

January 2020

The Effects Of Coordination Environment On The Spectroscopic And Electrochemical Properties Of Divalent Lanthanides

Tyler C. Jenks
Wayne State University

Follow this and additional works at: https://digitalcommons.wayne.edu/oa_dissertations

 Part of the [Chemistry Commons](#)

Recommended Citation

Jenks, Tyler C., "The Effects Of Coordination Environment On The Spectroscopic And Electrochemical Properties Of Divalent Lanthanides" (2020). *Wayne State University Dissertations*. 2451.
https://digitalcommons.wayne.edu/oa_dissertations/2451

This Open Access Dissertation is brought to you for free and open access by DigitalCommons@WayneState. It has been accepted for inclusion in Wayne State University Dissertations by an authorized administrator of DigitalCommons@WayneState.

**THE EFFECTS OF COORDINATION ENVIRONMENT ON THE SPECTROSCOPIC
AND ELECTROCHEMICAL PROPERTIES OF DIVALENT LANTHANIDES**

by

TYLER CHRISTIAN JENKS

DISSERTATION

Submitted to the Graduate School

of Wayne State University,

Detroit, Michigan

in partial fulfillment of the requirements

for the degree of

DOCTOR OF PHILOSOPHY

2020

MAJOR: CHEMISTRY (Inorganic)

Approved by:

Advisor Date

ACKNOWLEDGEMENTS

Earning my PhD has been one of the greatest challenges and utmost honors in my life, and I am grateful to everyone who helped me along my journey. Above all, I want to thank my family for their ongoing and unwavering support throughout my life. Everything I have and will accomplish is a direct reflection of my aspirations to realize the potential that you see in me. My parents, Todd and Elsa, always drove me to be my best at everything I did. They constantly encouraged me to try new things and never let me give up on anything. To my mom; you were always my number one fan, my loudest supporter, and I can still hear you screaming from the sidelines. To my dad; you were always there to practice with me no matter what sport, subject, or age, and there is absolutely no doubt in my mind that my success is as much yours as it is mine. And finally, to my baby sister Morgan; I can't imagine growing up without you and you will always be my closest friend.

Football, and sports in general, played a large part in my development and my opportunities; and, accordingly, my coaches throughout my youth played a pivotal role in my development as a person. Dan Waterman may not have been my dad, but he was nothing less than a third parent to me. He was the first one to get me into the weight room and inspired a lifelong passion that I am grateful for. Jim Olson gave me my first (and still favorite) job and kicked my ass on the wrestling mat well into his fifties. If anyone can teach grit, it's him, and I am a better man for having spent a decade in his presence. This list wouldn't be complete without Darren Geraghty, Tom McCutcheon, and Aaron Shreffler. Thank you all for teaching me about hard work and true commitment.

I would not have made it to graduate school without the influences of several key chemistry educators in my life. In high school, Jon Wier inspired my interest in chemistry and

helped me focus my academic interests. At Hillsdale College, I had many excellent chemistry professors, but the most profound influence was from my advisor Chris VanOrman. I was not confident enough in myself to consider graduate school to be a valid option, but, with Dr. V's encouragement, I made one of the best decisions of my life and pursued a graduate degree in chemistry.

What first attracted me to Wayne State was my initial interview with Matt Allen and the research being conducted in his group. When it came down to choosing research groups in my first year, I almost went another direction, but I can say with the utmost certainty that I made the correct choice by joining the Allen Lab. Dr. Allen has been a fantastic motivator and mentor, getting me through the rough patches that undoubtedly come with graduate school, and helping to develop the critical thinking necessary to be an effective scientist. My time under his mentorship has made me step outside my comfort zone and expand my skill set and knowledge base to make me a more well-rounded researcher. Along with Dr. Allen, I would like to thank Federico Rabuffetti, Jenn Stockdill, and Corey Stephenson for serving on my committee.

My five-year bid in grad school would also not have been possible without the support of my research group. The dynamic in the 230 Crew was incredible and we truly had something that no other group in our department did. The friends I made at Wayne State also played a huge role in maintaining my physical and emotional health throughout grad school. Matt Bailey really took me under his wing and coached me through the seemingly endless stream of techniques that I was not familiar with. Pulling all-nighters for three months straight to finish that first photoredox paper sparked our friendship, and, at times, having a desk next to his was the only thing keeping me motivated to come to work every day. My friendships with Adam Boyden and Gabe Stewart both began as lifting buddies, but both have extended well beyond the confines of

the Mort Harris Recreation and Fitness Center. These friendships were the subplots that got me through the arc of grad school, and I have no doubt that they will last forever.

Finally, I want to thank my wonderful girlfriend Andrea and our wonder-dog Freya. Our pack has been the glue that has held me together for the last four years and I cannot express what you mean to me. After all this time together, I still get excited every time I come home to you. Finding you was the single best outcome of my time in grad school, and I hope to one day ease your suspicions that I am a serial killer.

TABLE OF CONTENTS

Acknowledgements	ii
List of Tables	viii
List of Figures.....	ix
List of Symbols and Abbreviations	xiii
Chapter 1: Divalent Lanthanide Luminescence in Solution	1
1.1 Introduction.....	1
1.1.1 4f–5d Transitions	1
1.1.2 Nonradiative Deactivation	4
1.1.3 Solid-State Doping	5
1.2 Complexes of Divalent Europium.....	7
1.2.1 Divalent Europium Salts	7
1.2.2 Macrocyclic Complexes of Divalent Europium	8
1.2.3 Sandwich Complexes of Divalent Europium	18
1.2.4 Other Complexes of Divalent Europium	21
1.3 Complexes of Divalent Ytterbium	24
1.4 Complexes of Divalent Samarium and Other Divalent Lanthanides	27
1.5 Summary.....	29
1.6 Thesis Overview	30

Chapter 2: First Use of a Divalent Lanthanide in Visible-Light-Promoted Photoredox Catalysis	32
2.1 Introduction.....	32
2.2 Results and Discussion.....	33
2.3 Summary.....	43
2.4 Materials and Methods.....	44
2.4.1 Experimental Procedures.....	44
2.4.2 Gas Chromatography–Mass Spectrometry.....	48
2.4.3 Cyclic Voltammetry	50
Chapter 3: Photophysical Characterization of a Highly Luminescent Divalent-Europium-Containing Azacryptate.....	52
3.1 Introduction.....	52
3.2 Results and Discussion.....	53
3.3 Summary.....	60
3.4 Materials and Methods.....	61
3.4.1 Experimental Procedures.....	61
3.4.2 Synthesis of Eu25I₂.....	61

Chapter 4: Spectroscopic and Electrochemical Trends in Divalent Lanthanides Through the Modulation of Coordination Environment	63
4.1 Introduction.....	63
4.2 Results and Discussion.....	65
<i>4.2.1 Solid-State Characterization</i>	<i>65</i>
<i>4.2.2 Photophysical Characterization.....</i>	<i>67</i>
<i>4.2.3 Electrochemical Characterization</i>	<i>72</i>
4.3 Summary.....	76
4.4 Materials and Methods.....	77
<i>4.4.1 Experimental Procedures.....</i>	<i>77</i>
<i>4.4.2 Synthesis of Yb^{II}-Containing Complexes</i>	<i>78</i>
Chapter 5: Summary and Future Directions	80
5.1 Summary.....	80
5.2 Future Directions	81
Appendix A: Supplementary Figures	84
Appendix B: Permissions	113
References	116
Abstract.....	142
Autobiographical Statement	144

LIST OF TABLES

Table 1.1 Luminescence properties measured in methanol at a europium concentration of 4 mM. ⁹	11
Table 1.2 Luminescence properties of the Eu ^{II} -containing sandwich complexes.....	19
Table 2.1 Stoichiometric control reactions.	37
Table 2.2 Stern–Volmer data.	38
Table 4.1 Lowest-energy absorbance maxima and corresponding extinction coefficients of Yb ^{II} -containing cryptates.	68
Table 4.2 Excitation and emission wavelengths of YbI ₂ and Yb ^{II} -containing complexes.....	72
Table 4.3 $E_{1/2}$ potentials of YbI ₂ and Yb ^{II} -containing complexes vs Fc/Fc ⁺	73

LIST OF FIGURES

- Figure 1.1** Part of the emission spectrum of a solid sample of the SmI₂ complex of 18-crown-6 recorded at 77 K. The 4f–4f emissions—⁵D₁→⁷F₃, ⁵D₀→⁷F₁, and ⁵D₀→⁷F₃—overlap the broader 5d–4f emission (4f⁵5d¹→4f⁶) (adapted from reference 6). 2
- Figure 1.2** Schematic configurational-coordinate diagram for (a) 4fⁿ–4fⁿ and (b) 4fⁿ–4fⁿ⁻¹5d¹ transitions for a lanthanide ion. The lengths of the excitation and emission arrows represent the magnitude of energy associated with that transition and the difference in energy between them is the Stokes shift. 3
- Figure 1.3** Energies of 4f–5d transitions for divalent lanthanides in CaF₂ plotted versus the number of 4f electrons of the Ln^{II} ion. Circles represent empirical data on spin-allowed transitions and triangles represent empirical data on spin-forbidden transitions. The dashed curve represents the calculated values for the lanthanides (adapted from reference 17). 6
- Figure 1.4** (a, black) Chemiluminescence and (b, dark blue) photoluminescence spectra of the reaction solution containing Eu(NO₃)₃·6H₂O and *i*-Bu₂AlH in tetrahydrofuran. Photoluminescence spectra of (c, red) crystalline and (d, blue) solid Eu(NO₃)₃·6H₂O (adapted from reference 20). 8
- Figure 1.5** Macrocyclic ligands studied by Adachi and co-workers.^{21,26–31} 10
- Figure 1.6** Schematic representation of the 3:1 coordination of crown ether **2** to Eu^{II} 12
- Figure 1.7** Molecular structures of the divalent europium complexes with cryptands **16** (left) and **17** (right).^{32,33} Thermal ellipsoids are drawn at 50% probability. H atoms and non-coordinated solvent molecules and counteranions are omitted for clarity. Grey = carbon; red = oxygen; blue = nitrogen; seagreen = europium; and green = chloride. 15
- Figure 1.8** (Top) Nitrogenous cryptands used in the luminescence studies of divalent europium and (bottom) molecular structure of corresponding Eu^{II}-containing cryptates.^{35,36} Thermal ellipsoids are drawn at 50% probability. H atoms and non-coordinated solvent molecules and counteranions are omitted for clarity. Grey = carbon; blue = nitrogen; seagreen = europium; purple = iodide; and green = chloride. 17
- Figure 1.9** Eu^{II}-containing sandwich complexes. 18

- Figure 1.10** (a) hexafluoroisopropoxide ligand and molecular structures of (b) **34** and (c) **35**.^{43,44} Thermal ellipsoids are drawn at 50% probability. H atoms and non-coordinated F atoms are omitted for clarity. Grey = carbon; seagreen = europium; red = oxygen; green = fluorine; and blue = yttrium. 21
- Figure 1.11** (Left) Structure of ligand **36** and (right) the molecular structure of the corresponding Eu^{II}-containing complex from a crystal.⁴⁵ Thermal ellipsoids are drawn at 50% probability. H atoms and non-coordinated counteranions and solvent molecules are omitted for clarity. Grey = carbon; seagreen = europium; orange = silicon; and blue = nitrogen. 23
- Figure 1.12** Ligands **37–40** used in chemiluminescence studies of divalent europium.⁵ 23
- Figure 1.13** (a) Structure of cryptand **41**; (b) molecular structure of Yb^{II}**25**; and (c) luminescence spectra of YbI₂ (black), Yb^{II}**17** (yellow), Yb^{II}**23** (blue), Yb^{II}**25** (red), and Yb^{II}**41** (green).⁴⁷ Thermal ellipsoids are drawn at 50% probability. H atoms and non-coordinated iodides are omitted for clarity. Grey = carbon; seagreen = europium; and blue = nitrogen. Emission spectra of YbI₂, Yb^{II}**17**, Yb^{II}**23**, and Yb^{II}**41** are plotted against the left y-axis, and the emission spectrum of Yb^{II}**25** is plotted against the right y-axis. 25
- Figure 1.14** Maximum emission wavelengths of Yb^{II}-containing complexes classified by donor type.^{45–49} 26
- Figure 1.15** Excitation (dashed line) and emission (solid line) spectra of the complexes of (a) Eu^{II}, (b) Yb^{II}, (c) Sm^{II}, and (d) Tm^{II} with **36** in tetrahydrofuran (adapted from reference 45). 29
- Figure 2.1** Structures of ligand **23** (left) and Eu^{II}**23** (right). 34
- Figure 2.2** UV–visible absorption spectrum of Eu^{II}**23**Cl₂ (—, left y-axis) and emission spectrum ($\lambda_{\text{ex}} = 460 \text{ nm}$, $\epsilon: 1044 \text{ M}^{-1} \text{ cm}^{-1}$) of Eu^{II}**23**Cl₂ (••, right y-axis). Spectra were acquired in methanol. Data collected by Matthew D. Bailey. 35
- Figure 2.3** Formation of products and disappearance of starting material as a function of time for (A) stoichiometric and (B) catalytic (10 mol%) benzyl chloride coupling reactions (squares = 1,2-diphenylethane, diamonds = benzyl chloride, and circles = toluene). Each point is the mean of three independently prepared reactions, and the error bars represent the standard error of the means. 36

Figure 2.4 Crystal structure of $[\text{Eu}^{\text{II}}\mathbf{17}][\text{ZnCl}_4]$ generated from a mixture of EuCl_3 , Zn^0 , and $\mathbf{17}$ in methanol. Thermal ellipsoids are drawn at 50% probability. Crystallographic data for this structure has been deposited at the Cambridge Crystallographic Data Centre under deposition number CCDC 1539923. H atoms and an outer-sphere molecule of methanol have been omitted for clarity. Grey = C; blue = N; seagreen = Eu; green = Cl; and brown = Zn. Data collected by Matthew D. Bailey.	40
Figure 2.5 Proposed catalytic cycle.	43
Figure 3.1 Structures of (left) $\text{Eu}\mathbf{23}\text{Cl}_2$ and (right) $\text{Eu}\mathbf{25}\text{I}_2$	53
Figure 3.2 Crystal structure of $\text{Eu}\mathbf{25}\text{I}_2$ oriented (left) perpendicular to and (right) along the C_3 axis. Hydrogen atoms, two outer-sphere iodide ions, and one molecule of methanol are omitted for clarity. Thermal ellipsoids are drawn at 50% probability. Crystallographic data for this structure are available at the Cambridge Crystallographic Data Centre under deposition number CCDC 1826978. Blue = nitrogen; grey = carbon; and seagreen = europium. Data collected by Matthew D. Bailey.	54
Figure 3.3 Crystal structure of $\text{Eu}\mathbf{23}\text{I}_2$. Hydrogen atoms and an outer-sphere iodide ion have been omitted for clarity. Thermal ellipsoids are drawn at 50% probability. Crystallographic data for this structure are available at the Cambridge Crystallographic Data Centre under deposition number CCDC 1826977. Blue = nitrogen; grey = carbon; seagreen = europium; and pink = iodine. Data collected by Philip D. Martin.	55
Figure 3.4 Absorption (—, left y-axis), excitation (\cdots , right y-axis), and emission (---, right y-axis) spectra of $\text{Eu}\mathbf{25}\text{I}_2$ (1.8 mM) in methanol.	56
Figure 3.5 Orbital-energy diagram for the $5d_{z^2}$, $5d_{xy}$, and $4f_{z^3}$ orbitals for (left) $[\text{Eu}\mathbf{23}\text{Cl}]^+$, ⁷ (middle) $[\text{Eu}\mathbf{25}]^{2+}$, and (right) $[\text{Eu}\mathbf{23}']^{2+}$ (where $[\text{Eu}\mathbf{23}']^{2+}$ is $[\text{Eu}\mathbf{23}\text{Cl}]^+$ forced into an eight-coordinate distorted bicapped antiprism, like $[\text{Eu}\mathbf{25}]^{2+}$). Dashed lines are visual guides. Computations performed by Brooke A. Corbin.	58
Figure 3.6 Quartz cuvette (1 cm path length) containing a solution of $\text{Eu}\mathbf{25}\text{I}_2$ (1.5 mM) in methanol with (a) white and (b) black backgrounds. (c) The same cuvette under irradiation from a long-wave UV handheld lamp.	60
Figure 4.1 Series of cryptands, $\mathbf{17}$, $\mathbf{41}$, $\mathbf{23}$, and $\mathbf{25}$, displaying variations in donor atom identity, electronic character, and steric bulk.	64

- Figure 4.2** Molecular structures in crystals of (a) Yb^{II}**17** and (b) Yb^{II}**41**; (c) schematic representation of the eclipsed hula-hoop geometry of Yb^{II}**17** and Yb^{II}**41**; molecular structures in crystals of (d) Yb^{II}**23** and (e) Yb^{II}**25**; and (f) schematic representation of the bicapped trigonal antiprism geometry of Yb^{II}**23** and Yb^{II}**25**. Thermal ellipsoids are drawn at 50% probability. Hydrogen atoms, non-coordinated iodide ions, and non-coordinated solvent molecules are omitted for clarity. Blue, nitrogen; gray, carbon; red, oxygen; green, ytterbium; and purple, iodine. Crystallographic data for these structures have been deposited at the Cambridge Crystallographic Data Centre under deposition numbers CCDC 1977697–1977700. Data collected by Cassandra L. Ward and Matthew D. Bailey. 66
- Figure 4.3** UV–visible absorption spectra of YbI₂ and Yb^{II}-containing cryptates (1 mM) in methanol: YbI₂ (–), Yb^{II}**17** (···), Yb^{II}**41** (---), Yb^{II}**23** (----), and Yb^{II}**25** (---). 68
- Figure 4.4** Absorption maxima of Yb^{II}-containing cryptates, Eu^{II}-containing cryptates,^{7,13,36} YbI₂, and EuI₂. 69
- Figure 4.5** Excitation (···) and emission (—) spectra of YbI₂ and Yb^{II}-containing complexes (3 mM) in methanol: (a) YbI₂, (b) Yb^{II}**17**, (c) Yb^{II}**41**, (d) Yb^{II}**23**, and (e) Yb^{II}**25**. 71
- Figure 4.6** Emission maxima of Yb^{II}-containing cryptates, Eu^{II}-containing cryptates,^{7,13,36} YbI₂, and EuI₂. 71
- Figure 4.7** Cyclic voltammograms of (A) YbI₂, (B) Yb^{II}**17**, (C) Yb^{II}**41**, (D) Yb^{II}**23**, and (E) Yb^{II}**25** in *N,N*-dimethylformamide. 74
- Figure 4.8** $E_{1/2}$ potentials of Yb^{II}-containing cryptates, Eu^{II}-containing cryptates,¹⁷⁹ YbI₂, and EuI₂. Values for Eu^{II}**17** and Eu^{II}**41** are for anodic peak potentials. 75

LIST OF SYMBOLS AND ABBREVIATIONS

Symbol/Abbreviation	Term
Ln	lanthanide
M–L	metal–ligand
UV	ultraviolet
IR	infrared
NMR	nuclear magnetic resonance
GC	gas chromatography
MS	mass spectrometry
CV	cyclic voltammetry
EDXF	energy-dispersive X-ray fluorescence
EDX	energy-dispersive X-ray spectroscopy
ICP	inductively coupled plasma
TD-DFT	time-dependent density functional theory
SMD	solvation model based on density
h	hours
min	minutes
s	seconds
μs	microseconds
ns	nanoseconds
MHz	megahertz
cm	centimeters
nm	nanometers
mL	milliliters
mg	milligrams
amu	atomic mass units
ppm	parts per million

wt %	weight percent
mol	moles
mmol	millimoles
mol%	mole percent
M	molar
mM	millimolar
ϵ	molar absorptivity
h	Planck's constant
c	speed of light
λ	wavelength
λ_{exc}	excitation wavelength
λ_{em}	emission wavelength
λ_{abs}	absorption wavelength
λ_{max}	maximum wavelength
eV	electron volts
keV	kilo electron volts
W	watts
A	amperes
μA	microamperes
V	volts
mV	millivolts
$E_{1/2}$	electrochemical potential
$E_{1/2}^*$	excited-state electrochemical potential
E_{ox}	oxidation potential
E_{red}	reduction potential
E_{pc}	peak cathodic potential
$E_{0,0}$	energy of emission band

K	Kelvin
°C	degrees Celsius
E	energy
<i>I</i>	intensity
<i>I</i> ₀	initial intensity
<i>k</i> _q	rate of quenching
<i>i</i> -butyl, <i>i</i> -Bu	isobutyl
<i>n</i> -propanol	normal propanol
<i>n</i> -pentane	normal pentane
THF	tetrahydrofuran
X	anion
OTf, OTf ⁻	triflate
OAc	acetate
Fc/Fc ⁺	ferrocene/ferrocenium
Cp	cyclopentadienyl
Ph	phenyl
bpy	bipyridine
equiv	equivalents
Anal. Calcd	analysis calculated
NR	not reported
ACS	American Chemical Society
LED	light-emitting diode
CCDC	Cambridge Crystallographic Data Centre

CHAPTER 1: DIVALENT LANTHANIDE LUMINESCENCE IN SOLUTION

1.1 Introduction

The luminescence of divalent lanthanides has seen extensive use in phosphors and lighting, especially in the solid state, which will be discussed briefly in this chapter. The luminescence of molecular complexes of divalent lanthanides also has great utility in applications such as sensing and imaging, but far fewer research endeavors have been focused on these complexes, especially in solution. This limited amount of research stems from the propensity of the divalent states of lanthanides to oxidize to their trivalent counterparts. Until recently, it was thought that the only lanthanides that formed discrete, isolable molecular complexes in the divalent state were those with the most positive $\text{Ln}^{\text{III}}/\text{Ln}^{\text{II}}$ electrochemical couples. However, in 2013, isolation of a nearly complete series of divalent lanthanide complexes was reported (except for Pm^{II}).¹ Although solution-phase luminescence studies have not been performed on molecular complexes of most of the divalent lanthanides, isolation of the complexes is a promising start towards what are sure to be interesting and informative studies. This chapter describes the luminescence of divalent lanthanides with a predominant focus on molecular complexes of divalent lanthanides in solution.

1.1.1 4f–5d Transitions

The luminescence of divalent lanthanides is dominated by 4f–5d transitions, but 4f–4f transitions can also be observed with these ions (**Figure 1.1**).^{2–5} However, because 4f–4f transitions often occur simultaneously with 4f–5d transitions in divalent lanthanides, the 4f–4f transitions are usually obscured by the more intense parity-allowed 4f–5d transitions that occur in the same energy range. Divalent lanthanides exhibit 4f–5d transitions that are typically located in the UV to IR range of the electromagnetic spectrum. This range of energies, spanning the

visible region, makes the 4f–5d transitions of divalent lanthanides distinct from the same transitions of trivalent lanthanides that typically have 4f–5d transitions at energies associated with UV light. Unlike 4f electrons that are shielded from the surrounding environment by the full 5s and 5p orbitals, electrons in the 5d orbitals of lanthanides are influenced by ligand fields. Because of this vulnerability of 5d electrons, 4f–5d transitions display broad, intense peaks that are prone to vibronic coupling due to the spatially accessible 5d electron in the $4f^{n-1}5d^1$ excited state.

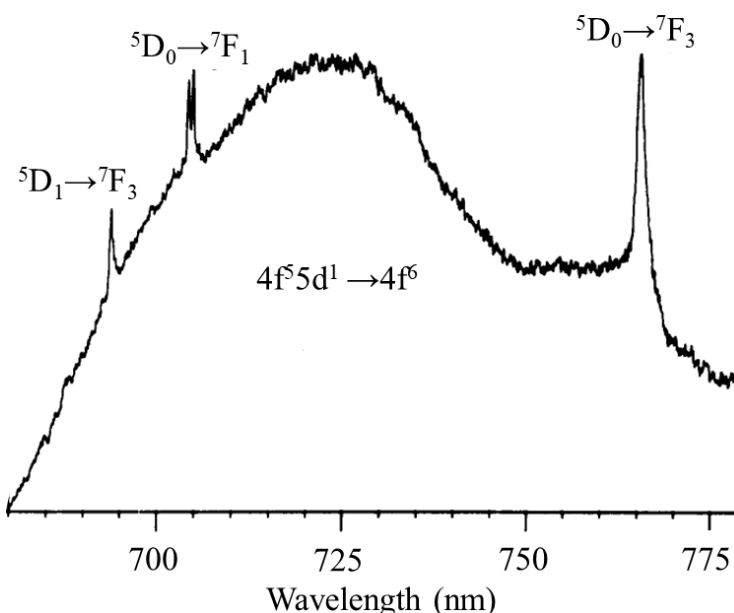


Figure 1.1 Part of the emission spectrum of a solid sample of the SmI_2 complex of 18-crown-6 recorded at 77 K. The 4f–4f emissions— $^5D_1 \rightarrow ^7F_3$, $^5D_0 \rightarrow ^7F_1$, and $^5D_0 \rightarrow ^7F_3$ —overlap the broader 5d–4f emission ($4f^5 5d^1 \rightarrow 4f^6$) (adapted from reference 6).

The configurational-coordinate diagrams of 4f–4f and 4f–5d transitions demonstrate the physical characteristics of the excited states that give rise to the peak widths and Stokes shifts associated with each type of transition (**Figure 1.2**). Bond lengths of the ground and excited states of 4f–4f transitions do not vary considerably.^{2–4} The similarity in bond lengths between ground and excited states is indicative of alignment of the ground- and excited-state energy wells

and consequent narrow line widths and small Stokes shifts. In contrast, $4f^{n-1}5d^1$ excited states move to shorter bond lengths than $4f^n$ ground states.^{2,7} This decrease in bond length is caused by an expansion of the electron charge distribution due to an electron being promoted from a 4f orbital to a 5d orbital, resulting in a slightly more positive effective nuclear charge for the lanthanide ion with respect to the ground state.² The change in charge distribution leads to the lanthanide ion interacting more strongly with coordinated atoms or ions, shortening bond lengths. As excited states relax to their lowest vibrational states, they move radially from the center of the ground-state potential energy wells, lowering emission energies with respect to excitation energies. Another feature of note in these diagrams is the wider parabola representing the $4f^{n-1}5d^1$ excited state with respect to the $4f^n$ ground and excited states. This widening is due to the interaction of the 5d orbitals with the surrounding ligand field and accounts for the broad peaks associated with 4f–5d transitions.

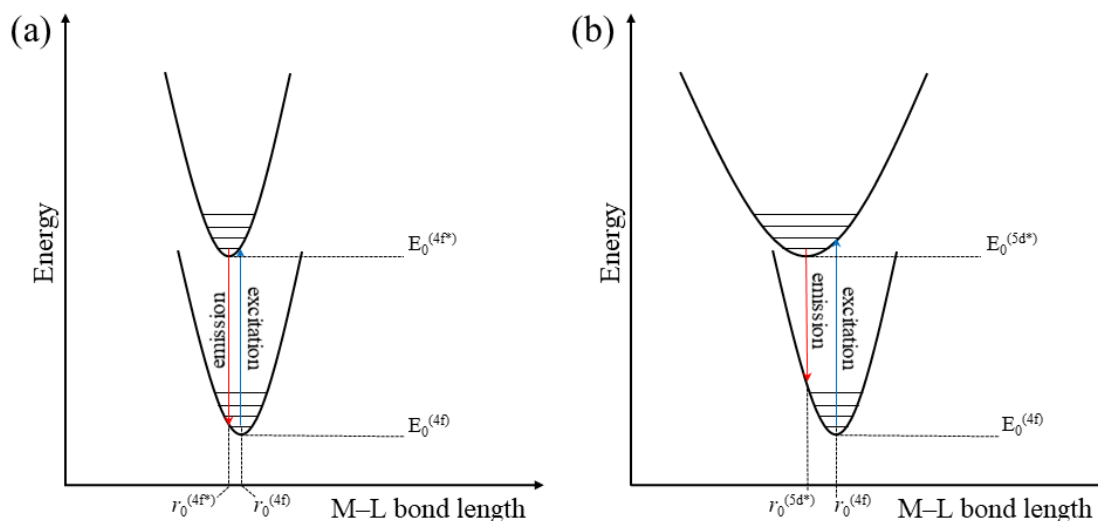


Figure 1.2 Schematic configurational-coordinate diagram for (a) $4f^n-4f^n$ and (b) $4f^n-4f^{n-1}5d^1$ transitions for a lanthanide ion. The lengths of the excitation and emission arrows represent the magnitude of energy associated with that transition and the difference in energy between them is the Stokes shift.

The increased intensity of 4f–5d transitions relative to 4f–4f transitions arises from 4f–5d transitions being parity allowed, giving the 4f–5d transition a higher probability of undergoing excitation and emission. Another feature of 4f–5d transitions is their broad peaks that arise from interaction of the 5d orbitals with ligand fields based not only on subtle geometric differences from vibronic coupling and solvation-layer structure but also coordinating atom identity in the case of labile solvents. The coordinating atoms of a complex also have an effect on the centroid shift of the 5d orbitals, which is the shift in 5d orbital energy with the respect to the 4f orbitals due to the nephelauxetic effect. The nephelauxetic effect induces centroid shifts of the 5d orbitals to lower energy with increasing covalency of metal–ligand bonds.^{2,8} Consequently, not only are 4f–5d transitions broad, but they also can be tuned throughout UV, visible, and IR energies. This tunability makes 5d–4f emissions of divalent lanthanides useful in luminescence applications.

1.1.2 Nonradiative Deactivation

As described in section 1.1.1, the 5d orbitals of lanthanide ions are more susceptible than the 4f orbitals to ligand environment. Although this susceptibility enables modulation of 4f–5d transition energies, it also leaves $4f^{n-1}5d^1$ excited states vulnerable to nonradiative decay via energy overlap with oscillators in the coordination sphere of the lanthanide ion. Similar to the luminescence quenching observed with some trivalent lanthanide ions, O–H and N–H oscillators can quench the 5d–4f luminescence of divalent lanthanides.⁹ Because of this quenching, it is generally desirable to avoid solvents containing these oscillators when performing spectroscopic measurements pertaining to luminescence intensity. Aside from nonradiative quenching from energy overlap with solvent oscillators, the photo-induced reaction between divalent europium and protic solvents has also been shown to nonradiatively generate trivalent europium and hydrogen gas.¹⁰ Similar electron transfers from excited Eu^{II} and Sm^{II} ions to organic substrates

have been shown to compete directly with radiative decay of the excited state of these divalent lanthanide ions.^{11–14} When coordinated to divalent lanthanides, ligands containing O–H and N–H oscillators have also been shown to nonradiatively extinguish the excited state of luminescent lanthanide ions.^{9,15} A common technique for avoiding nonradiative quenching of the excited states of divalent lanthanides is to coordinatively saturate the ions with ligands that do not contain quenching oscillators. This saturation also eliminates open coordination sites for solvent molecules containing O–H and N–H oscillators. Some of the most effective ligand scaffolds used for this purpose are multidentate macrocyclic ligands like crown ethers and cryptands.

Another phenomenon that can cause nonradiative decay of the excited state of lanthanide ions is thermal quenching.² At higher thermal energy levels, the potential wells of ground and excited states cross, introducing a direct, nonradiative path from the excited state to the ground state (**Figure 1.2**). Narrowing of the excited-state energy well in the configurational-coordinate diagram pushes the crossing of the ground- and excited-state parabolas to higher energies, resulting in higher temperatures for the onset of thermal quenching. Additionally, at higher temperatures, there is more available vibrational energy in solvent and ligand molecules; therefore, the quenching caused by O–H and N–H oscillators becomes a more prevalent issue. For these reasons, it is common for luminescence experiments to be performed below room temperature.

1.1.3 Solid-State Doping

The divalent oxidation state is more stable for lanthanides in the solid state, and all the divalent lanthanides (excluding Pm^{II}) have been observed as molecular complexes.¹ Most applications requiring the luminescence of divalent lanthanides, such as solid-state lighting and lasing materials, use the elements in the solid state. Because of the increased stability of divalent

lanthanides in the solid phase and the prevalence of materials applications, a great deal of foundational knowledge and most of the available research on divalent lanthanide luminescence has been accumulated in the solid state.

The electronic transition energies of hundreds of inorganic compounds of divalent lanthanides were compiled by Dorenbos.¹⁶ He determined that each host matrix invokes a characteristic red shift and Stokes shift compared to the free ion energy for each divalent lanthanide. Using this knowledge, he successfully created a model in which the lowest-energy 4f–5d transition of any divalent lanthanide can be predicted if the energy of another divalent lanthanide 4f–5d transition in the same host lattice is known. An example of the predictive power of the Dorenbos model is presented in **Figure 1.3** that demonstrates the good agreement between predicted and experimental values for divalent lanthanides in CaF₂.¹⁷ For thorough discussions of the luminescence of divalent lanthanides in the solid-state, readers are referred to several review articles.^{3,16–18} The remainder of this chapter is focused on the luminescence of discrete complexes in solution.

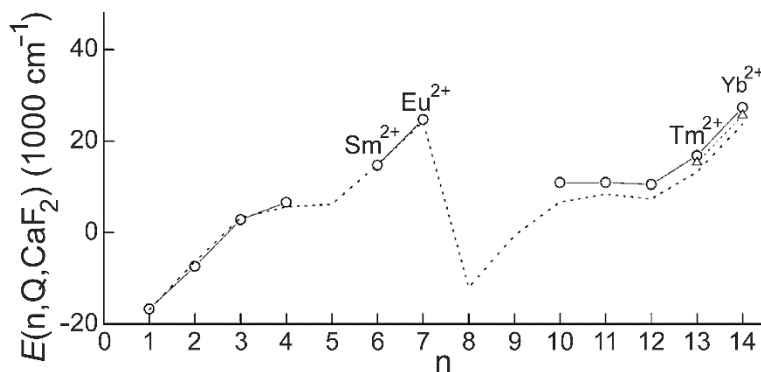


Figure 1.3 Energies of 4f–5d transitions for divalent lanthanides in CaF₂ plotted versus the number of 4f electrons of the Ln^{II} ion. Circles represent empirical data on spin-allowed transitions and triangles represent empirical data on spin-forbidden transitions. The dashed curve represents the calculated values for the lanthanides (adapted from reference 17).

1.2 Complexes of Divalent Europium

Europium, having the most positive $\text{Ln}^{\text{III}}/\text{Ln}^{\text{II}}$ electrochemical potential of the lanthanides, has been the most studied divalent lanthanide with respect to luminescence in solution. This section is divided into subsections describing different types of Eu^{II} -containing salts and coordination complexes including macrocyclic and sandwich complexes.

1.2.1 Divalent Europium Salts

In general, divalent europium salts are excited by UV irradiation and weakly emit blue light in solution. The intensity and wavelength of emission for Eu^{II} varies slightly as a function of solvent and counteranion.^{19–24} Promotion of Eu^{II} to the excited state through irradiation with light is the most common method of excitation, but chemiluminescence has also been reported.^{5,20,24,25} The system of $\text{EuX}_3 \cdot 6\text{H}_2\text{O}$ ($\text{X} = \text{Cl}$ or NO_3) in tetrahydrofuran (THF) with various alkylaluminum complexes has been shown to produce Eu^{II} luminescence through chemical excitation (**Figure 1.4**).^{20,25} The trivalent europium salt is reduced by the excess alkylaluminum complex, forming the divalent salt that can be roughly approximated as $\text{EuX}_2(\text{THF})_2 \cdot \text{R}_{3-x}\text{AlH}_x$ in solution where R is *i*-butyl, ethyl, or methyl. Unreacted alkylaluminum complex in solution reacts with residual molecular oxygen to form triplet-excited aldehyde that transfers energy to divalent europium to induce Eu^{II} luminescence. As a specific example, the chemiluminescence of $\text{EuX}_2(\text{THF})_2 \cdot i\text{-Bu}_2\text{AlH}$ display similar emission wavelengths for the chloride and nitrate salts (447 and 454 nm, respectively), but the chemiluminescence of the chloride-containing system is approximately six times more intense than the nitrate-containing system. It was hypothesized that the difference in emission intensity was due to a more efficient energy transfer between triplet excited isobutyric aldehyde and $\text{EuCl}_2(\text{THF})_2 \cdot i\text{-Bu}_2\text{AlH}$ relative to the nitrate salt.²⁰

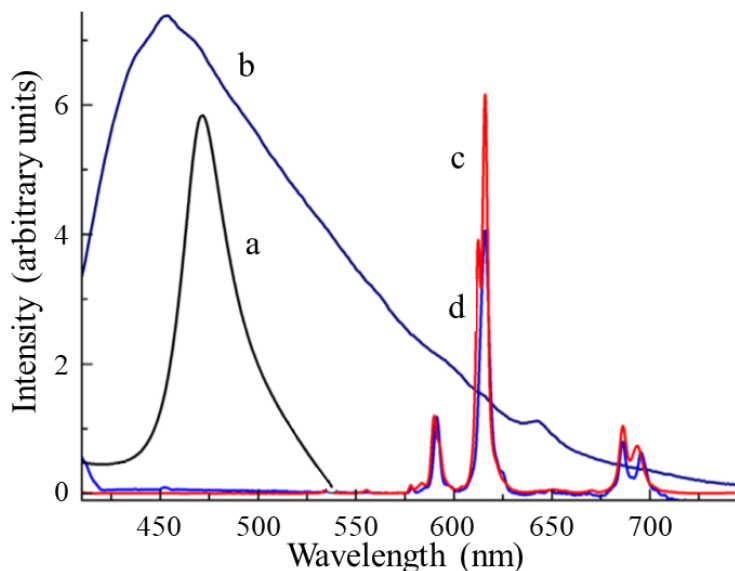


Figure 1.4 (a, black) Chemiluminescence and (b, dark blue) photoluminescence spectra of the reaction solution containing $\text{Eu}(\text{NO}_3)_3 \cdot 6\text{H}_2\text{O}$ and $i\text{-Bu}_2\text{AlH}$ in tetrahydrofuran. Photoluminescence spectra of (c, red) crystalline and (d, blue) solid $\text{Eu}(\text{NO}_3)_3 \cdot 6\text{H}_2\text{O}$ (adapted from reference 20).

Another chemiluminescent system involving divalent europium was reported with EuCl_3 in dimethylformamide.²⁴ In this system, dimethylformamide replaces one or two chlorides in the inner coordination sphere of solvated EuCl_3 . Under UV irradiation, dimethylformamide becomes excited, and electron density is directed from the oxygen atom of the excited dimethylformamide to Eu^{III} . With the donated electron density, Eu^{III} is reduced to an excited Eu^{II} ion that subsequently emits at 530 nm and transfers the electron back to dimethylformamide, reforming the ground-state complex of Eu^{III} .

1.2.2 Macrocyclic Complexes of Divalent Europium

Macrocyclic ligands, such as crown ethers and cryptands, are some of the most widely studied ligands for luminescence enhancement of divalent europium. One benefit of these ligands is that many of them have been shown to positively shift the electrochemical potential of the $\text{Ln}^{\text{III}}/\text{Ln}^{\text{II}}$ couple of europium in protic solvents, including water and methanol.⁹ This shifting

of electrochemical potential makes the Eu^{II} -containing complex less prone to reduction by solvent molecules, making the complexes easier to study in solution. Although the electrochemical shift is not positive enough to prevent oxidation of complexes in the presence of molecular oxygen, it provides a larger range of conditions in which the complexes can be studied. Also, macrocyclic ligands generally tend to increase the luminescence intensity of coordinated Eu^{II} ions with respect to the uncomplexed ion. This increase in luminescence intensity has been attributed to a shielding effect that macrocyclic ligands impart on coordinated ions.⁴ The shielding effect refers to the ability of a macrocyclic ligand to saturate the coordination sphere of a metal ion. By blocking sites at which the metal ion could interact with O–H and N–H oscillators from solvent molecules, the ligand effectively lowers the frequency of interactions that lead to nonradiative quenching of the excited state of Eu^{II} .

An early set of systematic investigations of the enhancement of the luminescence of Eu^{II} by macrocyclic ligands was conducted by Adachi and co-workers.^{9,21,26–31} They used several properties to compare the luminescence of Eu^{II} -containing complexes (**Figure 1.5** and **Table 1.1**). The main benchmark used for comparison was the relative luminescence intensity of each divalent europium complex with respect to an equimolar solution of EuCl_2 . After reporting a large (690×) enhancement of the luminescence intensity of Eu^{II} through complexation with a series of macrocyclic ligands, Adachi and co-workers explored the effects of other crown ether derivatives on the luminescence of divalent europium (**Figure 1.5**).^{9,21} The selection of macrocyclic ligands in this study consisted of crown ethers and cryptands with various cavity sizes, denticities, coordinating atom identities, and functionalities.

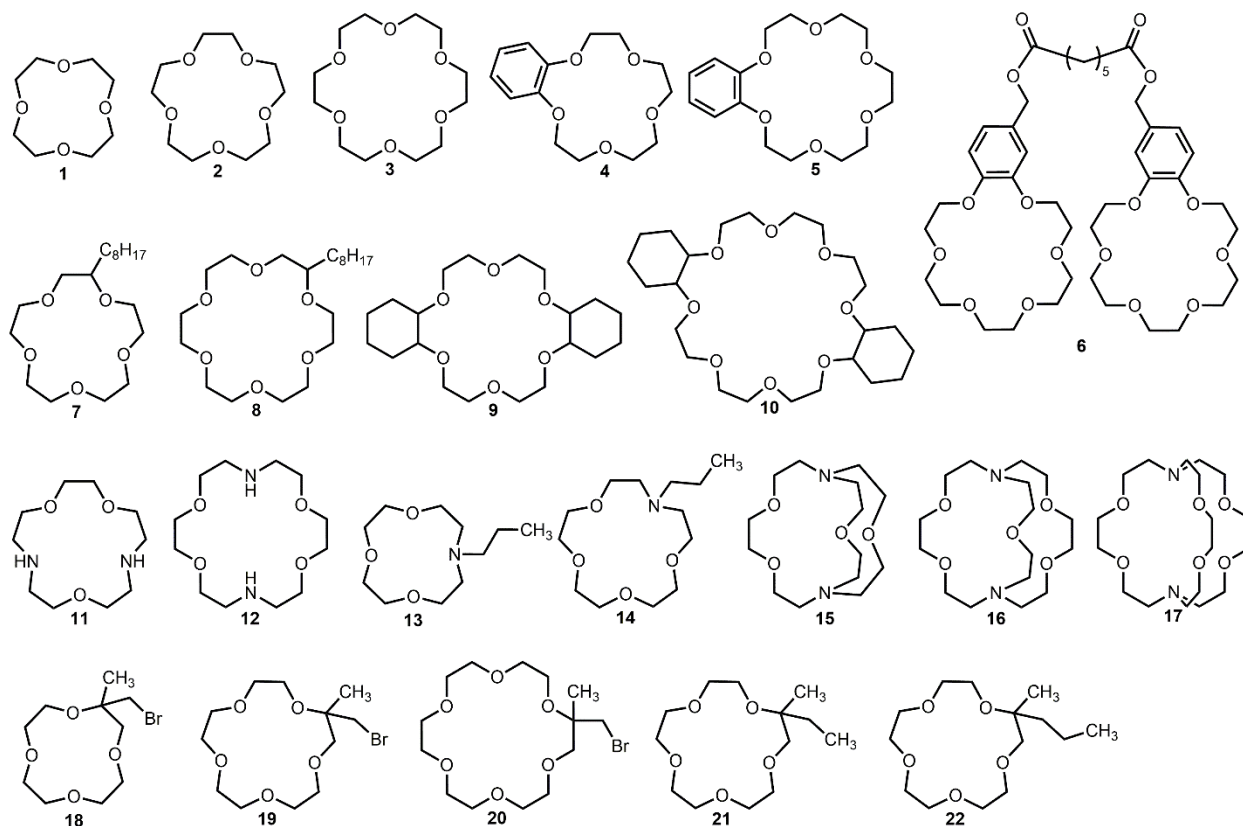


Figure 1.5 Macrocyclic ligands studied by Adachi and co-workers.^{21,26-31}

To explain the differences in relative emission intensities among Eu^{II}-containing complexes, other luminescence properties of these complexes were compared with an emphasis on radiative and nonradiative rate constants.⁹ In general, Eu^{II}-containing complexes in the series studied by Adachi and co-workers displayed radiative rate constants within an order of magnitude of EuCl₂. The nonradiative rate constants, however, varied significantly with the lowest values belonging to ligands with the highest luminescence enhancement. This correlation between nonradiative rate constant and luminescence enhancement suggests that the most important factor in luminescence efficiency is the ability of a ligand to adequately encapsulate the Eu^{II} ion to protect it from interactions with O–H and N–H oscillators.⁹

Table 1.1 Luminescence properties measured in methanol at a europium concentration of 4 mM.⁹

Complex	Maximum emission wavelength (nm)	Relative emission intensity	Luminescence quantum yield (%)	Luminescence lifetime (ns)	Radiative rate constant ($\times 10^{-5}$ s)	Nonradiative rate constant ($\times 10^{-5}$ s)
EuCl ₂	489	1.0	0.036	2.1	2.1	5900
Eu ^{II} 1	428	93	3.6	300	1.2	32
Eu ^{II} 2	432	690	28	800	3.5	9.0
Eu ^{II} 3	446	160	9.4	142	6.6	64
Eu ^{II} 4	417	95	1.5	143	1.2	69
Eu ^{II} 5	447	9.2	0.2	28	0.72	360
Eu ^{II} 6	448	2.2	0.05	NR	NR	NR
Eu ^{II} 7	423	690	2.1	761	2.8	12
Eu ^{II} 8	445	120	6.7	143	4.7	66
Eu ^{II} 9	440	87	3.8	89	4.3	110
Eu ^{II} 10	443	180	2.9	290	0.099	3.4
Eu ^{II} 11	460	130	7.1	42	1.7	21
Eu ^{II} 12	469	6.8	4.6	16	0.29	62
Eu ^{II} 13	488	410	14	810	1.7	11
Eu ^{II} 14	472	13	0.31	16	1.9	620
Eu ^{II} 15	445	1.0	0.05	NR	NR	NR
Eu ^{II} 16	445	29	1.4	24	0.58	41
Eu ^{II} 17	468	270	9.3	200	0.47	4.5

NR = not reported

Of all the ligands in Adachi's studies, 15-crown-5 (**2**) induced the largest enhancement of luminescence intensity of Eu^{II} relative to EuCl₂.⁹ Two other sizes of crown ethers were included in Adachi's studies, 12-crown-4 (**1**) and 18-crown-6 (**3**), but they did not induce as large of a luminescence enhancement as **2**. The success of **2** in terms of luminescence enhancement was ascribed to two factors: cavity size of the ligand and ligand-to-metal ratio of the resulting Eu^{II}

complex. Crown ether **2** has the cavity size (0.9–1.1 Å) closest to the ionic radius of Eu^{II} (1.09 Å), and the europium ion sits just above the plane of the crown ether.^{9,26,27} Two more equivalents of **2** sit above the exposed side of the Eu^{II} ion (**Figure 1.6**), making the ligand-to-metal ratio 3:1 (based on Job plot and $^1\text{H-NMR}$ studies of the Sr^{II} -containing analogue), effectively blocking O–H oscillators of methanol from interacting with the inner sphere of the excited Eu^{II} ion. The smaller size of **1** forces the Eu^{II} ion to sit farther above the equatorial plane of the crown relative to **2**, but a binding ratio for this complex was not reported. Although the larger cavity size of **3** enables the Eu^{II} ion to sit in the equatorial plane of the crown ether, this ligand forms a 1:1 complex with Eu^{II} based on $^1\text{H-NMR}$ studies of the Sr^{II} -containing analogue and, therefore, leaves open inner-sphere coordination sites above and below the plane of the crown for interactions with methanol.²⁶

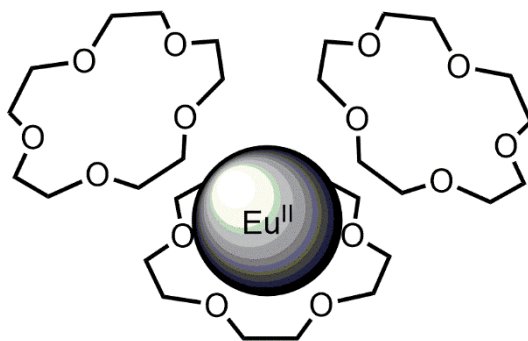


Figure 1.6 Schematic representation of the 3:1 coordination of crown ether **2** to Eu^{II} .

Despite the smaller cavity size of **2** with respect to **3**, the greater luminescence enhancement of Eu^{II} by coordination to **2** was ascribed to its superior ability to block interactions between solvent molecules and the coordinated Eu^{II} ion. To investigate the ability of **2** and **3** to block interactions between coordinated Eu^{II} ions and solvent further, the luminescence of the complexes was compared in four protic solvents: water, methanol, ethanol, and *n*-propanol.²⁸ The maximum wavelength of the emission band of the Eu^{II} complex with **3** shifted to higher

energy with increasing molecular weight of solvent, whereas the emission wavelength was unaffected with **2**. A decrease in the luminescence lifetime and quantum yield with increasing solvent molecular weight was also observed with **3**, while the quantum yield observed with **2** was hindered only by water and remained unaffected by the alcohols. Lastly, the quantum yield and luminescence lifetime for both complexes were compared in methanol and deuterated methanol. The values for **2** were unchanged while the quantum yield and lifetime both increased for **3** in the deuterated solvent. The diminished influence of solvent effects on the luminescence of $\text{Eu}^{\text{II}}\mathbf{2}$ relative to $\text{Eu}^{\text{II}}\mathbf{3}$ is evidence that **2** is more capable of minimizing interactions between coordinated Eu^{II} ions and solvent molecules.

Adachi and co-workers also studied derivatives of crown ethers containing benzo (**4–6**) and alkyl groups (**7–10**).^{21,26,27,29} The benzo-containing crown ethers **4–6** resulted in less luminescence enhancement relative to nonfunctionalized crowns **2** and **3**. This decrease in enhancement for **4–6** was attributed to the decreased flexibility of the crown ether with the addition of a benzo group. With lower flexibility, the ligand cannot as effectively encapsulate Eu^{II} and provide protection from solvent-based oscillators. Although electronic effects from the benzo group might be expected, the researchers claim that no intramolecular sensitization was observed.^{26,29} Crown ethers **7** and **8** adorned with octyl moieties displayed luminescence enhancement similar to their nonfunctionalized analogues, indicating that the alkyl chains have little effect on the efficiency of these ligands to exclude the coordination of solvent molecules to Eu^{II} . Along the same vein, crowns **9** and **10** bearing cyclohexyl groups displayed more luminescence enhancement than the benzo-containing crown ethers. Although crowns **5** and **9** have different numbers of functionalities, comparison of these two ligands suggests that non-

aromatic moieties impart less rigidity on the ligand and therefore better encapsulation of the Eu^{II} ion.

To investigate the effects of nitrogenous donor atoms relative to ethereal donors in a comparably sized cavity, ligands **11–14** were complexed with Eu^{II} for comparison to the Eu^{II}-containing complexes of ligands **1–3**.^{26,30} In general, the ligands containing coordinating nitrogen atoms induced less luminescence enhancement of Eu^{II}. Only ligand **13** outperformed its ethereal counterpart, **1**, in terms of luminescence enhancement, which was found to be a result of its 2:1 ligand/metal ratio that enabled greater insulation of the Eu^{II} ion from methanol. The lower luminescence enhancement imparted on Eu^{II} by **11** and **12** was attributed to the coupling of the N–H oscillators from the secondary amines on the ligands to the excited state of Eu^{II}. These nitrogen-containing crown ethers also induced broader emission bands and red shifts in emission wavelengths for Eu^{II} with respect to **1–3**. Because nitrogen is a stronger donor than oxygen, a greater splitting of the d orbitals leads to a greater curve of the 4fⁿ⁻¹5d¹ excited state in the configurational-coordinate diagram. The greater d-orbital splitting increases the width of the 5d–4f emission band and moves the transition to slightly lower energies.

Three cryptands were also investigated by Adachi and co-workers including [2.1.1] (**15**), [2.2.1] (**16**), and [2.2.2] (**17**).²⁶ Cryptands **16** and **17** form complexes with EuCl₂ (**Figure 1.7**),^{32,33} but **15** was too small to encapsulate the Eu^{II} ion adequately and provided no luminescence enhancement with respect to EuCl₂.²⁶ Although **16** has the cavity size closest to the ionic radius of Eu^{II}, it did not provide the highest luminescence enhancement, indicating that cavity size compatibility is not the only determining factor for luminescence enhancement. Cryptand **17** has a slightly larger cavity and one more coordinating atom than **16**, enabling **17** to occupy more coordination sites where solvent molecules might nonradiatively interact with the

excited state. These factors result in **17** inducing the greatest luminescence enhancement of Eu^{II} among the three cryptands studied by Adachi and co-workers.

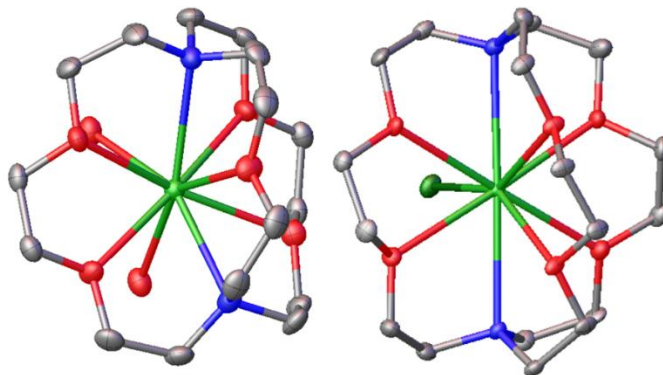


Figure 1.7 Molecular structures of the divalent europium complexes with cryptands **16** (left) and **17** (right).^{32,33} Thermal ellipsoids are drawn at 50% probability. H atoms and non-coordinated solvent molecules and counteranions are omitted for clarity. Grey = carbon; red = oxygen; blue = nitrogen; seagreen = europium; and green = chloride.

A separate study was conducted to determine the effects of added anions on the luminescence of divalent europium complexes of **3** and **17**.³⁴ Solutions of $\text{Eu}^{\text{II}}\mathbf{3}$ and $\text{Eu}^{\text{II}}\mathbf{17}$ were prepared through the reduction of $\text{Eu}(\text{OTf})_3$ by zinc metal in methanol in the presence of either **3** or **17** and five equivalents of the respective anion to be studied (Cl^- , Br^- , I^- , NO_3^- , SCN^- , OAc^- , or none). For both complexes, no change in the emission wavelength was observed, but a decrease in the Eu^{II} luminescence intensity was observed with the addition of NO_3^- , SCN^- , and OAc^- . No explanation of these results was given, but because there was no change in the emission wavelength, there was likely no change in the geometry of the complex between the anions. The differences in luminescence intensities could be related to the presence of intramolecular vibrations in the NO_3^- , SCN^- , and OAc^- anions, which could potentially overlap with the energy of the Eu^{II} excited state leading to nonradiative decay.

An interesting observation regarding emission intensity and wavelength was made with the Eu^{II} -containing complexes of ligands **18–22**.³¹ Crown ethers **18–20** contain bromoalkyl

groups, whereas **19** and **20** contain nonhalogenated alkyl chains. Over extended periods of irradiation, the emission intensities of the bromo-containing complexes increased, while the nonhalogenated complexes did not. A shift in emission to shorter wavelengths was also observed for the bromo-containing complexes but not for the nonhalogenated complexes. It was hypothesized that the cause of the shift in wavelength and increase in intensity of emission resulted from chelation by the alkyl chain through coordination of the terminal bromide. Chelation would change the donor from solvent to alkylbromide, thus reducing nonradiative quenching from coordinated solvent molecules.

In addition to the studies of Adachi and co-workers, the luminescence of several other cryptates of divalent europium have been reported.^{15,35,36} A common method for the modulation of Eu^{II} luminescence with respect to Eu^{II}**17** is the substitution of ethereal donors with softer nitrogenous donors (**Figure 1.8**).^{15,35,36} The Eu^{II} complex with **23** in basic water (pH 12) was found to have a luminescence quantum yield three times higher (26%) and a maximum 5d–4f emission peak that is bathochromically (to longer wavelengths) shifted into the yellow region of the electromagnetic spectrum (580 nm) with respect to its isostructural analogue, Eu^{II}**17**.¹⁵ Computational studies confirmed that the shift to a lower energy 4f–5d transition is a result of greater d-orbital splitting by the nitrogen donors of **23** with respect to the oxygen donors of **17**.⁷ The increase in quantum yield was attributed to the lack of solvent molecules directly bound to Eu^{II} in the crystal structure of Eu^{II}**23**. Eu^{II}**23** was also characterized in methanol for the purposes of photoredox catalysis,¹³ and an increase of quantum yield to 37% was observed with no appreciable shift in the 5d–4f emission peak. The increase in quantum yield was attributed to a decrease in the concentration of O–H oscillators in methanol relative to water.

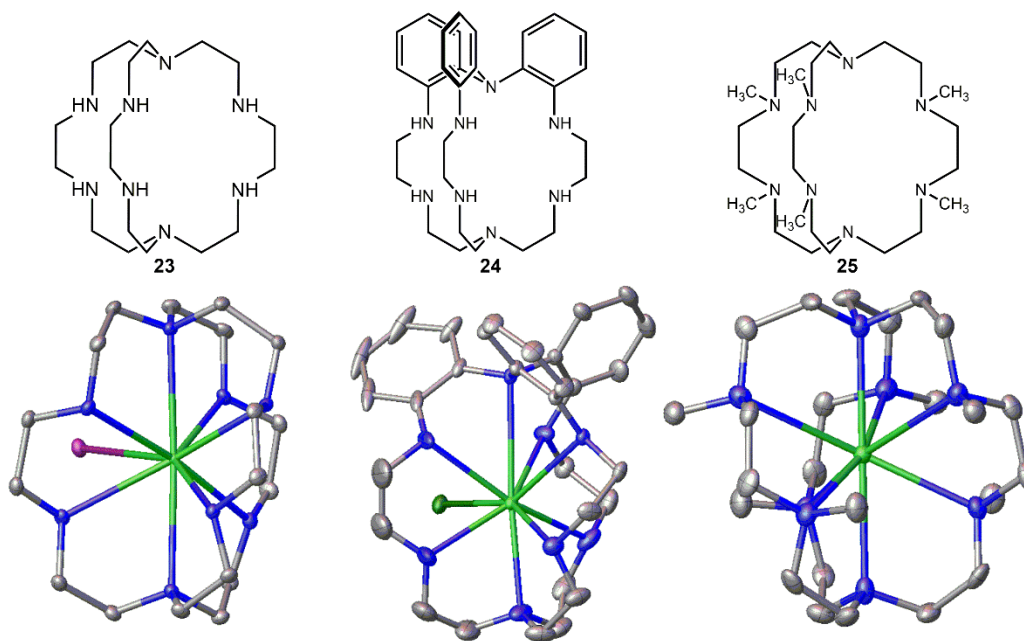


Figure 1.8 (Top) Nitrogenous cryptands used in the luminescence studies of divalent europium and (bottom) molecular structure of corresponding Eu^{II} -containing cryptates.^{35,36} Thermal ellipsoids are drawn at 50% probability. H atoms and non-coordinated solvent molecules and counteranions are omitted for clarity. Grey = carbon; blue = nitrogen; seagreen = europium; purple = iodide; and green = chloride.

Eu^{II} -containing complexes with **24** and **25**, which are derivatives of **23**, were also studied to probe the effect of electronics on the luminescence of Eu^{II} .^{35,36} The electron withdrawing nature of the benzo groups on **24** was expected to shift the 4f–5d transitions of Eu^{II} to higher energies and the methyl groups on **25** were expected to shift the 4f–5d transitions of Eu^{II} to lower energies with respect to **23**. However, both ligands induced shifts to higher-energy emissions with respect to **23**. The addition of benzo groups on **24** raised the energy of the 5d orbitals, leading to a hypsochromic (to shorter wavelengths) shift.³⁵ Cryptand **25**, however, was expected to induce a longer wavelength emission than **23** based on larger d-orbital splitting by the tertiary amines compared to secondary amines. Computational studies confirmed that the tertiary amines cause larger d-orbital splitting, but a change in geometry between $\text{Eu}^{\text{II}}\mathbf{23}$ and $\text{Eu}^{\text{II}}\mathbf{25}$ increased the energy gap between the 4f and 5d orbitals of Eu^{II} that overshadowed the effects of d-orbital

splitting. Another interesting aspect of $\text{Eu}^{\text{II}}\mathbf{25}$ is the remarkably large (47%) luminescence quantum yield that was attributed to the lack of N–H oscillators coordinated to Eu^{II} and the preclusion of innersphere interactions between Eu^{II} and solvent molecules by the sterically hindering methyl groups of $\mathbf{25}$.³⁶

1.2.3 Sandwich Complexes of Divalent Europium

Aside from macrocyclic complexes, another popular coordination motif for divalent lanthanide luminescence is sandwich or sandwich-like complexes. Sandwich complexes of divalent lanthanides have been known for their increased reactivity, but these complexes of divalent europium also have been shown to give rise to intense luminescence at longer wavelengths in the visible region of the electromagnetic spectrum (**Figure 1.9** and **Table 1.2**).^{37–}

42

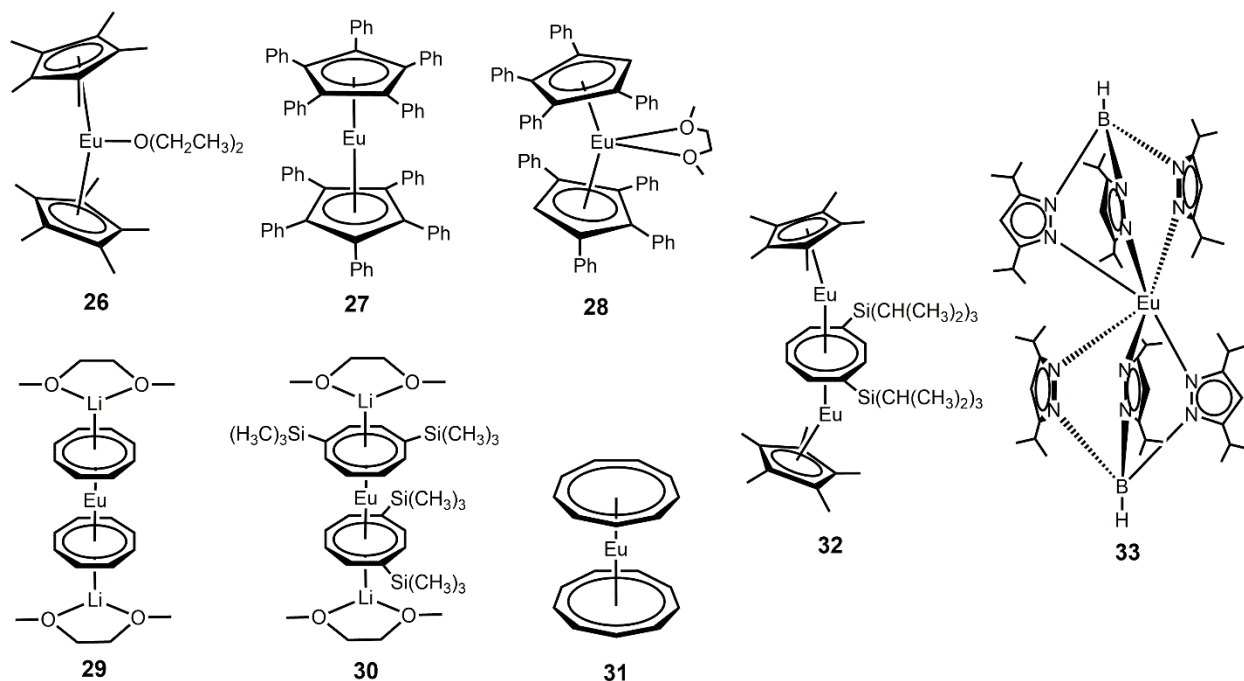


Figure 1.9 Eu^{II} -containing sandwich complexes.

Table 1.2 Luminescence properties of the Eu^{II}-containing sandwich complexes.

Eu ^{II} sandwich complex	Maximum emission wavelength (nm)	Luminescence quantum yield (%)	Solvent	Reference
26	730	4	toluene	38
27	616	45	toluene	37
28	645	41	toluene	37
29	623	2.4	toluene	39
30	594	21	toluene	39
31	516	1.0	toluene	40
32	509	<0.1	tetrahydrofuran	41
33	552	NR	<i>n</i> -pentane	42

NR = not reported

The divalent europium sandwich complexes **26–28** are similar in that they are cyclopentadienyl complexes that display 5d–4f emission in toluene.^{37,38} The Eu^{II} ions in **26** and **28** are also coordinated by diethyl ether and dimethoxyethane, respectively, presumably giving them a slightly bent geometry compared to the linear geometry reported for **27**. Assuming **26** and **28** maintain the same geometries in solution, the main difference in these complexes would be the electronics of their substituents. The methyl groups on **26** should donate more electron density than the aromatic moieties of **28**, resulting in greater d-orbital splitting and a longer-wavelength transition, consistent with the observations. Comparison of **26** and **28** to **27** revealed that the two bent complexes have more red-shifted emissions. More distorted geometries, such as bent versus linear in this case, lead to larger centroid shifts and, therefore, lower energy 5d–4f transitions.¹⁸

The luminescence of the structurally similar Eu^{II} sandwich complexes **29** and **30** have been examined in toluene.³⁹ The emission wavelengths for these two complexes are comparable at 623 and 594 nm for **29** and **30**, respectively. However, the peak width and Stokes shift are

larger for **29** than for **30**, indicating that **29** experiences a greater structural change between the ground and excited states. This difference in excited-state reorganization is explained by the steric bulk of the trimethylsilyl groups of **30** limiting the shortening of Eu^{II}–ligand bonds in the excited state. Additionally, the greater rigidity imparted by the trimethylsilyl groups and the restriction of bond shortening in the excited state cause an increase in luminescence quantum yield by approximately an order of magnitude for **30** relative to **29**. Another divalent europium sandwich complex with 5d–4f luminescence in toluene is **31**.⁴⁰ The coordinating rings are expanded by one carbon; there is an absence of lithium ions when compared to **29**; and **31** exhibits an emission at 516 nm that is blue shifted from **29** and **30**. Computations suggest that this shift to a higher energy transition is a result of a centroid shift of the 5d orbitals to energies farther from the 4f orbitals. This centroid shift is caused by a more widely distributed electrostatic potential for **31**, whereas the electrostatic potential in **29** is contained by the lithium ions capping each ring.

The weakly luminescent bimetallic Eu^{II} sandwich complex **32** was reported to display a 5d–4f emission at 509 nm in THF.⁴¹ Although this complex has an emission wavelength in a similar range as the other Eu^{II} sandwich complexes, the much smaller luminescence quantum yield sets it apart. The smaller quantum yield stems from nonradiative interactions between the two Eu^{II} ions in **32**, similar to the concentration quenching observed in solid-state luminescence when luminescent species occupy sites close enough together to promote nonradiative energy transfer.

Although it is not a traditional sandwich complex, sandwich-like **33** shares structural similarities to Eu^{II}-containing sandwich complexes.⁴² With a slightly bent geometry similar to **26** and **28**, the Eu^{II} ion in **33** displays a 5d–4f emission centered at 552 nm in *n*-pentane. The high

electron density of the borate ligands, nitrogenous donors, and lower symmetry of the bent geometry of **33** are likely responsible for the red-shifted emission with respect to other Eu^{II} -containing complexes.

1.2.4 Other Complexes of Divalent Europium

The solution-phase luminescence of two multimetallic Eu^{II} -containing complexes (**Figure 1.10**) have been reported.^{43,44} The mixed-valent trimetallic complex **34** contains two divalent europium ions and one trivalent europium ion coordinated by a field of bridging hexafluoroisopropoxide ligands (**Figure 1.10a**) and several molecules of dimethoxyethane.⁴³ The heterobimetallic trinuclear complex **35** consists of two Eu^{II} ions and one Y^{III} ion with a coordination sphere consisting of bridging hexafluoroisopropoxide and dimethoxyethane molecules, similar to **34**.⁴⁴ The electronics of the coordination spheres in these two complexes appear similar; however, **34** has a Eu^{II} -centered 5d–4f emission band at 330 nm whereas the same emission band for **35** is centered at 485 nm. This large discrepancy in emission wavelengths is likely due to differences in the coordination environments around the emissive Eu^{II} ions that influence splitting and centroid shift of the 5d orbitals.

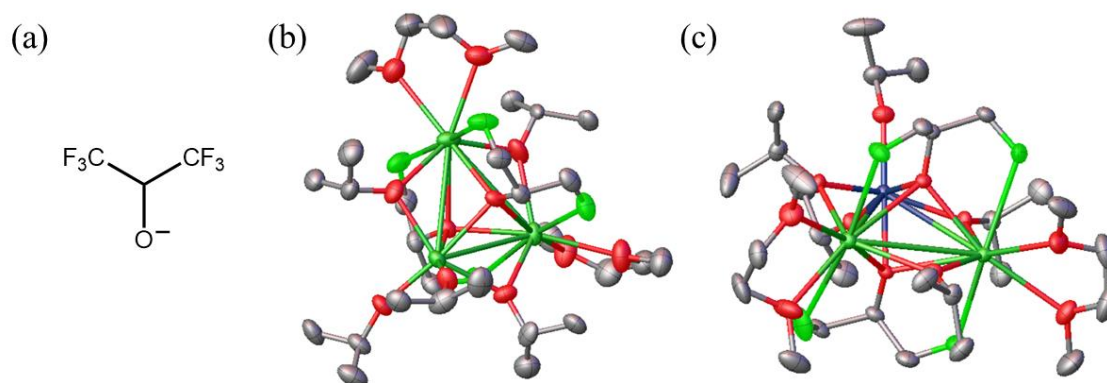


Figure 1.10 (a) hexafluoroisopropoxide ligand and molecular structures of (b) **34** and (c) **35**.^{43,44} Thermal ellipsoids are drawn at 50% probability. H atoms and non-coordinated F atoms are omitted for clarity. Grey = carbon; seagreen = europium; red = oxygen; green = fluorine; and blue = yttrium.

Along with the examination of macrocyclic ligands discussed in section 1.3.2, Adachi and co-workers explored the effects of polyethylene glycols on the luminescence of divalent europium.^{21,26} A series of five polyethylene glycols containing three to seven ethers were complexed with EuCl_2 and compared to the ligands in **Figure 1.5**. The polyethylene glycols enhanced Eu^{II} luminescence with respect to EuCl_2 but fell short of the enhancement observed with the macrocyclic complexes. The smaller enhancement was attributed to the absence of the macrocyclic effect in the polyethylene glycols and the presence of O–H oscillators on the terminal oxygens of the glycols. Longer polyethylene glycol chains imparted larger luminescence enhancement on Eu^{II} than the shorter chains, and this difference was attributed to larger denticities associated with the longer chains enabling closer to coordinative saturation of Eu^{II} and lower likelihood of coordinating to a terminal hydroxide.

The solution-phase luminescence of a Eu^{II} -containing complex with a trigonal planar geometry (**Figure 1.11**) was reported.⁴⁵ The Eu^{II} ion is coordinated by three equivalents of **36** and displays a 5d–4f emission centered at 540 nm in tetrahydrofuran. This emission wavelength for Eu^{II} is relatively long compared to many of the other complexes discussed so far and is probably due in part to the d-orbital splitting induced by the trigonal planar geometry. Another aspect that likely affects this bathochromic shift is the covalency of the metal–ligand bonds that shifts the energy of the 5d orbitals closer to the energy of the 4f orbitals.

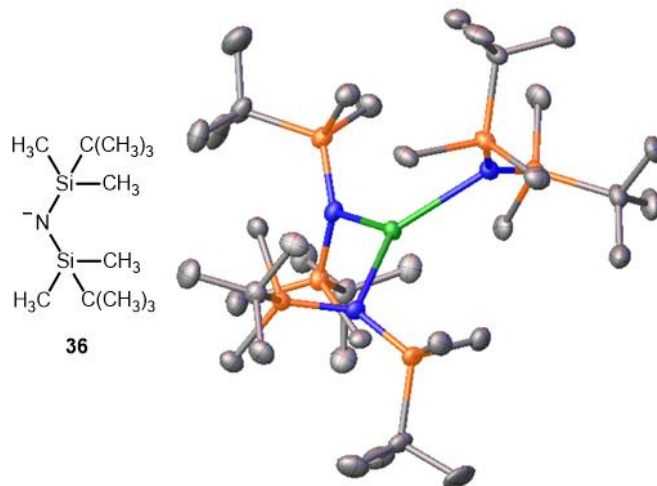


Figure 1.11 (Left) Structure of ligand **36** and (right) the molecular structure of the corresponding Eu^{II}-containing complex from a crystal.⁴⁵ Thermal ellipsoids are drawn at 50% probability. H atoms and non-coordinated counteranions and solvent molecules are omitted for clarity. Grey = carbon; seagreen = europium; orange = silicon; and blue = nitrogen.

As an extension of the divalent-europium-chemiluminescence system described in section 1.2.1, a series of europium complexes with β -diketonate ligands **37–39** and carboxylate ligand **40** was investigated (**Figure 1.12**).⁵ The reduction and excitation of the europium complexes by *i*-Bu₂AlH follows the same mechanism described in section 1.2.1, but some interesting changes in chemiluminescence were observed. The emission intensities of the complexes of Eu^{II} with β -diketonate ligands **37–39** and carboxylate ligand **40** were smaller than that of EuCl₂(THF)₂·*i*-Bu₂AlH, and the emission wavelengths were shifted from the blue to the green region of the electromagnetic spectrum with maxima between 550 and 565 nm. These shifts to longer wavelengths are indicative of increased d-orbital splitting and more covalent character of the bonds between Eu^{II} and **37–40** relative to the chloride salt.

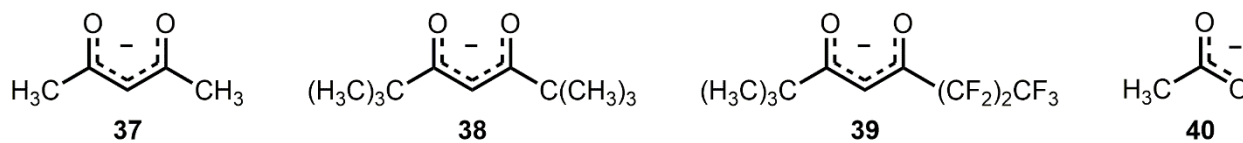


Figure 1.12 Ligands **37–40** used in chemiluminescence studies of divalent europium.⁵

1.3 Complexes of Divalent Ytterbium

Ytterbium has the most positive $\text{Ln}^{\text{III}}/\text{Ln}^{\text{II}}$ couple after europium, but at roughly 800 mV more negative, Yb^{II} is more challenging to stabilize than Eu^{II} .¹ Consequently, there are fewer reports of Yb^{II} luminescence in molecular complexes than for Eu^{II} . One of the interesting aspects of Yb^{II} luminescence is that it does not display 4f–4f transitions due to its full $4f^{14}$ ground state configuration and, therefore, only displays 4f–5d transitions. Yb^{II} tends to have 4f–5d transitions in a similar range as Eu^{II} but at lower intensities,^{3,17} and divalent ytterbium halides luminesce with peaks between 400 and 515 nm depending on anion and solvent.^{22,23,46,47}

The majority of studies of Yb^{II} luminescence use macrocyclic ligand scaffolds for the same reasons discussed for Eu^{II} . In one of the earliest solution-phase luminescence studies of Yb^{II} -containing complexes, Adachi and co-workers investigated the effect of crown ethers **1–3** on YbCl_2 in methanol.⁴⁶ Contrary to analogous studies with Eu^{II} , **1** and **2** had no effect on the spectroscopic properties of YbCl_2 . When complexed with **3**, however, the emission band maximum for YbCl_2 (~425 nm) was hypsochromically shifted to approximately 375 nm. An increase in quantum yield from 0.03 to 1% was also observed upon complexation that was ascribed to the coordinative girth of **3** limiting nonradiative interactions between solvent molecules and Yb^{II} ions.

The effects of cryptands **17**, **23**, **25**, and **41** on the luminescence of Yb^{II} in methanol were also explored.⁴⁷ All four cryptands induced a bathochromic shift in emission with respect to YbI_2 through a combination of d-orbital splitting and centroid shift (**Figure 1.13**). Following the well-established trends of the electrochemical series, the nitrogenous donors of **23** and **25** induced larger red shifts in emission than the oxygen donors of **17** and **41**. The Yb^{II} complexes with **17**, **23**, and **41** exhibited weak luminescence intensity, as is normal for Yb^{II} in solution; however,

$\text{Yb}^{\text{II}}\mathbf{25}$ displayed luminescence that is visible to the naked eye and approximately three orders of magnitude more intense than the other complexes. The lack of N–H oscillators coordinated to Yb^{II} and the preclusion of solvent– Yb^{II} ion interactions by the steric hindrance of the methyl groups was used to explain this enhancement of luminescence intensity.

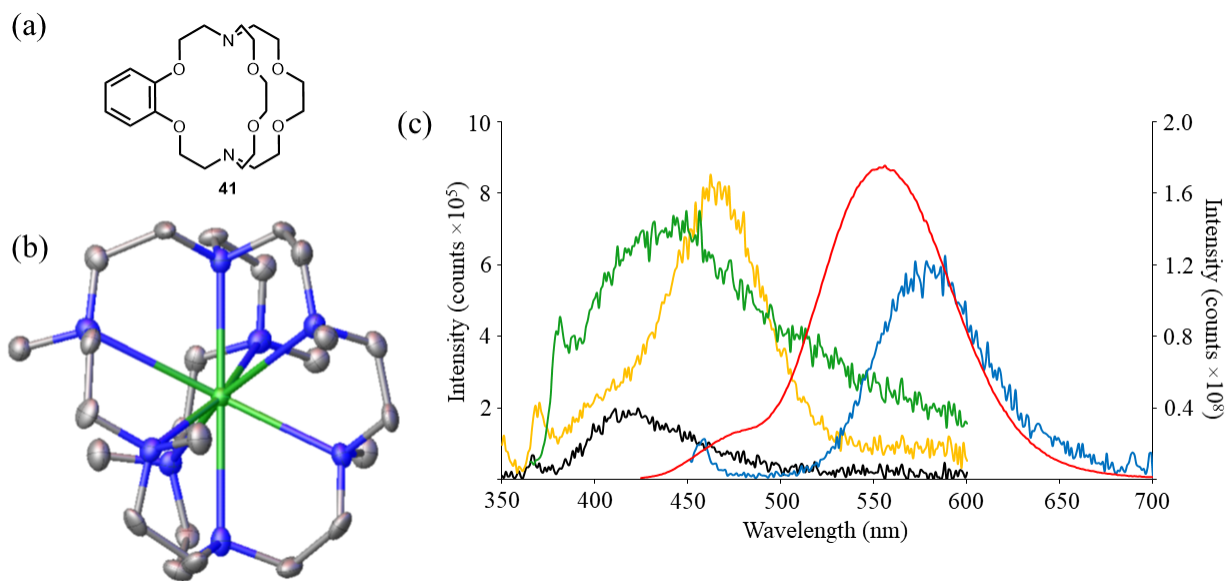


Figure 1.13 (a) Structure of cryptand **41**; (b) molecular structure of $\text{Yb}^{\text{II}}\mathbf{25}$; and (c) luminescence spectra of YbI_2 (black), $\text{Yb}^{\text{II}}\mathbf{17}$ (yellow), $\text{Yb}^{\text{II}}\mathbf{23}$ (blue), $\text{Yb}^{\text{II}}\mathbf{25}$ (red), and $\text{Yb}^{\text{II}}\mathbf{41}$ (green).⁴⁷ Thermal ellipsoids are drawn at 50% probability. H atoms and non-coordinated iodides are omitted for clarity. Grey = carbon; seagreen = europium; and blue = nitrogen. Emission spectra of YbI_2 , $\text{Yb}^{\text{II}}\mathbf{17}$, $\text{Yb}^{\text{II}}\mathbf{23}$, and $\text{Yb}^{\text{II}}\mathbf{41}$ are plotted against the left y-axis, and the emission spectrum of $\text{Yb}^{\text{II}}\mathbf{25}$ is plotted against the right y-axis.

The trigonal planar ligand scaffold consisting of three equivalents of **36** described earlier for Eu^{II} was also applied to Yb^{II} .⁴⁵ Unlike with europium, exciting at different peaks in the excitation spectrum for the divalent ytterbium complex led to 5d–4f emission at different wavelengths ($\lambda_{\text{em}} = 340$ nm when excited at 280 nm, $\lambda_{\text{em}} = 650$ nm when excited at 320 or 480 nm) in tetrahydrofuran. This dependency of emission wavelength on excitation wavelength indicates that the emission process from higher energy levels in the excited-state manifold is faster than nonradiative relaxation to the lowest energy level of the excited state. The longer

emission wavelength at 650 nm compared to the divalent ytterbium salts and macrocyclic complexes suggests that **36** may induce centroid shift and large splitting of the 5d orbitals of Yb^{II} . The bathochromic shift induced by **36** with respect to **23** and **25** follows expected trends based on the increased donor strength of the amides of **36** with respect to the amines of **23** and **25** (Figure 1.14).

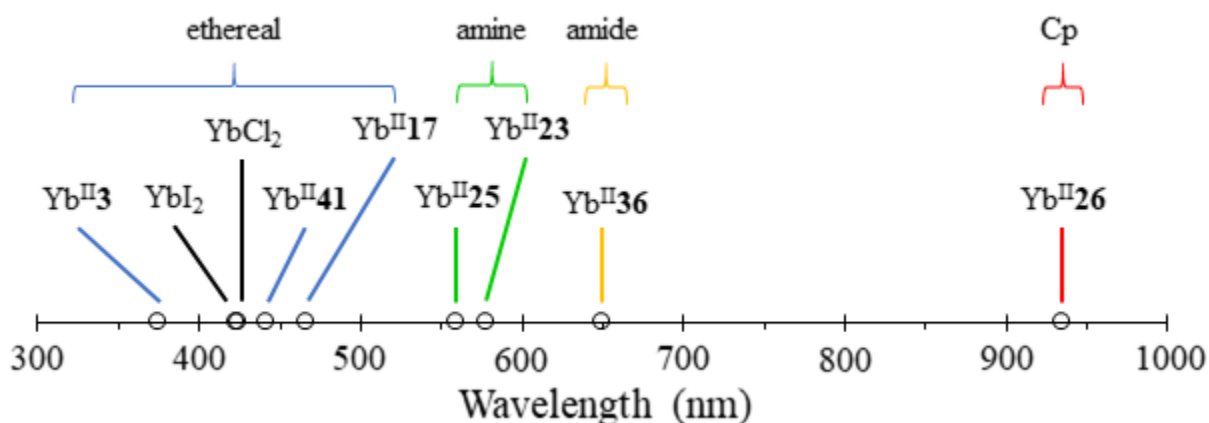


Figure 1.14 Maximum emission wavelengths of Yb^{II} -containing complexes classified by donor type.^{45–49}

Divalent ytterbium has also been shown to display 5d–4f luminescence when coordinated in a sandwich complex with pentamethylcyclopentadiene, **26**.^{38,48,49} The emission of this complex appears at wavelengths (900 and 935 nm) just outside the visible spectrum in toluene and tetrahydrofuran, respectively. This shift to longer wavelengths compared to other Yb^{II} -containing complexes is indicative of a more covalent interaction between the metal ion and ligand. Overall, the complexes of Yb^{II} that contained the strongest donors experienced the largest bathochromic shifts in emission wavelength.

1.4 Complexes of Divalent Samarium and Other Divalent Lanthanides

As with ytterbium, there are few reports of solution-phase luminescence of divalent samarium, largely due to its tendency to oxidize in solution. Because of its utility as a reductant in organic synthesis, a significant portion of the available research regarding the luminescence of divalent samarium in solution revolves around SmI_2 in tetrahydrofuran. The 5d–4f emission for the SmI_2 –THF adduct has been well-documented to occur at ~ 760 nm.^{14,23,50} With the addition of hexamethylphosphoramide, a common additive to enhance the reactivity of SmI_2 , the emission intensity of Sm^{II} decreases and the emission peak shifts to 820 nm.⁵⁰ This shift in luminescence to longer wavelength and lower quantum yield suggests that Sm^{II} forms a complex with hexamethylphosphoramide that has more covalent character than the complex without hexamethylphosphoramide because it is a strong donor.

One report of Sm^{II} -based luminescence in solution involved chemiluminescence systems similar to those described for europium in sections 1.2.1 and 1.2.4.⁵¹ The researchers found that $i\text{-Bu}_2\text{AlH}$ was capable of reducing $\text{SmCl}_3 \cdot 6\text{H}_2\text{O}$ in tetrahydrofuran and promoting chemiluminescence of the resulting complex of divalent samarium. Under the same mechanism described in section 1.2.1, $\text{SmCl}_2(\text{THF})_2$ was generated *in situ* giving rise to a Sm^{II} 5d–4f luminescence band centered at 780 nm. The Sm^{II} chemiluminescence was lower in intensity than that of $\text{EuCl}_2(\text{THF})_2 \cdot i\text{-Bu}_2\text{AlH}$ by five orders of magnitude, but the photoluminescence intensity was only two orders of magnitude smaller than that of the europium system. This difference is due in part to the inherently smaller luminescence efficiency of Sm^{II} relative to Eu^{II} in general. However, the greater difference between chemiluminescence intensities arises from the decreased energy overlap between triplet-excited isobutyric aldehyde ($\lambda_{\text{max}} = 23,256 \text{ cm}^{-1}$) and Sm^{II} ($\lambda_{\text{max}} = 12,821 \text{ cm}^{-1}$) with respect to Eu^{II} ($\lambda_{\text{max}} = 21,505 \text{ cm}^{-1}$).

In a study reporting the effect of macrocyclic ligands on the luminescence of Sm^{II}, **2** and **3** were complexed with SmI₂ in acetonitrile.⁵² Isothermal titration calorimetry, NMR spectroscopy, and crystal structure analysis revealed that Sm^{II} formed 2:1 and 1:1 ligand-to-metal complexes with **2** and **3**, respectively. Similar results to the studies regarding Eu^{II} luminescence were observed,⁹ with both crown ethers providing enhancement of luminescence with respect to SmI₂, which does not luminescence in acetonitrile. Complexes of Sm^{II} with **2** and **3** exhibited quantum yields of 30 and 0.04%, respectively. This enhancement by complexation with crown ethers was attributed to solvent exclusion.

While reports of divalent samarium luminescence in solution are scarce, there are even fewer reports for divalent lanthanides with more negative Ln^{III}/Ln^{II} electrochemical potentials than samarium. However, the luminescence of complexes of Sm^{II} and Tm^{II} coordinated by three equivalents of **36** have been reported (**Figure 1.15**).⁴⁵ These two complexes are structurally analogous to the trigonal planar complexes described earlier for Eu^{II} and Yb^{II}. The Sm^{II}-containing complex displays 5d–4f emissions at 360, 560, and 610 nm, depending on the wavelength of excitation. The dependence on excitation wavelength indicates that the 5d–4f emission for this divalent samarium complex originates from different energy levels within the excited state manifold much like the Yb^{II}-containing complex. The Tm^{II}-containing complex displays a 5d–4f emission band with a maximum at 545 nm that is not dependent on excitation wavelength.

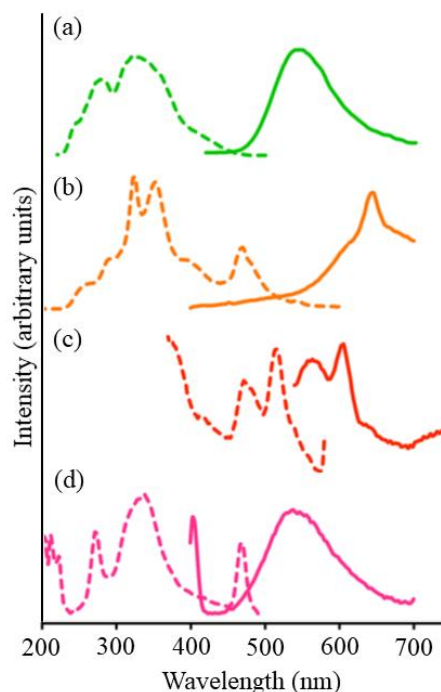


Figure 1.15 Excitation (dashed line) and emission (solid line) spectra of the complexes of (a) Eu^{II} , (b) Yb^{II} , (c) Sm^{II} , and (d) Tm^{II} with **36** in tetrahydrofuran (adapted from reference 45).

1.5 Summary

In summary, several coordination motifs have been described in relation to the luminescence divalent europium, ytterbium, samarium, and thulium in solution. The divalent lanthanide luminescence described in this chapter is dominated by 5d–4f transitions bearing broad, intense peaks compared to the 4f–4f transitions that dominate the luminescence of their trivalent counterparts. Strategies for the modulation of emission wavelength and enhancement of luminescence intensity were also described, with a focus on preventing interactions between solvent molecules and excited Ln^{II} ions primarily using principles of coordination chemistry. The observations made for these few lanthanide ions are likely translatable to complexes of other divalent lanthanides in solution, and as the study of those complexes becomes increasingly common, we expect that a rich body of luminescence studies will be reported.

1.6 Thesis Overview

The luminescence of divalent lanthanides, especially in solution, remains an underrepresented field in lanthanide chemistry. While the luminescence of divalent lanthanides in the solid state has been well studied, controlling the luminescence properties in solution presents a unique set of challenges. To improve upon the body of knowledge in the field of solution-phase divalent-lanthanide luminescence, this thesis describes the use of a luminescent divalent-europium-containing complex as a photoredox precatalyst, the effects of structural modifications on the luminescence properties of a divalent-europium-containing complex, and the effects of coordination environment on luminescence properties across the divalent-lanthanide series.

In Chapter 2, the use of a divalent europium complex in visible-light-promoted bond-forming reactions is reported. Stoichiometric and catalytic reductions using Eu^{II} and blue light are reported, and a substrate scope demonstrating the thermodynamic window of reactivity of the catalyst is discussed. The properties of the Eu^{II} -containing complex pertaining to photoredox catalysis including spectroscopic and electrochemical characterization are also explored. Finally, a catalytic cycle based on empirical evidence is proposed. The results of this chapter are foundational for future studies involving Eu^{II} -based photoredox catalysis.

In Chapter 3, I report a new luminescent Eu^{II} -containing complex that is based on the photoredox precatalyst discussed in Chapter 2. The complex is structurally modified to provide more steric bulk around the Eu^{II} ion, inciting surprising changes in the spectroscopic properties. The effect of structural properties on the spectroscopic properties of the complex are discussed. This chapter provides insight regarding structural factors that can lead to the enhancement of Eu^{II} luminescence intensity in solution.

In Chapter 4, the influence of coordination environment on complexes of Yb^{II} are reported and compared with analogous complexes of Eu^{II} . Four ligands with systematically varied electronic and steric characteristics are used to probe the coordination environment and electronic and redox properties of the corresponding Yb^{II} -containing complexes. Trends in properties across the series of Yb^{II} -containing complexes were compared to trends reported for the analogous Eu^{II} -containing complexes, revealing the translatability of coordination environment effects across the divalent lanthanide series. These studies provide valuable information regarding the behavior of small and medium-sized divalent lanthanides outside of the solid state.

In Chapter 5, a brief summary of the findings in Chapters 2–4 is provided and future directions in which this research can be directed is discussed.

CHAPTER 2: FIRST USE OF A DIVALENT LANTHANIDE IN VISIBLE-LIGHT-PROMOTED PHOTOREDOX CATALYSIS

Parts of this chapter were reproduced or adapted with permission from: Jenks, T. C.; Bailey, M. D.; Hovey, J. L.; Fernando, S.; Basnayake, G.; Cross, M. E.; Li, W.; Allen, M. J. “First use of a divalent lanthanide for visible-light-promoted photoredox catalysis” *Chem. Sci.* **2018**, 9, 1273–1278. – Published by The Royal Society of Chemistry.

In this chapter, “we” and other first-person plural pronouns are used in reference to all authors of this publication. My individual contributions to the research include execution of the photoredox reactions, cyclic voltammetry, and gas chromatography–mass spectrometry. Figures and tables containing data contributed by researchers other than me will contain a disclaimer in the caption; figures and tables with no disclaimer in the caption contain data collected by me. The materials and methods section represents my individual contributions to the publication.

2.1 Introduction

Metal-assisted photoredox catalysis uses light to promote the reactivity of metal-containing complexes in reactions such as halogen-atom abstractions, functional-group reductions, and carbon–carbon bond formations.^{53–77} Most reported metal-assisted photoredox systems rely on transition metals,^{68–75} with a small number of photoredox systems involving lanthanides that are either catalytic via the +3/+4 redox couple^{76–80} or noncatalytic starting from the +2 oxidation state.^{12,14,50,81–91} Among these metals, Eu^{II} is unique in that it is the mildest reducing agent of the divalent lanthanides. It can be handled in protic solvents including water; it can be produced from Eu^{III}, which is inexpensive relative to second and third row transition metals commonly used in photoredox catalysis; and it undergoes metal–orbital-based electronic transitions that are not susceptible to photobleaching like organic dyes.^{92,93} Recently, we reported

a luminescent, aqueous, Eu^{II}-containing complex that had a high quantum yield (26%) for a 5d–4f transition that occurred in the visible region of the electromagnetic spectrum using a ligand that can be prepared on large scale in two steps.^{7,15,94,95} We hypothesized that because this complex is luminescent and contains a redox-active metal, it could be employed in photoredox reactions with a sacrificial reducing agent to make the reaction catalytic in europium. Here, we report the first catalytic example of carbon–carbon bond formation using a europium-containing complex and visible light. Further, we evaluate the mechanism of the catalytic system.

2.2 Results and Discussion

Our photoredox system relies on azacryptand 1,4,7,10,13,16,21,24-octaazabicyclo[8.8.8]hexacosane, **23**, to encapsulate Eu^{II}, inducing a bathochromic shift in the UV–visible absorption of Eu^{II} from the UV to the visible region of the electromagnetic spectrum (**Figure 2.1**). This bathochromic shift arises from d-orbital splitting, caused by the nitrogen atoms of the cryptand, that results in a lower-energy 5d–4f transition relative to transitions induced by weaker field ligands.⁷ Upon absorption of blue light by Eu^{II}**23**, an electron is excited into an emissive state that has a luminescence lifetime of $0.98 \pm 0.03 \mu\text{s}$ and a quantum yield of 37% in methanol. The quantum yield of Eu^{II}**23** in methanol is 11% higher than the previously reported value for the same complex in a pH 12 aqueous solution,¹⁵ and the difference in the quantum yield is likely caused by the change of solvent. The luminescence lifetime of Eu^{II}**23** is in the range of typical photoredox systems.⁹⁶ Interestingly, both Eu^{II} and Ce^{III} are known to be emissive through 5d–4f transitions with typical lifetimes on the order of 1 ns to 1 μs .^{9,12,76,77,97} This range of lifetimes for similar electronic transitions suggests that these lifetimes are largely dependent on ligand field and not necessarily intrinsic to the metal ions. The values for lifetime and quantum yield are toward the long and high end, respectively, of reports for solvated

Eu^{II}.^{45,98} Due to the photophysical properties of Eu^{II}**23**, including the efficient conversion of visible light to a long-lived excited state, we hypothesized that Eu^{II}**23** would be a good promoter of photoredox reactions.

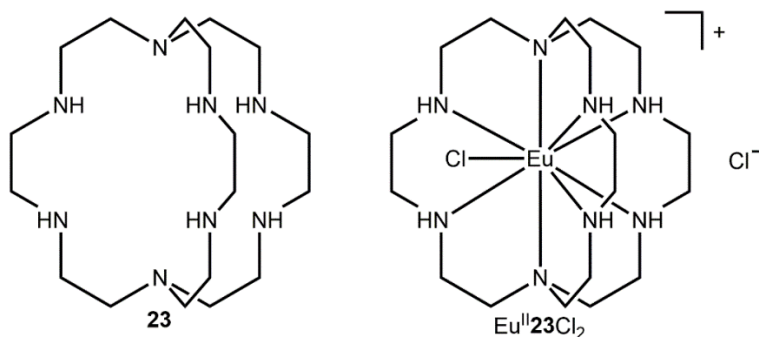


Figure 2.1 Structures of ligand **23** (left) and Eu^{II}**23** (right).

When a redox-active metal complex is excited to an emissive state, the $E_{1/2}$ of the complex changes.^{14,50,53–90} To estimate the $E_{1/2}$ of Eu^{II}**23** in the emissive state, the excited-state potential ($E_{1/2}^*$) was calculated by means of the Rehm–Weller formalism (**Equation 2.1**) using the ground-state potential ($E_{1/2}$) and the energy of the emission band ($E_{0,0}$), which is the energy of an electron in the excited state relative to the ground state as determined by the maximum emission wavelength (**Figure 2.2**).^{99,100} There is an additional work-function term that has been omitted from **Equation 2.1** because it was assumed to be negligibly small.⁷⁸ To determine the ground-state potential of Eu^{II}**23**, cyclic voltammetry was performed with Eu^{II}**23** in *N,N*-dimethylformamide. A reversible Eu^{II/III}**23** couple was observed with an $E_{1/2}$ of -0.90 V vs. Ag/AgCl, which represents a negative shift in the $E_{1/2}$ potential relative to the solvated Eu^{II/III} couple, and the negative shift is consistent with other reported Eu^{II} complexes that contain nitrogen donors.^{101–104} $E_{0,0}$ was estimated to be 2.14 V by dividing the product of Planck's constant and the speed of light by the maximum emission wavelength (580 nm) in meters (hc/λ). Using these values for the ground-state potential and the emission-band energy, the $E_{1/2}^*$ of Eu^{II}**23** was calculated to be -3.0 V vs. Ag/AgCl. This calculated excited-state potential is among

the most negative excited-state potentials reported to date for metal-based catalytic photoredox agents and is more negative than the potential of the potent reducing agent SmI₂ in the presence of hexamethylphosphoramide.^{78,105} With a sense of the redox properties of Eu^{II}**23** in hand, we were interested in probing the reactivity of Eu^{II}**23**. On the basis of a recent report from the Schelter group describing photocatalytic reductive couplings using a Ce^{III/IV} system,^{76,77} we expected that Eu^{II}**23** would display similar reactivity.

Equation 2.1
$$E_{1/2}^* = E_{1/2} - E_{0,0}$$

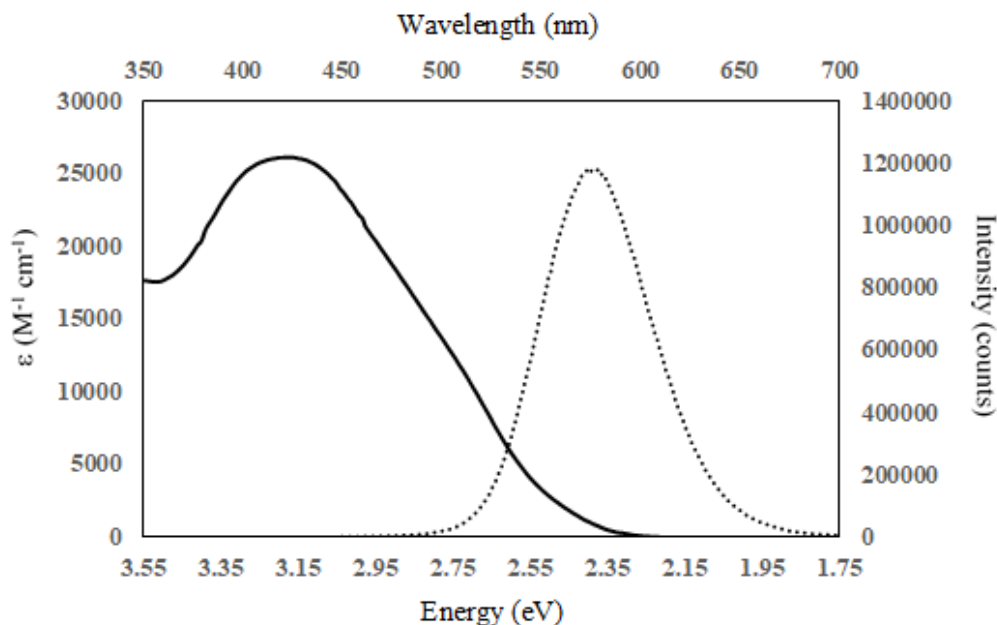


Figure 2.2 UV–visible absorption spectrum of Eu^{II}**23**Cl₂ (—, left y-axis) and emission spectrum ($\lambda_{\text{ex}} = 460$ nm, ϵ : 1044 M⁻¹ cm⁻¹) of Eu^{II}**23**Cl₂ (••, right y-axis). Spectra were acquired in methanol. Data collected by Matthew D. Bailey.

To study the reactivity of Eu^{II}**23**, we attempted to reductively couple alkyl halides to form carbon–carbon bonds. A solution containing EuCl₂ (1 equivalent), **23** (1 equivalent), and benzyl chloride (1 equivalent, 0.027 mmol) in methanol was illuminated with blue light (~ 7.6 W, $\lambda_{\text{em}} = 460$ nm) using a strip of light-emitting diodes. We observed the formation of 1,2-diphenylethane ($85 \pm 2\%$) and toluene ($4.7 \pm 0.4\%$) within 30 minutes (**Figure 2.3A**).¹⁰⁶

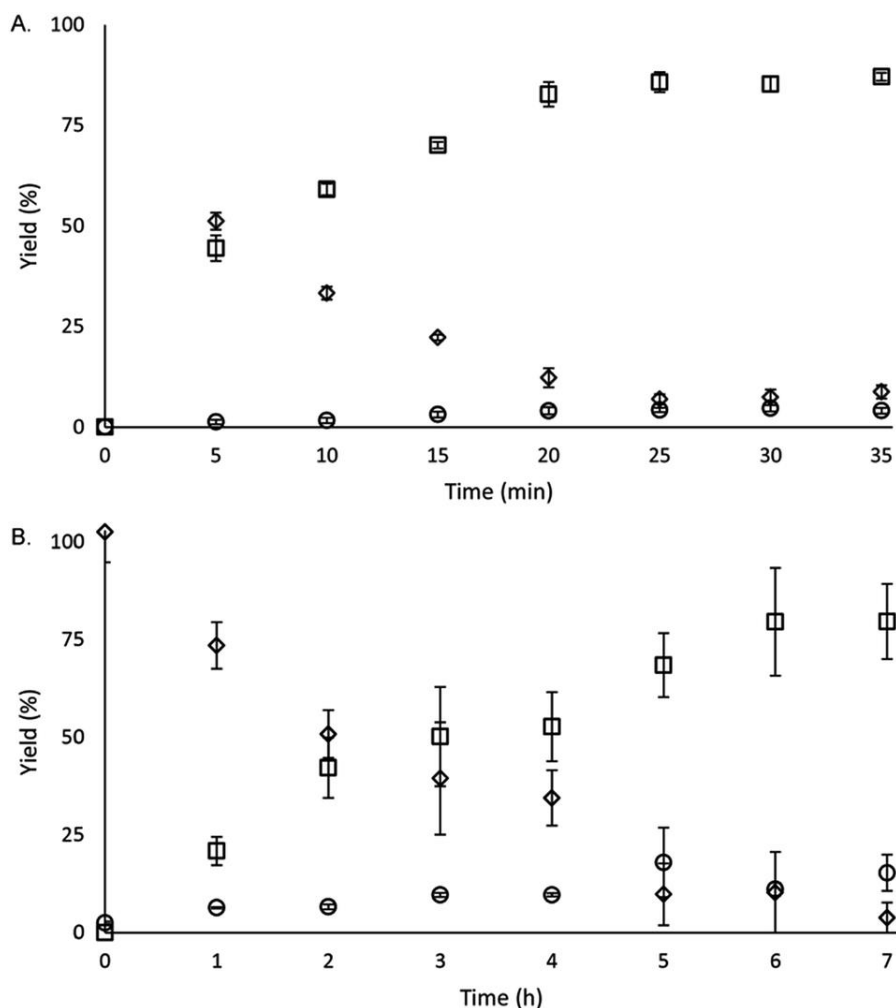


Figure 2.3 Formation of products and disappearance of starting material as a function of time for (A) stoichiometric and (B) catalytic (10 mol%) benzyl chloride coupling reactions (squares = 1,2-diphenylethane, diamonds = benzyl chloride, and circles = toluene). Each point is the mean of three independently prepared reactions, and the error bars represent the standard error of the means.

To determine whether the reaction was promoted by the excited state of $\text{Eu}^{\text{II}}\mathbf{23}$, we performed three control reactions (**Table 2.1**). When the coupling of benzyl chloride was attempted in the absence of light, no product was observed. This observation indicated that for the reaction to proceed, light must be present, suggesting that the excited state of $\text{Eu}^{\text{II}}\mathbf{23}$ was promoting the reaction and not the ground state of $\text{Eu}^{\text{II}}\mathbf{23}$. When ligand **23** was omitted, no product was observed. This observation indicated that uncomplexed europium ions are incapable of performing the reductive coupling. When EuCl_2 was omitted, no product was observed,

indicating that europium is an active participant in the reduction of benzyl chloride. The control reactions demonstrate that light, ligand **23**, and europium are all necessary to reduce benzyl chloride. To test for reactivity with methanol, fluorescence spectroscopy was performed before and after 12 hours of light exposure on samples of Eu^{II}**23** (**Figure A2.1**). Based on these studies, the excited state of Eu^{II}**23** reacts with methanol, but no reaction with methanol was observed over the same time period in the dark. Despite the reactivity of the excited state of Eu^{II}**23** with methanol, the observation of 1,2-diphenylethane in excellent yields in 30 minutes indicates that the reaction with methanol is relatively slow. To further understand how Eu^{II}**23** promotes light-induced bond formation, we attempted to determine the mechanism of electron transfer.

Table 2.1 Stoichiometric control reactions.

Conditions	Yield ^a
Unmodified	85 ± 2%
Dark	No reaction
No 23	No reaction
No Eu	No reaction

^aDetermined by gas chromatography–mass spectrometry.

The emissive state of Eu^{II}**23** is responsible for the observed reactivity, and it is unlikely that energy transfer occurs between the emissive state of Eu^{II}**23** and benzyl chloride as shown by the lack of spectral overlap between the absorption of benzyl chloride and the emission of Eu^{II}**23**; therefore, the reductive coupling of benzyl chloride must occur through a photoinduced electron transfer, which would be expected to quench luminescence. We sought to investigate the mechanism of photoinduced electron transfer using substrates to quench luminescence with Stern–Volmer analyses.¹⁰⁷ We measured the rate of quenching (k_q) of the excited-state intensity (I) as function of concentration of substrates (**Table 2.2**). Additionally, we measured k_q at three

different temperatures for benzyl chloride and attempted to obtain lifetime quenching data. Entries 1 and 2 showed no detectable quenching of luminescence with Eu^{II}**23**, unlike entries 3 and 4 (**Table 2.2**). For entries 3 and 4, plots of I_0/I versus concentration of quencher resulted in the observation of linear relationships (**Figure A2.2**). The linear relationships are indicative of well-behaved bimolecular quenching interactions that can be either collisional or static in nature.¹⁰⁷ Furthermore, k_q increased with increasing temperature, suggesting that the quenching is likely due to a diffusion-limited, collisional mechanism and is not static in nature (**Figure A2.3**). The collisional mechanism eliminates the possibility of the participation of a preorganized benzyl chloride adduct of Eu^{II}**23** in the reaction. These results are consistent with the reaction of benzyl bromide with divalent europium in the presence of crown ethers.¹² In both cases, the values of k_q differ from the idealized collisional bimolecular quenching constant ($10^{10} \text{ M}^{-1} \text{ s}^{-1}$).¹⁰⁷ These differences are likely due to coordinative saturation of Eu^{II}, causing a lower frequency of productive collisions between Eu^{II} and substrates compared to idealized lumophores.

Table 2.2 Stern–Volmer data.

Entry	Quencher	E_{pc} of quencher (V vs Ag/AgCl)	$k_q^{[a]}$ ($\times 10^7 \text{ M}^{-1} \text{ s}^{-1}$)	Product	Yield ^b (%)
1	(CH ₃) ₃ CCl	-3.05	0 ^c	((CH ₃) ₃ C) ₂	1.9 ± 0.1
2	C ₆ H ₅ Cl	-2.93	0 ^c	C ₆ H ₆	5.4 ± 0.4
3	CH ₂ CHCH ₂ Cl	-2.35	8.5	(CH ₂ CHCH ₂) ₂	46 ± 2
4	C ₆ H ₅ CH ₂ Cl	-2.34	73	(C ₆ H ₅ CH ₂) ₂	85 ± 2

^aData collected by Matthew D. Bailey.

^bDetermined by gas chromatography–mass spectrometry.

^cNo quenching of the excited state was observed.

To explain the apparent selectivity observed in the Stern–Volmer analyses, cyclic voltammetry was performed for the complex and substrates (**Table 2.2**). The peak cathodic

potentials of the substrates that showed no quenching of luminescence (E_{pc} of entries 1 and 2 in **Table 2.2**) are close to or more negative than the calculated $E_{1/2}^*$ of $\text{Eu}^{\text{II}}\mathbf{23}$. Because reliable cyclic voltammetry of $\text{Eu}^{\text{II}}\mathbf{23}$ could not be obtained in methanol, the $E_{1/2}$ of $\text{Eu}^{\text{II}}\mathbf{23}$ recorded in *N,N*-dimethylformamide might have resulted in a more negative value of $E_{1/2}$ than would be present in methanol, propagating to a more negative estimation of $E_{1/2}^*$. However, the E_{pc} of the substrates that quenched the luminescence of the excited state of $\text{Eu}^{\text{II}}\mathbf{23}$ (entries 3 and 4 in **Table 2.2**) are between the calculated $E_{1/2}^*$ and ground-state $E_{1/2}$ of $\text{Eu}^{\text{II}}\mathbf{23}$, consistent with the difference in reactivity of $\text{Eu}^{\text{II}}\mathbf{23}$ with benzyl chloride in the light and dark. Furthermore, allyl chloride, which has an E_{pc} more positive than the $E_{1/2}^*$ of $\text{Eu}^{\text{II}}\mathbf{23}$, also shows expected product formation in the light (**Table 2.2**). Based on the cathodic potentials and lack of observed luminescence quenching, we would not expect chlorobenzene and 2-chloro-2-methylpropane to react with the excited state of $\text{Eu}^{\text{II}}\mathbf{23}$; however, products were observed for these two substrates in yields of 1.9 and 5.4%, respectively. These data point toward a thermodynamic window of selectivity (-0.9 to approximately -3 V vs. Ag/AgCl) that is unique for $E_{1/2}^*$.

With an understanding of the electron transfer mechanism of $\text{Eu}^{\text{II}}\mathbf{23}$, we were interested in moving from reactions that were stoichiometric in Eu to reactions that were catalytic in Eu. To enable catalysis, a sacrificial reducing agent was needed, and it is known that Eu^{III} can be reduced to Eu^{II} *in situ* with Zn^0 .^{34,104} To ensure that $\text{Eu}^{\text{II}}\mathbf{23}$ could be assembled *in situ* from Eu^{III} , $\mathbf{23}$, and Zn^0 , UV–visible and fluorescence spectroscopies were performed on a mixture of EuCl_3 , Zn^0 , and $\mathbf{23}$. Absorption at wavelengths >400 nm and a broad emission between 500 and 700 nm, which are both characteristic of $\text{Eu}^{\text{II}}\mathbf{23}$, indicated that $\text{Eu}^{\text{II}}\mathbf{23}$ can be assembled *in situ* (**Figures A2.4** and **A2.5**). Furthermore, X-ray diffraction of material nucleated from a mixture of EuCl_3 , Zn^0 , and $\mathbf{23}$ in methanol provides direct evidence that $\text{Eu}^{\text{II}}\mathbf{23}$, as well as oxidized zinc species,

are formed under the reaction conditions (**Figure 2.4**). The crystal structure in **Figure 2.4** is from a crystal isolated from the reaction mixture. Although several crystals formed, a yield was not determined. However, because it nucleated from a reaction mixture in which Eu^{II} was not directly added, this structure demonstrates that Zn^0 is able to complete the catalytic cycle by either reducing EuCl_3 followed by metalation with **23** or by reducing $\text{Eu}^{\text{III}}\mathbf{23}$ to $\text{Eu}^{\text{II}}\mathbf{23}$. Direct evidence of the reduction of Eu^{III} to Eu^{II} can be found in the Eu–N bond distances between Eu and the ligand [2.7116(10)–2.7484(10) Å for secondary amines and 2.8030(11)–2.8333(10) Å for tertiary amines] that are in the expected range for $\text{Eu}^{\text{II}}\text{–N}$ bonds.^{15,33,35} In the structure in **Figure 2.4**, unlike with the previously reported structure of $\text{Eu}^{\text{II}}\mathbf{23}$, there was no inner-sphere chloride, and the associated anion was ZnCl_4^{2-} instead of two equivalents of Cl^- , indicating oxidation of Zn^0 and demonstrating the formation of $\text{Eu}^{\text{II}}\mathbf{23}$ via reduction of Eu^{III} by Zn^0 .

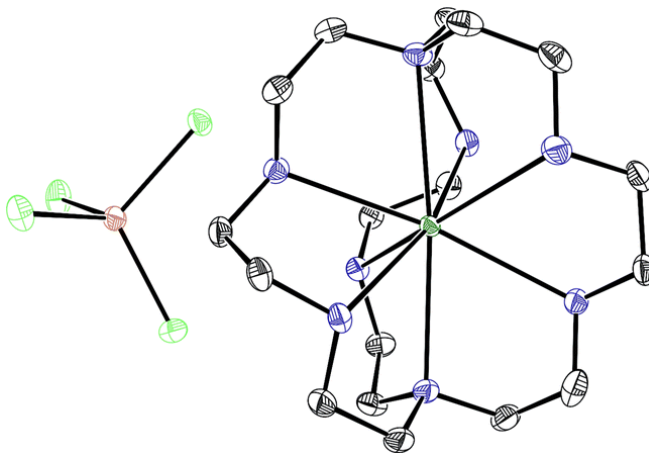


Figure 2.4 Crystal structure of $[\text{Eu}^{\text{II}}\mathbf{17}][\text{ZnCl}_4]$ generated from a mixture of EuCl_3 , Zn^0 , and **17** in methanol. Thermal ellipsoids are drawn at 50% probability. Crystallographic data for this structure has been deposited at the Cambridge Crystallographic Data Centre under deposition number CCDC 1539923. H atoms and an outer-sphere molecule of methanol have been omitted for clarity. Grey = C; blue = N; seagreen = Eu; green = Cl; and brown = Zn. Data collected by Matthew D. Bailey.

To ensure that Zn^0 could not promote the reductive coupling of benzyl chloride, a control experiment was performed with Zn^0 , light, and benzyl chloride. Only the formation of toluene was observed after six hours, indicating that Zn^0 does not promote the reductive coupling of

benzyl chloride. To probe whether Zn^0 promoted the formation of toluene, another control experiment was performed that only included benzyl chloride, methanol, and light. This experiment showed no formation of toluene, indicating that Zn^0 induces the reduction of benzyl chloride to toluene.

Knowing that $\text{Eu}^{\text{II}}\mathbf{23}$ can be formed in situ and that Zn^0 does not promote the reductive coupling of benzyl chloride, we wanted to probe the catalytic activity of $\text{Eu}^{\text{II}}\mathbf{23}$. A benzyl chloride coupling reaction was performed starting from EuCl_3 (10 mol%) and $\mathbf{23}$ (10 mol%). This reaction yielded 1,2-diphenylethane ($80 \pm 10\%$) and toluene ($11 \pm 2\%$) in six hours (**Figure 2.3B**). The variation in yields is likely due to the heterogeneity of the reaction mixture and small differences in stir rate, causing a variability in light penetration. These experiments demonstrate that the photoredox reaction can be rendered catalytic (~ 8 turnovers) in europium.

To determine how catalyst loading influenced product formation, the loading of EuCl_3 and $\mathbf{23}$ were systematically varied, keeping ten equivalents of Zn^0 relative to benzyl chloride constant, and yields were compared at six hours. Benzyl chloride coupling reactions were performed at catalyst loadings of 5, 1, and 0.5 mol%. Yields of 1,2-diphenylethane of $71 \pm 5\%$ (~ 14 turnovers), $70 \pm 5\%$ (~ 70 turnovers), and $60 \pm 3\%$ (~ 120 turnovers), respectively, were observed. Toluene was also formed at yields of 12 ± 2 , 21 ± 2 , and $26 \pm 1\%$ for 5, 1, and 0.5% catalyst loadings, respectively. This trend demonstrates that decreased catalyst loading correlates to increased toluene production. At a much lower catalyst loading (0.005%), only toluene formation was observed. These results indicate that the precatalyst operates efficiently at low concentrations but is likely in competition with zinc for reduction versus reductive coupling.

After examining the catalytic utility of $\text{Eu}^{\text{II}}\mathbf{23}$, we were interested in examining the effect of water on the system because all of the reactions to this point were performed under anhydrous

conditions. To introduce water into the system, $\text{EuCl}_3 \cdot 6\text{H}_2\text{O}$ was used as the Eu^{III} source and the samples were prepared in a wet glovebox (water allowed but no molecular oxygen). Reactions of the catalytic reductive coupling of benzyl chloride under these wet conditions were prepared at 10 mol% catalyst loading, and the formation of 1,2-diphenylethane in yields of $80 \pm 3\%$ was observed. These yields are not different from those of reactions performed under anhydrous conditions, indicating that small amounts of water have no significant effect on the performance of the precatalyst.

To determine if Eu^{III} remains complexed after the oxidation of Eu^{II} , luminescence intensities were compared of solutions containing EuCl_3 , EuCl_3 in the presence of **23**, and $\text{Eu}^{\text{II}}\mathbf{23}$ that was opened to air to oxidize (**Figure A2.6**). The spectra were normalized to the $^5\text{D}_0 \rightarrow ^7\text{F}_1$ transition at 591 nm that is insensitive to ligand environment, and the emission intensities of the spectra were compared at the $^5\text{D}_0 \rightarrow ^7\text{F}_2$ transition (610–630 nm) that is hypersensitive to ligand environment.^{108,109} The change in spectral profile of the $^5\text{D}_0 \rightarrow ^7\text{F}_2$ transitions indicates that there is an interaction between Eu^{III} and **23**, but the exact nature of this interaction is ambiguous.

Based on the data presented here, we propose that the photocatalytic reductive coupling of benzyl chloride using $\text{Eu}^{\text{II}}\mathbf{23}$ proceeds through the catalytic cycle shown in **Figure 2.5**. From luminescence experiments, $\text{Eu}^{\text{II}}\mathbf{23}$ is excited by blue light into an excited state ($\text{Eu}^{\text{II}}\mathbf{23}^*$). Two molecules of $\text{Eu}^{\text{II}}\mathbf{23}^*$ reduce two molecules of substrate through a collisional electron transfer based on Stern–Volmer analyses, followed by reductive coupling of substrate molecules. The electron transfer also generates Eu^{III} that interacts with **23** to some extent. Zn^0 reduces Eu^{III} to Eu^{II} either as the complex or the uncomplexed ion. Spectroscopic evidence (**Figure A2.6**) supports the presence of interactions between Eu^{III} and **23**, but this evidence is not conclusive with respect to the nature of speciation of the trivalent ion. Regardless of the extent of

encapsulation of Eu^{III} by **23**, reduction by Zn^0 regenerates $\text{Eu}^{\text{II}}\mathbf{23}$, evidenced by spectroscopy and the crystal structure in **Figure 2.4**, restarting the catalytic cycle.

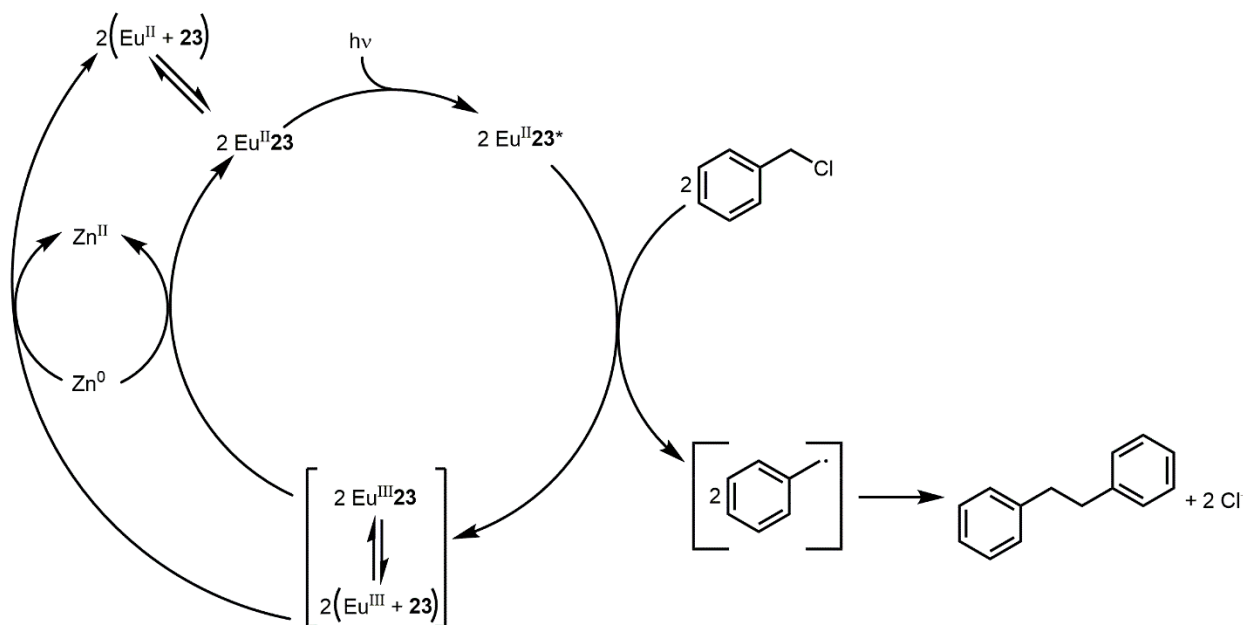


Figure 2.5 Proposed catalytic cycle.

2.3 Summary

We have described the first report of photoredox catalysis based on europium. Exposure of $\text{Eu}^{\text{II}}\mathbf{23}$ to visible light forms an excited state with a calculated electrochemical potential that rivals SmI_2 in the presence of hexamethylphosphoramide, has a long luminescence lifetime, is tolerant of protic solvents and some H_2O , and can be assembled *in situ* starting from air-stable and relatively inexpensive $\text{EuCl}_3 \cdot 6\text{H}_2\text{O}$. We expect that the mechanistic insight provided here will open the door for the study of visible-light-promoted photoredox catalysis using $\text{Eu}^{\text{II}}\mathbf{23}$ in reactions that require large negative electrochemical potentials between -0.9 and approximately -3 V vs. Ag/AgCl , including challenging systems like unactivated halides such as aryl bromides. Furthermore, studies from our laboratory have shown that ligand modifications to $\text{Eu}^{\text{II}}\mathbf{23}$ can influence its spectroscopic properties,³⁵ and these modifications are likely to impact excited-state

redox properties. Studies exploring ligand modifications and the scope of reactivity of Eu^{II}**23** are underway in our laboratory.

2.4 Materials and Methods

2.4.1 Experimental Procedures

Commercially available chemicals were of reagent-grade purity or better and were used without further purification unless otherwise noted. DriSolv anhydrous methanol and liquid substrates were degassed under reduced pressure prior to being brought into gloveboxes. Non-degassed substrates and ACS-grade methanol were used for reactions prepared outside of the gloveboxes. Water was purified by using a PURELAB Ultra Mk2 water purification system (ELGA). Azacryptand 1,4,7,10,13,16,21,24-octaazabicyclo[8.8.8]hexacosane (**23**) was prepared by following a published procedure.^{94,95}

Photoreactors (**Figures A2.7** and **A2.8**) were assembled using strips of multicolored light emitting diodes (LEDs) purchased from Lighting Ever (SKU 4100053-US, <http://www.lightingever.com/rgb-led-strip-non-waterproof-4100053-us-a.html>, accessed on 08/26/2016). Each reactor consisted of approximately 47 LEDs (0.16 W per LED) resulting in a total of ~7.6 W of light for each reactor. Reactors were placed on top of stir plates and fans (Vornado Flippi V6 Personal Air Circulator) were used to cool the reactors.

Stoichiometric reactions were prepared in a dry glovebox under an atmosphere of N₂. Samples of Eu^{II}**23** were prepared by mixing solid **23** (103.0–107.9 mg, 0.2779–0.2912 mmol, 1 equiv) with solid EuCl₂ (62.1–63.9 mg, 0.279–0.287 mmol, 1 equiv) and diluting with methanol to a total volume of 10.0 mL. The resulting solution was stirred for two hours to yield a solution of Eu^{II}**23** (27.8–28.7 mM). Benzyl chloride solutions were prepared by diluting benzyl chloride (30.7–37.9 mg, 0.243–0.299 mmol, 1 equiv) with methanol to a total volume of 10.0 mL to make

a benzyl chloride solution (24.3–29.9 mM). Reactions were prepared by adding the benzyl chloride solution (1.00 mL), the Eu^{II}**23** solution (1.00 mL), and methanol (1.00 mL) to a 20 mL vial equipped with a Teflon-coated stir bar. Vials were sealed with electrical tape, brought out of the glovebox, and placed in photoreactors to be illuminated with blue LEDs. For time progression studies, eight identical reaction vessels were set up simultaneously from the same stock solutions. Starting at zero min (before irradiation), one reaction was stopped every five min for 35 min. After completion, each reaction mixture was removed from the photoreactor and diluted to 10.0 mL in ACS-grade methanol for analysis by GC–MS using method A (see GC–MS section 2.4.2 below).

Substrate scope reactions were performed at stoichiometric catalyst concentrations as described in the stoichiometric reaction section and were prepared in a dry glovebox under an atmosphere of N₂. Eu^{II}**23** stock solutions were prepared as described in the stoichiometric reaction section. Substrate solutions were prepared by diluting the requisite amount of substrate (18.4–23.6 mg, 0.240–0.308 mmol, 1 equiv allyl chloride; 27.8–33.8 mg, 0.247–0.300 mmol, 1 equiv chlorobenzene; and 25.3–39.5 mg, 0.273–0.427 mmol, 1 equiv 2-chloro-2-methylpropane) with methanol to a total volume of 10.0 mL. Reactions were prepared by the respective substrate solution (1.00 mL), the Eu^{II}**23** solution (1.00 mL), and methanol (1.00 mL) to a 20 mL vial equipped with a Teflon-coated stir bar. Vials were sealed with electrical tape, brought out of the glovebox, and placed in photoreactors to be illuminated with blue LEDs for 30 min. Each reaction was extracted with GC–MS-grade *n*-pentane (5×3 mL) and the *n*-pentane extract was used for GC–MS analysis using method B for the allyl chloride and 2-chloro-2-methylpropane reactions and method C for the chlorobenzene reactions (see GC–MS section 2.4.2 below).

Catalytic reactions (10% catalyst loading) starting from EuCl_3 were prepared in a dry glovebox, and catalytic reactions starting from $\text{EuCl}_3 \cdot 6\text{H}_2\text{O}$ were prepared in a wet glovebox. Both the dry and wet gloveboxes operate under an atmosphere of N_2 . Separate stock solutions of **23** (101.2–105.7 mg, 0.273–0.285 mmol, 0.1 equiv), EuCl_3 (71.9–73.6 mg, 0.278–0.285 mmol, 0.1 equiv), and $\text{EuCl}_3 \cdot 6\text{H}_2\text{O}$ (103.1–113.0 mg, 0.281–0.308 mmol, 0.1 equiv) were prepared by dissolving the respective solid in methanol and diluting to 10.0 mL. Benzyl chloride stock solutions were prepared by diluting benzyl chloride (337.1–364.4 mg, 2.663–2.879 mmol, 1 equiv) with methanol to a total volume of 10.0 mL. Reactions were prepared by adding the benzyl chloride solution (1.00 mL), the respective Eu^{III} solution (1.00 mL), and the solution of **23** (1.00 mL) to a 20 mL vial containing approximately 176 mg of zinc dust (~10 equiv vs substrate) and a Teflon-coated stir bar. Reaction vessels were sealed with electrical tape before removal from the glovebox. Reactions were stirred for two hours in the dark prior to being illuminated by blue LEDs. For time-progression studies, eight identical reaction vessels were prepared simultaneously from the same stock solutions. Starting at zero hours (after the two-hour stirring period but before irradiation), one reaction was stopped every hour for seven hours. After completion, each reaction mixture was removed from the photoreactor, filtered through Celite to remove zinc, and diluted to 100.0 mL in ACS-grade methanol for analysis by GC–MS using method A (see GC–MS section 2.4.2 below).

Catalytic loading reactions (5, 1, and 0.5% catalyst loadings) were prepared in a dry glovebox under an atmosphere of N_2 . Benzyl chloride stock solutions were prepared by diluting benzyl chloride (344.8–351.3 mg, 2.724–2.775 mmol, 1 equiv) with methanol to a total volume of 10.0 mL. Separate stock solutions of **23** (50.0–55.0 mg, 0.135–0.148 mmol, 0.05 equiv) and EuCl_3 (33.8–35.2 mg, 0.131–0.136 mmol, 0.05 equiv) were prepared by dissolving the respective

solid in methanol and diluting to 10.0 mL. The 5% loading reactions received 1.00 mL of each stock solution; the 1% loading reactions received 1.00 mL of the benzyl chloride stock solution, 0.20 mL of the EuCl_3 and **23** stock solutions, and 1.60 mL of methanol; and the 0.5% loading reactions received 1.00 mL of the benzyl chloride stock solution, 0.10 mL of the EuCl_3 and **23** stock solutions, and 1.80 mL of methanol. Reactions were prepared in 20 mL vials containing approximately 176 mg of zinc dust (~10 equiv vs substrate) and a Teflon-coated stir bar, then sealed with electrical tape prior to removal from the glovebox. Reactions were stirred for two hours in the dark prior to being illuminated by blue LEDs for six hours. After completion, each reaction mixture was removed from the photoreactor, filtered through Celite to remove zinc, and diluted to 100.0 mL in ACS-grade methanol for analysis by GC–MS using method A (see GC–MS section 2.4.2 below).

Control reactions were prepared in a dry glovebox under an atmosphere of N_2 . The control reaction omitting light was prepared as described in the stoichiometric reaction section above, but the reaction vessel was wrapped in foil inside the photoreactor and stirred for 30 min. For the control reaction omitting europium, solid **23** (11.1 mg, .0300 mmol, 1 equiv) was weighed into a 20 mL vial with a Teflon-coated stir bar along with a solution of benzyl chloride (27 mM, 1.00 mL) and methanol (2.00 mL), and the reaction was stirred under irradiation from blue LEDs for 30 min. For the control reaction omitting **23**, solid EuCl_2 (14.4 mg, .0646 mmol, 2 equiv) was weighed into a 20 mL vial with a Teflon-coated stir bar along with a solution of benzyl chloride (27 mM, 1.00 mL) and methanol (2.00 mL), and the reaction was stirred under irradiation from blue LEDs for 30 min. All control reactions were sealed with electrical tape before being removed from inert atmosphere. After completion, each reaction mixture was

removed from the photoreactor and diluted to 10.0 mL in ACS-grade methanol for analysis by GC–MS using method A (see GC–MS section 2.4.2 below).

For the control reaction showing that zinc alone does not promote the coupling of benzyl chloride, zinc dust (~176 mg, 10 equiv) was weighed into a 20 mL vial with a Teflon-coated stir bar. To this vial was added a solution of benzyl chloride (114 mM, 3.00 mL). For the control showing the reaction of benzyl chloride with light, benzyl chloride (35.9–36.1 mg, 0.2863–0.285 mmol) was weighed into a vial containing methanol (3.00 mL). The reactions were stirred for two hours in the dark before being exposed to blue LEDs for six hours. All control reactions were sealed with electrical tape before being removed from the glovebox. After completion, each reaction mixture was removed from the photoreactor and diluted to 100.0 mL with ACS-grade methanol for analysis by GC–MS using method A (see GC–MS section 2.4.2 below). The reactions containing zinc were filtered through Celite to remove the zinc prior to dilution.

2.4.2 Gas Chromatography–Mass Spectrometry

Gas chromatography–mass spectrometry (GC–MS) analyses (**Figures A2.9–A2.17**) were performed on a Shimadzu GC 2010 Plus gas chromatograph with a Shimadzu SH-Rxi-5Sil MS 30 m column and Shimadzu GCMS-QP2010 SE mass spectrometer with an electron impact ionization source. All GC methods used an injection temperature of 250 °C and split injection mode with a 5.0 split ratio. All MS methods used an ion source temperature of 200 °C, an interface temperature of 300 °C, an event time of 0.10 s, and a scan speed of 20,000 amu s⁻¹. Three separate methods (A, B, and C) were prepared to analyze the reactions and their specifications are listed below:

- A. The temperature gradient for the GC method for the benzyl chloride coupling reaction starts at 50 °C and holds for 2.5 min, ramps to 300 °C at 50 °C per min, and holds at 300

°C for 1 min. MS acquisition time was set from 2.5 to 8.5 min. Calibration solutions for the starting materials [benzyl chloride (2.394–0.5984 mM)] and potential products [toluene (0.4027–0.1007 mM); 1,2-diphenylethane (1.569–0.3923 mM)] for the benzyl chloride reactions were prepared from commercially available materials in ACS-grade methanol. Integrated peak areas from the chromatograms were used to prepare standard curves and calculate yields of reactions.

- B. The temperature for the GC method for the allyl chloride and 2-chloro-2-methylpropane coupling reactions holds at 26 °C for 6 min. MS acquisition time was set from 1.95 to 6 minutes. Calibration solutions for the starting materials [2-chloro-2-methylpropane (1.997–0.09987 mM)] and potential products [1,5-hexadiene (1.0229–0.05115 mM); 2,2,3,3-tetramethylbutane (1.0225–0.05113 mM)] of the allyl chloride and 2-chloro-2-methylpropane reactions were prepared in GC–MS-grade *n*-pentane. Allyl chloride did not yield a linear GC–MS response vs concentration, so its calibration curve was not utilized. Integrated peak areas from the chromatograms were used to prepare standard curves and calculate yields of reactions.
- C. The temperature gradient for the GC method for the chlorobenzene coupling reaction starts at 30 °C and holds for 5.5 min, ramps to 250 °C at 80 °C per min, and holds at 250 °C for 2 min. MS acquisition time was set from 2.05 to 8.69 min. Calibration solutions for the starting materials [chlorobenzene (2.213–0.1107 mM)] and potential products [benzene (1.061–0.05307 mM); biphenyl (1.010–0.05049 mM)] of the chlorobenzene reactions were prepared in GC–MS-grade *n*-pentane. Integrated peak areas from the chromatograms were used to prepare standard curves and calculate yields of reactions.

2.4.3 Cyclic Voltammetry

Cyclic voltammetry (CV) was performed on a Pine Wavenow USB potentiostat under an atmosphere of N₂ with a glassy carbon working electrode, a platinum wire counter electrode, and a Ag/AgCl reference electrode. For the CV of Eu^{II}**23** (**Figure A2.18**), a solution of Eu(OTf)₃ (4.97 mM), **23** (28.7 mM), and tetraethylammonium perchlorate (48.1 mM) in anhydrous *N,N*-dimethylformamide (DMF) was used for the analysis, and the potential was found to be -0.90 V. Acquisition parameters were eight segments, an initial potential of -1.5 V (rising), an upper potential of 0 V, a lower potential of -1.5 V, and a sweep rate of 100 mV s⁻¹. For the CVs of the substrates (**Figure A2.19**), solutions of the substrates (90 mM) were prepared in anhydrous DMF with tetraethylammonium perchlorate (5 equiv) as the supporting electrolyte. Each acquisition consisted of eight scans with a sweep rate of 100 mV s⁻¹. Acquisition parameters and cathodic potentials for each substrate are as follows:

1. Benzyl chloride: The cathodic potential was found to be -2.34 V. Acquisition parameters were an initial potential of -2.75 V (rising), an upper potential of 0 V, and a lower potential of -2.75 V.
2. Allyl chloride: The cathodic potential was found to be -2.35 V. Acquisition parameters were an initial potential of -2.75 V (rising), an upper potential of 0 V, and a lower potential of -2.75 V.
3. Chlorobenzene: The cathodic potential was found to be -2.93 V. Acquisition parameters were an initial potential of -3.25 V (rising), an upper potential of 0 V, and a lower potential of -3.25 V.

4. 2-chloro-2-methylpropane: The cathodic potential was found to be -3.05 V. Acquisition parameters were an initial potential of -3.25 V (rising), an upper potential of 0 V, and a lower potential of -3.25 V.

CHAPTER 3: PHOTOPHYSICAL CHARACTERIZATION OF A HIGHLY LUMINESCENT DIVALENT-EUROPIUM-CONTAINING AZACRYPTATE

Parts of this chapter were reproduced or adapted with permission from: Jenks, T. C.; Bailey, M. D.; Corbin, B. A.; Kuda-Wedagedara, A. N. W.; Martin, P. D.; Schlegel, H. B.; Rabuffetti, F. A.; Allen, M. J. “Photophysical characterization of a highly luminescent divalent-europium-containing azacryptate” *Chem. Commun.* **2018**, *54*, 4545–4548. – Reproduced by permission of The Royal Society of Chemistry.

In this chapter, “we” and other first-person plural pronouns are used in reference to all authors of this publication. My individual contributions to the research include synthesis, crystal growth, and spectroscopic characterization of Eu^{2+} . Figures and tables containing data contributed by researchers other than me will contain a disclaimer in the caption; figures and tables with no disclaimer in the caption contain data collected by me. The materials and methods section represents my individual contributions to the publication.

3.1 Introduction

Luminescent materials and complexes have numerous applications in displays,^{110–114} lighting,^{115–119} imaging,^{120–122} sensing,^{123–129} and catalysis.^{13,78,130–134} Two of the most desirable traits for luminescent materials are tunability and high quantum efficiency. Recently, a highly efficient Eu^{II} -containing complex, $\text{Eu}^{2+}\text{Cl}_2$ (**Figure 3.1**), was reported that displayed yellow luminescence that is bathochromically shifted from typical Eu^{II} -based excitations and emissions.¹⁵ These large shifts prompted us to explore the ligand-induced tunability of emission for Eu^{II} . Here, we report a new Eu^{II} -containing complex that advances the understanding of the effect of ligand design on the enhancement and tunability of Eu^{II} luminescence in solution.

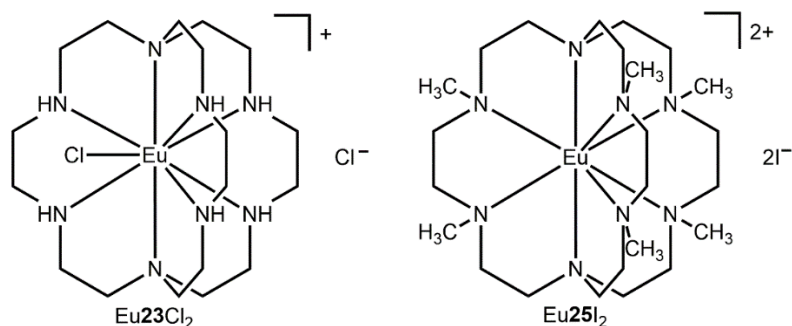


Figure 3.1 Structures of (left) Eu23Cl_2 and (right) Eu25I_2 .

3.2 Results and Discussion

Our design was based on experimental and computational studies that demonstrated that an increased splitting of 5d-orbital energies results in decreased f–d transition energies.^{7,15} The influence of a strong-field ligand on f–d transitions was demonstrated by the bathochromic shift observed with Eu23Cl_2 relative to a Eu^{II} -containing [2.2.2]-cryptate.^{4,15} We hypothesized that conversion of the secondary amine donors of Eu23Cl_2 to tertiary amines would increase the ligand field splitting of the 5d orbitals, inducing a smaller f–d transition energy and a further red-shifted emission.

The conversion of secondary amines on ligand **23** to the tertiary amines of ligand **25** was accomplished following a reported procedure that used an Eschweiler–Clarke reaction to functionalize the secondary amines with methyl groups.¹³⁵ Hexamethylated ligand **25** was metalated by mixing solutions of EuI_2 and **25** in tetrahydrofuran, resulting in the precipitation of Eu25I_2 . Complex Eu25I_2 is soluble and luminescent in degassed water, but attempts at crystallization from water were unsuccessful. However, vapor diffusion of tetrahydrofuran into a concentrated methanolic solution of Eu25I_2 yielded yellow crystals that were suitable for X-ray diffraction.

X-ray crystallography was performed to explore the geometry of Eu25I_2 , revealing a unit cell containing four units of $[\text{Eu25}]^{2+}$, eight outer-sphere iodide ions, and four disordered outer-

sphere molecules of methanol (**Figure 3.2**). The europium ion is coordinated by each tertiary nitrogen atom of the ligand in a distorted bicapped trigonal antiprism, and Eu–N bond lengths range between 2.822 Å and 2.975 Å, which are within the expected range for divalent europium with tertiary amines.^{13,15,33,35,102,136–139} When viewing the complex along the C_3 axis (**Figure 3.2**, right), the three anterior methyl groups are oriented in the opposite direction as the three posterior methyl groups. As a result of this orientation, two methyl groups from adjacent arms are situated in front of the Eu^{II} ion between each pair of arms of the cryptate. These methyl groups sterically block the sites at which anions or solvent molecules coordinate to Eu^{II} in other cryptates.^{15,33,35,138,139} Unlike Eu23Cl_2 that contains one inner-sphere chloride, Eu25I_2 has no inner-sphere anions or solvent molecules, likely due to the alignment of the methyl groups. However, because of the difference in anions between Eu23Cl_2 and Eu25I_2 , we could not rule out the possibility that the larger iodide anion precluded coordination instead of the methyl groups.

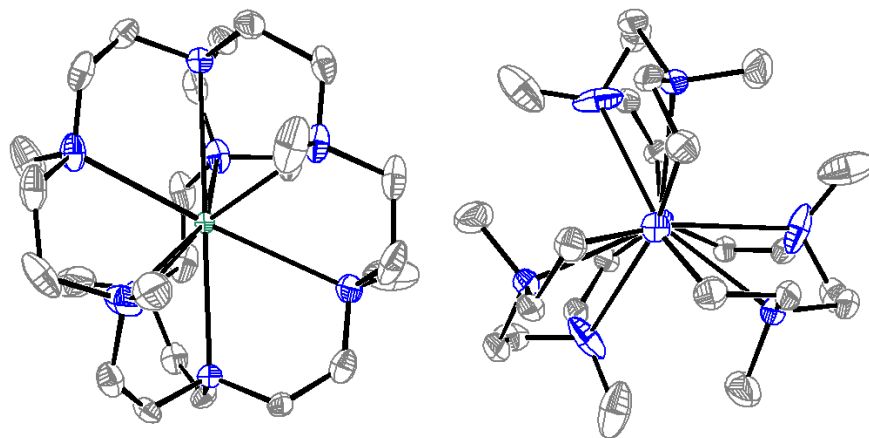


Figure 3.2 Crystal structure of Eu25I_2 oriented (left) perpendicular to and (right) along the C_3 axis. Hydrogen atoms, two outer-sphere iodide ions, and one molecule of methanol are omitted for clarity. Thermal ellipsoids are drawn at 50% probability. Crystallographic data for this structure are available at the Cambridge Crystallographic Data Centre under deposition number CCDC 1826978. Blue = nitrogen; grey = carbon; and seagreen = europium. Data collected by Matthew D. Bailey.

To study the relative influence of methyl groups and counteranions on geometry, we crystallized Eu23I_2 . The structure of Eu23I_2 revealed a similar nine-coordinate hula-hoop geometry as Eu23Cl_2 with iodide replacing chloride (**Figure 3.3**).¹⁵ The iodide structure indicates that the methyl groups, and not the size of the anion, were responsible for the change in coordination of Eu25I_2 relative to Eu23Cl_2 or Eu23I_2 . After observing the structural features of Eu25I_2 , we characterized its photophysical properties.



Figure 3.3 Crystal structure of Eu23I_2 . Hydrogen atoms and an outer-sphere iodide ion have been omitted for clarity. Thermal ellipsoids are drawn at 50% probability. Crystallographic data for this structure are available at the Cambridge Crystallographic Data Centre under deposition number CCDC 1826977. Blue = nitrogen; grey = carbon; seagreen = europium; and pink = iodine. Data collected by Philip D. Martin.

To probe the photophysical properties of Eu25I_2 , absorption, excitation, and emission spectra were collected (**Figure 3.4**). Solutions of Eu25I_2 were handled under inert atmosphere because luminescence decreased in the presence of air, likely due to oxidation of Eu^{II} to Eu^{III} . The UV–visible spectrum showed two absorbance peaks centered at 261 ($\epsilon = 752 \text{ M}^{-1} \text{ cm}^{-1}$) and 345 nm ($\epsilon = 274 \text{ M}^{-1} \text{ cm}^{-1}$). Luminescence studies revealed a broad excitation peak at 271 nm and another centered at 349 nm that trailed into the visible region, with an associated broad emission peak centered at 447 nm. These broad peaks are indicative of f–d transitions.^{4,7,9} With

the addition of the electron-donating methyl groups to the coordinating nitrogen atoms of the cryptand, we expected to see a bathochromic shift in the absorbance of Eu**25**I₂ relative to Eu**23**Cl₂. This shift was expected because an increased splitting of the d-orbitals by the stronger-field tertiary amine donors of **25** relative to the secondary amine donors of **23** should result in a lower-energy f–d transition for Eu^{II}. Instead, we observed a slight hypsochromic shift that brought the absorbance of Eu**25**I₂ to the high-energy edge of the visible region. We suspected that this shift was due to the change in geometry of Eu**25**I₂ relative to Eu**23**Cl₂ overpowering the splitting differences, similar to what would be expected when moving between octahedral and tetrahedral geometries.

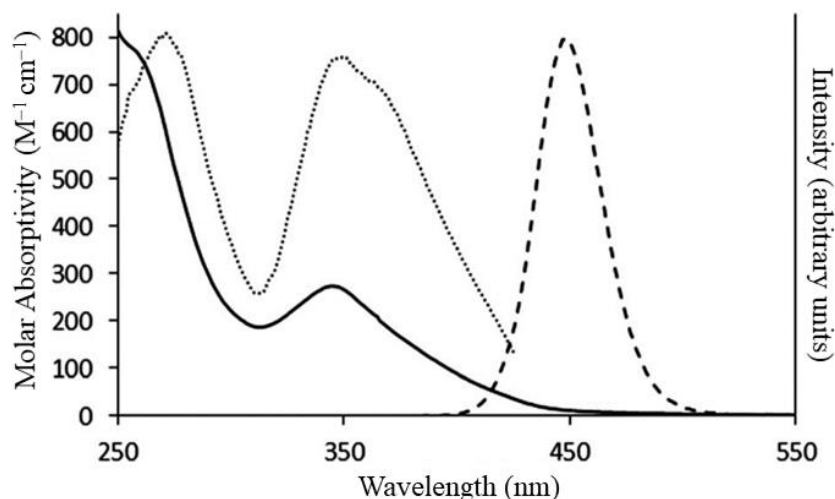


Figure 3.4 Absorption (—, left y-axis), excitation (···, right y-axis), and emission (---, right y-axis) spectra of Eu**25**I₂ (1.8 mM) in methanol.

To support our proposed explanation for the hypsochromic shift, we employed time-dependent density functional theory (TD-DFT) calculations to identify the molecular orbitals involved in the luminescence of [Eu**25**]²⁺. Prior to TD-DFT calculations, geometry-optimization calculations were performed to compare the calculated ground-state geometry in solution to the solid-state crystallographic coordinates. After optimization of [Eu**25**]²⁺ with the SMD implicit solvation model in methanol, the Eu–N bond distances from the calculation (2.893–3.145 Å)

were found to be in good agreement with crystallographic bond distances (2.822–2.975 Å).^{7,140} With the completion of the ground-state optimization, the calculation for [Eu25]²⁺ ground-state geometry was validated, and excitation and emission calculations were pursued.

TD-DFT calculations (80 states)^{7,141–145} were performed to obtain simulated excitation and emission spectra of [Eu25]²⁺. The calculated absorbance spectrum (**Figure A3.1**) displays two broad peaks centered at 268 and 357 nm that are comparable to the broad peaks in the experimental spectrum centered at 261 and 345 nm. To simulate the emissive state, we optimized the geometry corresponding to the high-oscillator-strength transition from the lower-energy absorbance curve. TD-DFT calculations of the emissive state were then employed to simulate the emission.^{141–145} The calculated emission spectrum (**Figure A3.2**) displayed a maximum value at 384 nm and is within the expected error of the experimental value (447 nm).⁷ To further understand the luminescence, natural-transition-orbital calculations were performed to characterize the high-oscillator-strength transitions involved in the two major excitations. For the high-energy excitation at 268 nm, natural-transition-orbital calculations revealed an expected 4f–5d transition, specifically from a 4f_{z³}-type orbital to a 5d_{z²}-type orbital with an oscillator strength of 0.029. For the lower-energy excitation at 357 nm, natural-transition-orbital calculations revealed a 4f–5d transition from a 4f-type orbital to a 5d_{xy}-type orbital with an oscillator strength of 0.0036. Comparison of the TD-DFT and natural-transition-orbital calculations of [Eu25]²⁺ to reported calculations of [Eu23Cl]⁺ revealed that both complexes involve similar orbital transitions for both the high and low energy excitations.⁷ Because the orbitals involved in the transitions for both [Eu23Cl]⁺ and [Eu25]²⁺ are similar, we sought to use an orbital energy diagram to compare the relative changes in orbital splitting energies. The orbital-energy diagrams for [Eu23Cl]⁺ and [Eu25]²⁺ based on these calculations (**Figure 3.5**) are consistent with

our measurements but display d-orbital splitting opposite to what would be expected based solely on the change from secondary to tertiary amines.

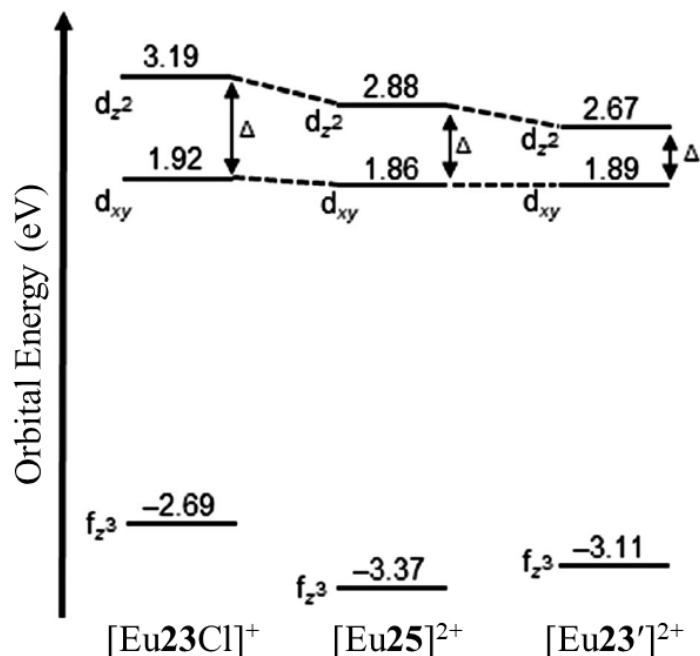


Figure 3.5 Orbital-energy diagram for the 5d_{z²}, 5d_{xy}, and 4f_{z³} orbitals for (left) [Eu23Cl]⁺,⁷ (middle) [Eu25]²⁺, and (right) [Eu23']²⁺ (where [Eu23']²⁺ is [Eu23Cl]⁺ forced into an eight-coordinate distorted bicapped antiprism, like [Eu25]²⁺). Dashed lines are visual guides. Computations performed by Brooke A. Corbin.

To better understand the impact of the different intramolecular factors contributing to the orbital energies, we developed a computational control experiment in which we forced [Eu23Cl]⁺ to adopt an eight-coordinate distorted bicapped antiprism like [Eu25]²⁺, and we calculated the excitation of the new complex, [Eu23']²⁺. Upon optimization and subsequent TD-DFT calculations, we found the orbital energies for [Eu23']²⁺ to be different from the reported values for [Eu23Cl]⁺ in two distinct ways (**Figure 3.5**). The change from nine-coordinate to eight-coordinate geometries lowered the energy of the 4f orbitals and decreased the splitting of the 5d orbital energies. Further, comparison of the calculations for [Eu25]²⁺ and [Eu23']²⁺ revealed that the d-orbital splitting supported our original hypothesis regarding expected trends based on the spectrochemical series: a smaller splitting energy was observed with the secondary-

amine donors of [Eu**23'**]²⁺ relative to the tertiary-amine donors of [Eu**25**]²⁺. From these calculations, we conclude that the cause of the observed hypsochromic shift in emission of Eu**25I**₂ relative to Eu**23Cl**₂ is dominated by the change in geometry and coordination number.

While characterizing the photophysical properties of Eu**25I**₂, we noticed that the luminescence of a solution of Eu**25I**₂ in methanol was visible to the unaided eye in ambient (laboratory fluorescent) light (**Figure 3.6**). Against a white background, the solution appeared pale yellow, but when viewed against a black background, the solution appeared blue. The color difference was rationalized with the assumption that light is reflected off a white surface but absorbed by a black surface. The reflected light is absorbed by the solution resulting in the transmission of yellow light. Without reflected light (black background), only blue luminescence is visible. The visible luminescence with ambient-light excitation led us to expect a large quantum yield for Eu**25I**₂ in methanol and prompted us to characterize the excited state by measuring the quantum yield and luminescence lifetime. Using an integrating sphere, the quantum yields of four dilute samples (roughly 0.2, 0.4, 0.6, and 1 mM) of Eu**25I**₂ in methanol were measured, giving a value of $47 \pm 3\%$. This quantum yield is among the largest of any discrete Eu^{II}-containing complex in solution, and is, to the best of our knowledge, the largest in a protic solvent. The lifetime of the excited state of Eu**25I**₂ was also measured in methanol and was found to be 1.25 μ s, which is within the expected range for Eu^{II}-containing complexes.^{9,12,13,45} Because interactions with O–H or N–H oscillators from solvent molecules or ligands cause non-radiative decay of Eu^{II} excited states,^{4,9,15} the efficient luminescence of Eu**25I**₂ in methanol is likely due to two aspects of the cryptand: the lack of N–H oscillators on the ligand and the steric shielding of the Eu^{II} ion from solvent molecules by the methyl groups. Relative to Eu**23Cl**₂, the lack of space for inner-sphere coordination and lack of ligand-based N–H

oscillators results in fewer vibrational modes that quench the excited state of Eu^{2+} via non-radiative decay.

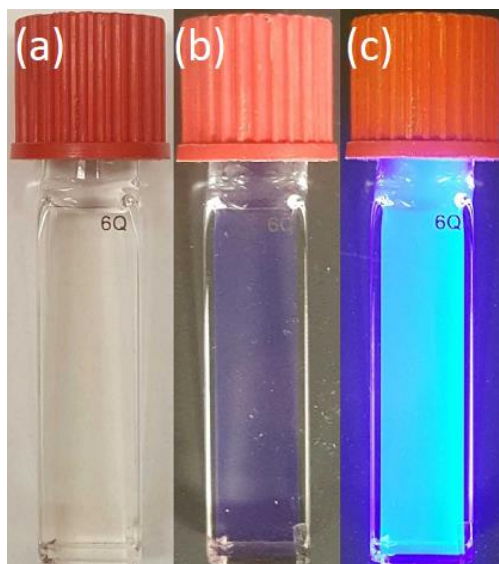


Figure 3.6 Quartz cuvette (1 cm path length) containing a solution of Eu^{2+} (1.5 mM) in methanol with (a) white and (b) black backgrounds. (c) The same cuvette under irradiation from a long-wave UV handheld lamp.

3.3 Summary

In conclusion, we have described a new Eu^{II} -containing complex that displays blue luminescence with a high quantum efficiency in protic solvent. This efficiency stems from the steric bulk of the methyl groups and lack of N–H oscillators. Crystal structures and TD-DFT calculations indicated that the blue emission is due to geometry having a larger influence on electronic transitions than d-orbital splitting from the ligand environment. This cryptate provides insight into the role of sterics and coordination environment that is expected to be useful for the rational design of divalent-lanthanide-containing complexes with desirable photophysical properties.

3.4 Materials and Methods

3.4.1 Experimental Procedures

Commercially available chemicals were of reagent-grade purity or better and were used without further purification unless otherwise noted. DriSolv anhydrous solvents were degassed under reduced pressure prior to use in the glovebox. Azacryptands 1,4,7,10,13,16,21,24-octazabicyclo[8.8.8]hexacosane (**23**)^{94,95} and 4,7,13,16,21,24-hexamethyl-1,4,7,10,13,16,21,24-octazabicyclo[8.8.8]hexacosane (**25**)¹³⁵ were prepared following published procedures.

UV-visible absorption measurements were performed using a Shimadzu UVmini-1240 spectrophotometer. Excitation and emission data were collected using a HORIBA Jobin Yvon Fluoromax-4 spectrofluorometer. Excitation and emission spectra were acquired with a 1 nm excitation slit width, 0.5 nm emission slit width, and 1 nm interval. Emission spectra were collected with an excitation wavelength of 359 nm, and excitation spectra were collected with an emission wavelength of 447 nm. The concentration of Eu for calculation of molar absorptivity was determined using energy-dispersive X-ray fluorescence (EDXF) spectroscopy at the Lumigen Instrument Center in the Department of Chemistry at Wayne State University. Elemental analyses (C, H, and N) were performed by Midwest Microlabs (Indianapolis, IN).

3.4.2 Synthesis of *Eu25I2*

In a dry glovebox under an atmosphere of N₂, a solution of **25** (131.0 mg, 0.2811 mmol) in tetrahydrofuran (8 mL) was added to a solution of EuI₂ (101.5 mg, 0.2501 mmol) in tetrahydrofuran (8 mL), and a pale-yellow precipitate immediately formed. The precipitate was washed with tetrahydrofuran (3 × 9 mL) and dried under reduced pressure to yield 211 mg (98%) of a pale-yellow solid. Anal. Calcd for C₂₄H₅₄N₈EuI₂: C, 33.50; H 6.33; N, 13.02. Found: C,

33.77; H 6.13; N, 12.71. All values are given as percentages. Crystals for X-ray analysis were grown by vapor diffusion of tetrahydrofuran into a solution of Eu_2I_2 in methanol.

CHAPTER 4: SPECTROSCOPIC AND ELECTROCHEMICAL TRENDS IN DIVALENT LANTHANIDES THROUGH THE MODULATION OF COORDINATION ENVIRONMENT

Reprinted (adapted) with permission from Jenks, T. C.; Kuda-Wedagedara, A. N. W.; Bailey, M. D.; Ward, C. L.; Allen, M. J. “Spectroscopic and Electrochemical Trends in Divalent Lanthanides through Modulation of Coordination Environment” *Inorg. Chem.* **2020**, *59*, 2613–2620. Copyright 2020 American Chemical Society.

In this chapter, “we” and other first-person plural pronouns are used in reference to all authors of this publication. My individual contributions to the research include synthesis; crystal growth; and all uncited spectroscopic and electrochemical characterization of the Yb^{II}- and Eu^{II}-containing complexes herein. Figures and tables containing data contributed by researchers other than me will contain a disclaimer in the caption; figures and tables with no disclaimer in the caption contain data collected by me. The materials and methods section represents my individual contributions to the publication.

4.1 Introduction

Advances in the fields of luminescent materials, chemical reductants, catalysis, and imaging require new materials with unique photophysical, redox, and magnetic properties. One class of molecules with properties suited for those fields is divalent-lanthanide-containing complexes.^{82,88,89,104,136,146–162} It is critical to be able to tune the properties of Ln^{II} ions, and studies of the photophysical properties of molecular complexes require a series of related ligands with systematically varied electronic and steric characteristics. Due to the relatively unexplored nature of molecular divalent-lanthanide-containing complexes compared to their trivalent counterparts, the translatability of these studies across the lanthanide series is not currently generalizable. Among Ln^{II}-containing complexes, there is a rich body of knowledge of the

photochemical, magnetic, and redox properties of Eu^{II} -containing cryptates relevant to applications including chemical reductions,^{12,163–165} luminescent materials,^{15,30,36,166,167} photoredox catalysis,^{11,13,168–170} and magnetic resonance imaging.^{138,171–176} After Eu^{II} , Yb^{II} is the Ln^{II} ion with the most positive electrochemical potential, and Yb^{II} is smaller in ionic radius than Eu^{II} by $\sim 0.1 \text{ \AA}$.¹⁷⁷ Because Yb^{II} can be coordinated by 2.2.2-cryptand (**17**) (**Figure 4.1**),^{139,178} we hypothesized that Yb^{II} could be complexed with a variety of cryptands to investigate if the influence of ligand properties on Eu^{II} is translatable across the series of divalent lanthanides, specifically to Yb^{II} . Here, we characterize a series of structurally varied Yb^{II} -containing cryptates; describe how the ligand environment influences their structural, electronic, and redox properties; and compare our findings with reported trends for Eu^{II} .

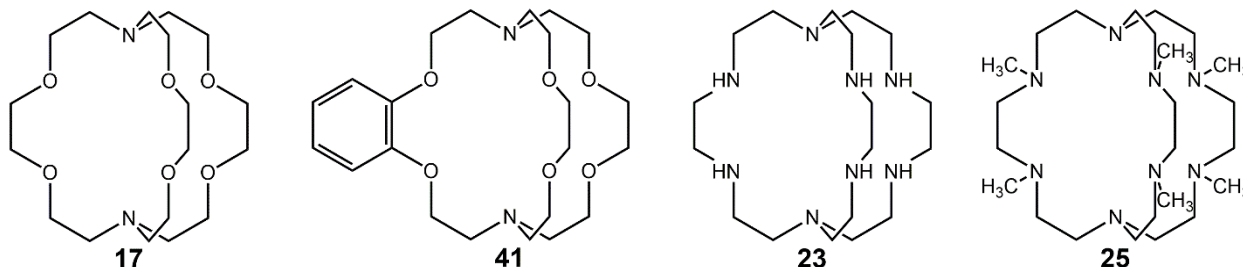


Figure 4.1 Series of cryptands, **17**, **41**, **23**, and **25**, displaying variations in donor atom identity, electronic character, and steric bulk.

To study the influence of ligand structure on the physicochemical properties of Yb^{II} -containing complexes, we used a series of four cryptands with different coordinating atoms (N or O) and functionalized scaffolds, providing systematic variations in electronic and steric character. These variations enable comparisons to previously reported Eu^{II} -containing analogues.^{7,13,15,33,36,179} This comparison is important because of the size difference between Eu^{II} (intermediate in size among the lanthanides) and Yb^{II} (one of the smallest lanthanides); therefore, the comparison of these two ions will direct future studies of Ln^{II} ions of intermediate size.

4.2 Results and Discussion

4.2.1 Solid-State Characterization

To explore the structural properties of Yb^{II}-containing cryptates, crystal structures of complexes Yb^{II}**17**, Yb^{II}**41**, Yb^{II}**23**, and Yb^{II}**25** were obtained (**Figure 4.2**). A coordinated iodide was observed with Yb^{II}**17** and Yb^{II}**41** but not with Yb^{II}**23** or Yb^{II}**25**. With the inclusion of the coordinated iodides, complexes Yb^{II}**17** and Yb^{II}**41** adopt nine-coordinate eclipsed hula-hoop geometries. This geometry for Yb^{II}**17** is the same as for a complex recently reported with a coordinated *N,N*-dimethylformamide molecule.¹⁷⁸ Complexes Yb^{II}**23** or Yb^{II}**25** adopt the relatively rare eight-coordinate bicapped trigonal antiprism geometry.¹⁸⁰ The edges that are highlighted in red (**Figure 4.2f**) of the bicapped trigonal antiprism of Yb^{II}**23** are equal in length (4.164 Å), and the two triangular planes are parallel to each other, indicating a perfect bicapped trigonal antiprism geometry.

We compared the structures of the Yb^{II}-containing cryptates with the structures of their Eu^{II}-containing analogues to look for similarities and differences. Complexes Yb^{II}**17** and Yb^{II}**41** share a nine-coordinate eclipsed hula-hoop geometry with the analogous Eu^{II}**17** and Eu^{II}**41**.³³ With the exception of one M–O bond on the benzo-bearing arm of Yb^{II}**41** (2.897(2) Å), the M–N and M–O bonds of Yb^{II}**17** and Yb^{II}**41** are shorter than those of the Eu^{II}-containing analogues, as expected for the smaller Yb^{II} ion. Yb^{II}**41** exhibits a lengthening of both M–O bonds on the benzo-bearing arm of the cryptand that is also observed with Eu^{II}**41** due to the decreased Lewis basicity imparted by the electron-withdrawing aromatic ring.^{33,181} A feature of Yb^{II}**41** that is not observed with Eu^{II}**41** is that one of the M–O bonds on the benzo-bearing arm is considerably longer than the other. We hypothesize that this lengthening is a result of the rigidity imposed by the benzo ring on cryptand **41** preventing the benzo-bearing arm of the cryptand

from contorting to accommodate ideal bond lengths from the coordinating atoms to the smaller Yb^{II} ion. Overall, the crystal structures of Yb^{II}**17** and Yb^{II}**41** in comparison to their Eu^{II}-containing analogues suggest that ethereal cryptands impose similar structural effects on Yb^{II}- and Eu^{II}-containing complexes.

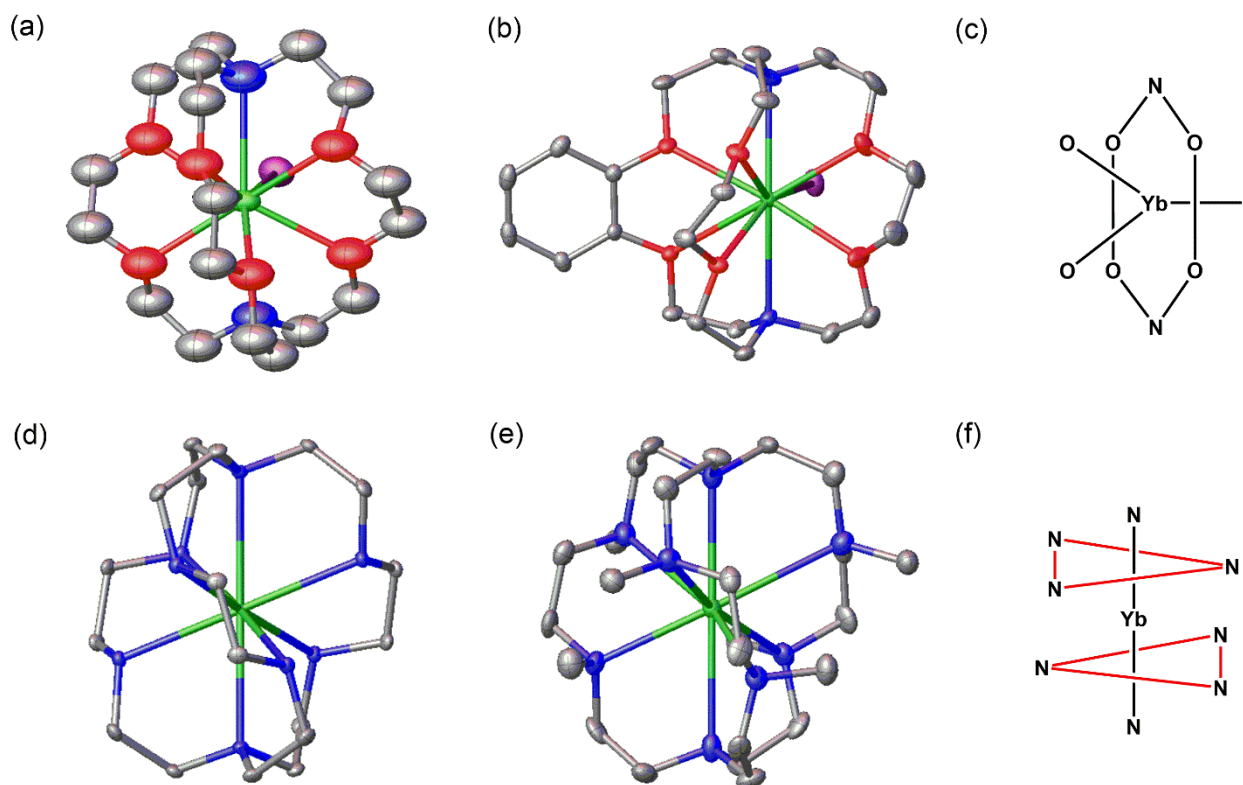


Figure 4.2 Molecular structures in crystals of (a) Yb^{II}**17** and (b) Yb^{II}**41**; (c) schematic representation of the eclipsed hula-hoop geometry of Yb^{II}**17** and Yb^{II}**41**; molecular structures in crystals of (d) Yb^{II}**23** and (e) Yb^{II}**25**; and (f) schematic representation of the bicapped trigonal antiprism geometry of Yb^{II}**23** and Yb^{II}**25**. Thermal ellipsoids are drawn at 50% probability. Hydrogen atoms, non-coordinated iodide ions, and non-coordinated solvent molecules are omitted for clarity. Blue, nitrogen; gray, carbon; red, oxygen; green, ytterbium; and purple, iodine. Crystallographic data for these structures have been deposited at the Cambridge Crystallographic Data Centre under deposition numbers CCDC 1977697–1977700. Data collected by Cassandra L. Ward and Matthew D. Bailey.

Azacryptates Yb^{II}**23** and Yb^{II}**25** adopt the same eight-coordinate bicapped trigonal antiprism geometry as Eu^{II}**25**.³⁶ Interestingly, Eu^{II}**23** adopts a nine-coordinate eclipsed hula-hoop geometry with iodide counteranions, making Yb^{II}**23** the only Yb^{II}-containing complex in this study that deviates from its Eu^{II}-containing analogue in coordination number and geometry.³⁶

The smaller coordination number of Yb^{II}**23** is likely due to the smaller ionic radius of Yb^{II} relative to that of Eu^{II}.¹⁷⁷ In some cases, as observed with Eu^{II}**23** with a zinc tetrachloride anion and Yb^{II}**17** with the [Cp'₃Yb]⁻ anion, a larger counteranion can preclude inner-sphere binding to the Ln^{II} ion, decreasing the coordination number of the complex.^{13,139} Overall, the M–N bond lengths of Yb^{II}**23** are shorter than those of its Eu^{II}-containing analogue, which is expected for the smaller Yb^{II} ion. The Yb–N bond lengths in cryptate Yb^{II}**25** vary extensively, ranging from 2.687(7) to 3.010(8) Å. Three of the six bonds between Yb^{II} and the amines on the arms of **25** measure 2.687(7) Å in length, with the other three being 3.010(8) Å. These discrepancies in bond lengths demonstrate that the Yb^{II} ion favors one side of cryptand **25** in the solid state, which could be the result of two factors, both of which are related to the smaller ionic radius of the Yb^{II} ion with respect to Eu^{II}. First, the smaller Yb^{II} ion could be coordinatively saturated by the tertiary amine donors of **25**, enabling Yb^{II} to favor one half of the cryptand. Second, the donor atoms of cryptand **25** might be unable to conform to the smaller ionic radius of Yb^{II} due to the steric bulk of the methyl groups, preventing tight packing around the ion. Overall, this data suggests that ethereal cryptands have similar structural effects on Yb^{II} and Eu^{II}, but the difference in solid-state structure between Yb^{II}**23** and Eu^{II}**23** suggests that nitrogenous cryptands promote a lower coordination number for smaller divalent lanthanides relative to mid- to large-sized divalent lanthanides.

4.2.2 Photophysical Characterization

To probe the photophysical properties of Yb^{II}-containing cryptates Yb^{II}**17**, Yb^{II}**41**, Yb^{II}**23**, and Yb^{II}**25**, UV–visible absorption spectra were collected (**Figure 4.3**). These spectra provide insight into the nature of coordination environments in solution including ligand-field effects and the strengths of metal–ligand interactions. Cryptates Yb^{II}**17**, Yb^{II}**41**, Yb^{II}**23**, and

Yb^{II}**25** display intense absorptions at wavelengths shorter than 300 nm and other absorptions between 300 and 550 nm that display different shifts based on the coordination environment. The low-energy absorption maxima for Yb^{II}**17**, Yb^{II}**41**, and Yb^{II}**25** (363, 364, and 369 nm, respectively) were within 5 nm of YbI₂ (368 nm) (**Table 4.1**). In the case of Yb^{II}**23**, two peaks were observed: a peak in the UV region centered at 324 nm and a lower-energy peak in the visible region centered at 487 nm. Absorptions of the Yb^{II}-containing complexes between 300 and 550 nm were assigned to transitions from a 4f¹⁴ ground state to a 4f¹³5d¹ excited state.^{30,182}

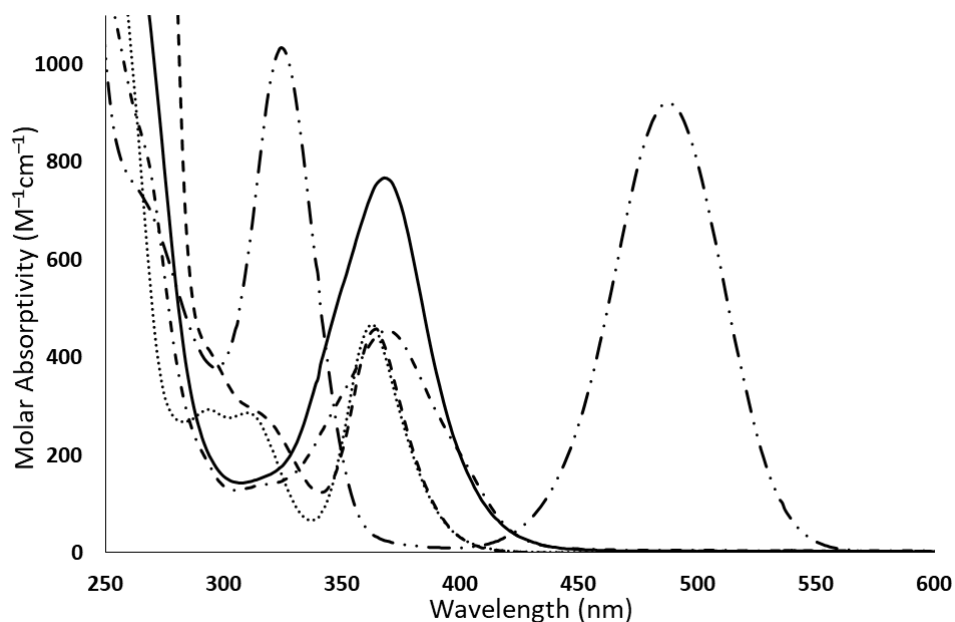


Figure 4.3 UV–visible absorption spectra of YbI₂ and Yb^{II}-containing cryptates (1 mM) in methanol: YbI₂ (—), Yb^{II}**17** (···), Yb^{II}**41** (---), Yb^{II}**23** (-·-·-), and Yb^{II}**25** (- - -).

Table 4.1 Lowest-energy absorbance maxima and corresponding extinction coefficients of Yb^{II}-containing cryptates.

Complex	λ_{abs} (nm)	ϵ (M ⁻¹ cm ⁻¹)
YbI ₂	368	543
Yb ^{II} 17	363	362
Yb ^{II} 41	364	371
Yb ^{II} 23	487	716
Yb ^{II} 25	369	476

Ether-rich cryptands **17** and **41** are expected to impose relatively weak ligand-field effects on the Yb^{II} ion. This expectation is supported by the absorption peaks of $\text{Yb}^{\text{II}}\mathbf{17}$ and $\text{Yb}^{\text{II}}\mathbf{41}$ that are clustered near the peak for YbI_2 , indicating that cryptands **17** and **41** impose relatively weak splitting on Yb^{II} . These ligands induced hypsochromic shifts of absorbance from YbI_2 as they do relative to EuI_2 ;⁷ however, the magnitude of the shifts is much larger for Eu^{II} than for Yb^{II} in the analogous complexes (**Figure 4.4**). Amine-rich cryptand **23**, which imposes a stronger ligand field than ethereal cryptands **17** and **41**, led to a lower-energy absorption than YbI_2 , consistent with its Eu^{II} -containing analogue but with a larger shift for Yb^{II} .¹⁵ Cryptand **25** imposed a smaller bathochromic shift in the absorption of Yb^{II} than cryptand **23**, which is the opposite of what is expected on the basis of orbital splitting according to the spectrochemical series, although it is consistent with the trend seen in the analogous Eu^{II} -containing cryptates.³⁶

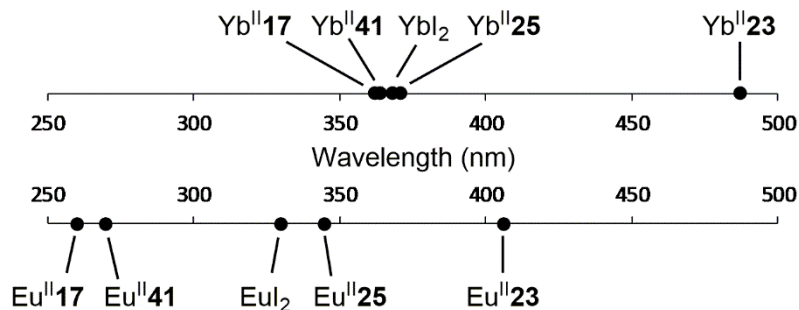


Figure 4.4 Absorption maxima of Yb^{II} -containing cryptates, Eu^{II} -containing cryptates,^{7,13,36} YbI_2 , and EuI_2 .

Overall, the absorption spectra for $\text{Yb}^{\text{II}}\mathbf{17}$, $\text{Yb}^{\text{II}}\mathbf{41}$, $\text{Yb}^{\text{II}}\mathbf{23}$, and $\text{Yb}^{\text{II}}\mathbf{25}$ display the same trends in the direction of shifts as the absorption spectra of analogous Eu^{II} -containing cryptates (**Figure 4.4**).^{7,13,36} $\text{Yb}^{\text{II}}\mathbf{17}$, $\text{Yb}^{\text{II}}\mathbf{41}$, and $\text{Yb}^{\text{II}}\mathbf{25}$ display smaller shifts from the solvated Ln^{II} ions than their Eu^{II} -containing counterparts, whereas $\text{Yb}^{\text{II}}\mathbf{23}$ displays a larger shift, indicating a strong interaction between Yb^{II} and cryptand **23**. Several factors contribute to the observed differences in absorption wavelengths between $\text{Yb}^{\text{II}}\mathbf{23}$ and the rest of the Yb^{II} -containing complexes, and

differences in coordinating atom identity and geometry alone might not explain the observed shift. With cryptand **23**, Yb^{II} displayed an absorption bathochromically shifted over 100 nm relative to that of the uncomplexed ion. The Yb^{II} ion is one of six Ln^{II} ions that are thought to display minimal metal–ligand orbital interactions;¹⁸³ however, the large shift in absorbance is highly unlikely if the interactions within the complex are purely electrostatic. Therefore, a third possible reason that governs the shift in absorption spectra is the presence of orbital interactions between the ligand and metal 5d orbitals.

To further analyze the influence of ligand structure on the electronics of these metal complexes, excitation and emission spectra were collected for YbI₂ and Yb^{II}**17**, Yb^{II}**41**, Yb^{II}**23**, and Yb^{II}**25** (**Figure 4.5**). Emission maxima for Yb^{II}**17**, Yb^{II}**41**, Yb^{II}**23**, and Yb^{II}**25** occurred in the range of 442 to 578 nm and were all shifted to lower energies relative to YbI₂ (**Figure 4.6**). Yb^{II}**17** displayed a broad emission between 380 and 540 nm ($\lambda_{\text{max}} = 467$ nm), and Yb^{II}**41** displayed a broad emission between 370 and 600 nm ($\lambda_{\text{max}} = 442$ nm) with a maximum that is shifted 25 nm higher in energy relative to Yb^{II}**17**. This shift to higher-energy emissions of Yb^{II}**41** relative to Yb^{II}**17** is a symptom of the weaker Lewis basicity of the oxygen donors attached to the benzo ring on **41**. Complex Yb^{II}**23** displayed a broad emission between 500 and 680 nm ($\lambda_{\text{max}} = 578$ nm), and Yb^{II}**25** displayed a broad emission peak between 480 and 660 nm ($\lambda_{\text{max}} = 558$ nm).

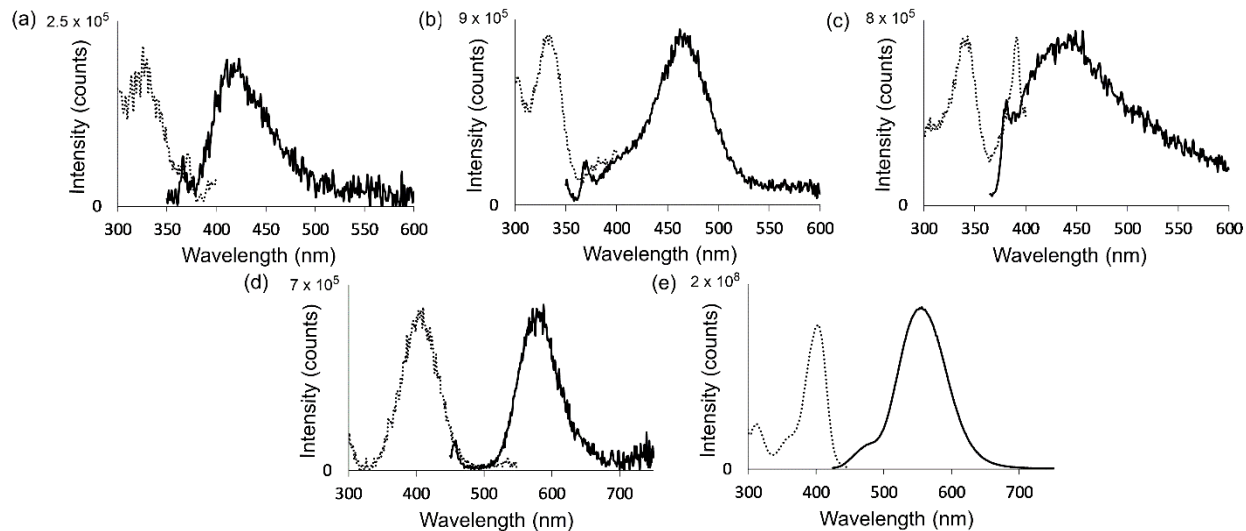


Figure 4.5 Excitation (···) and emission (—) spectra of YbI_2 and Yb^{II} -containing complexes (3 mM) in methanol: (a) YbI_2 , (b) $\text{Yb}^{\text{II}}\mathbf{17}$, (c) $\text{Yb}^{\text{II}}\mathbf{41}$, (d) $\text{Yb}^{\text{II}}\mathbf{23}$, and (e) $\text{Yb}^{\text{II}}\mathbf{25}$.

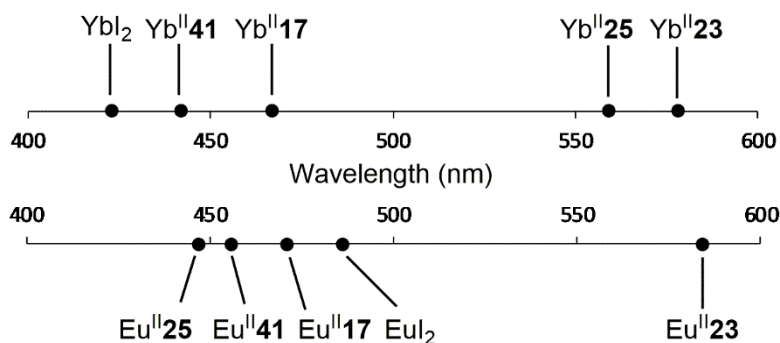


Figure 4.6 Emission maxima of Yb^{II} -containing cryptates, Eu^{II} -containing cryptates,^{7,13,36} YbI_2 , and EuI_2 .

Because emission wavelengths and intensities relate to the coordination environment of metal ions, the differences in the emission spectra of $\text{Yb}^{\text{II}}\mathbf{17}$, $\text{Yb}^{\text{II}}\mathbf{41}$, $\text{Yb}^{\text{II}}\mathbf{23}$, and $\text{Yb}^{\text{II}}\mathbf{25}$ provide insight regarding how ligand structure affects electronic character. For example, complexes $\text{Yb}^{\text{II}}\mathbf{23}$ and $\text{Yb}^{\text{II}}\mathbf{25}$ display emissions at longer wavelengths relative to $\text{Yb}^{\text{II}}\mathbf{17}$ and $\text{Yb}^{\text{II}}\mathbf{41}$ (Table 4.2). These shifts are an expected consequence of the strong-field effect of amine-rich ligands $\mathbf{23}$ and $\mathbf{25}$.¹⁵ Another difference among the emission spectra is that the emission of $\text{Yb}^{\text{II}}\mathbf{25}$ is higher intensity than those of $\text{Yb}^{\text{II}}\mathbf{17}$, $\text{Yb}^{\text{II}}\mathbf{41}$ and $\text{Yb}^{\text{II}}\mathbf{23}$ by approximately three orders of magnitude. This enhancement of emission intensity was also imparted to Eu^{II} by cryptand $\mathbf{25}$ and was

attributed to two factors: (1) the substitution of the secondary amines of **23** with the tertiary amines of **25** eliminates six N–H oscillators that are known to non-radiatively quench the excited state of Ln^{II} ions and (2) the steric bulk of the methyl groups on six of the amine donors imparts rigidity to the complex and prevents the coordination of solvent molecules that can non-radiatively quench the excited states of Ln^{II} ions.^{9,36}

Table 4.2 Excitation and emission wavelengths of YbI₂ and Yb^{II}-containing complexes.

Complex	λ_{exc} (nm)	λ_{em} (nm)
YbI ₂	328	423
Yb ^{II} 17	335	467
Yb ^{II} 41	341 and 392	442
Yb ^{II} 23	407	578
Yb ^{II} 25	404	559

When comparing the effects of cryptands **17**, **41**, **23**, and **25** on the emission of Yb^{II} and Eu^{II}, there is a departure from the similarities observed between the two ions thus far in this study (**Figure 4.6**). Cryptand **23** is the only ligand in this set to induce a bathochromic shift in emission from the solvated Eu^{II} ion, whereas all four cryptands induce a bathochromic shift in the emission of the Yb^{II} ion. This feature might lend itself useful for applications where selectively shifting the emission of the Yb^{II} ion further into the visible region is desired.

4.2.3 Electrochemical Characterization

The coordination environment influences not only the photochemical properties but also the electrochemical properties.^{52,103,153,179,184,185} Oxidation and reduction of metal complexes are associated with the energy difference between the highest occupied molecular orbitals and the lowest unoccupied molecular orbitals; therefore, a change in ligand structure that influences the energy of either of these frontier orbitals can be probed using the redox potentials of a metal

complex.¹⁸⁶ For complexes Yb^{II}**17**, Yb^{II}**41**, Yb^{II}**23**, and Yb^{II}**25**, redox potentials were measured using cyclic voltammetry, and the complexation of Yb^{II} with cryptands **17**, **41**, **23**, and **25** shifted the half-wave potentials ($E_{1/2}$) to more positive values relative to those for YbI₂ (-1.87 ± 0.01 V) (Table 4.3 and Figure 4.7). Compared to the aquated Yb^{II}/Yb^{III} couple in aqueous acid electrolytes (-1.72 V),^{187,188} the electrochemical potentials of Yb^{II}**17**, Yb^{II}**41** and Yb^{II}**23** are more positive and that of Yb^{II}**25** is more negative. Our values for cryptands **17** and **41** induced the largest positive shift of Yb^{II} relative to YbI₂, with shifts in $E_{1/2}$ of 0.72 and 0.79 V, respectively. In the case of amine-rich cryptands **23** and **25**, the half-wave potential of the corresponding complex experienced positive shifts relative to YbI₂ by 0.37 and 0.07 V, respectively.

Table 4.3 $E_{1/2}$ potentials of YbI₂ and Yb^{II}-containing complexes vs Fc/Fc⁺.

Complex	$E_{1/2}$ (V)	$E_{ox} - E_{red}$ (V)
YbI ₂	-1.87 ± 0.01	0.15
Yb ^{II} 17	-1.15 ± 0.01	0.12
Yb ^{II} 41	-1.08 ± 0.01	0.21
Yb ^{II} 23	-1.50 ± 0.01	0.12
Yb ^{II} 25	-1.80 ± 0.01	0.26

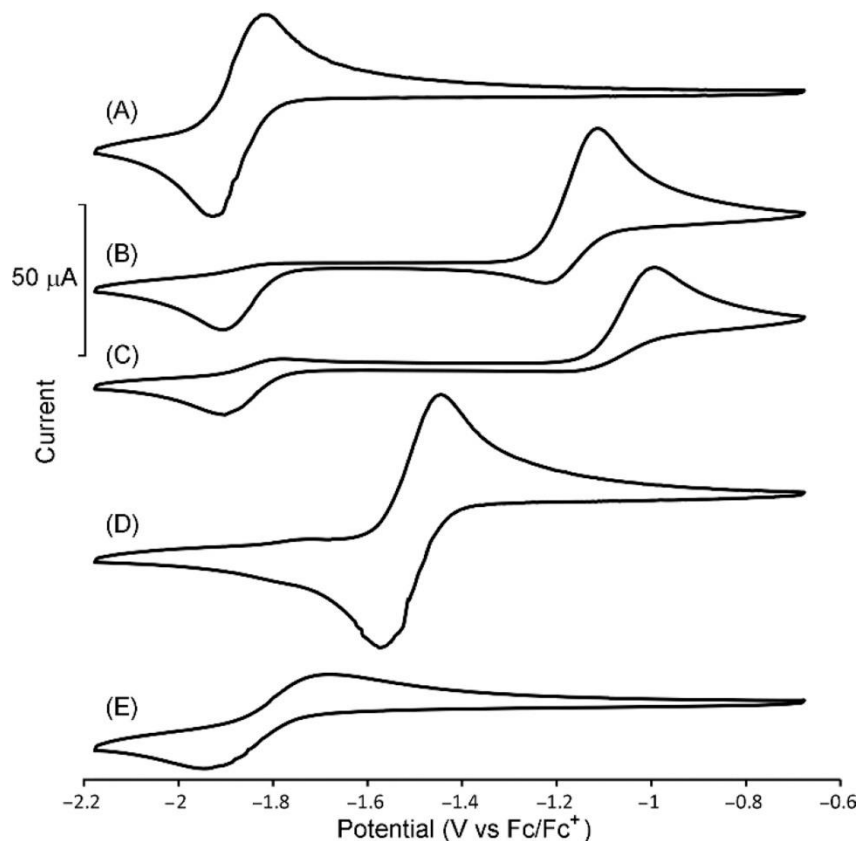


Figure 4.7 Cyclic voltammograms of (A) YbI_2 , (B) $\text{Yb}^{\text{II}}\mathbf{17}$, (C) $\text{Yb}^{\text{II}}\mathbf{41}$, (D) $\text{Yb}^{\text{II}}\mathbf{23}$, and (E) $\text{Yb}^{\text{II}}\mathbf{25}$ in *N,N*-dimethylformamide.

The cyclic voltammograms of $\text{Yb}^{\text{II}}\mathbf{17}$ and $\text{Yb}^{\text{II}}\mathbf{41}$ display large anodic peaks with small corresponding cathodic peaks at around -1.2 V and larger cathodic peaks at around -1.9 V. The $E_{1/2}$ values of $\text{Yb}^{\text{II}}\mathbf{17}$ and $\text{Yb}^{\text{II}}\mathbf{41}$ were calculated using the small cathodic peaks shifted 123 and 214 mV, respectively, more negative than the corresponding anodic peaks. The larger cathodic peaks associated with these complexes overlap with the cathodic wave of YbI_2 in solution. This observation can be explained by two possibilities: either Yb^{III} dissociates from $\mathbf{17}$ and $\mathbf{41}$ and then remetalates after the Yb^{III} ion is reduced to Yb^{II} at the electrode or after oxidation to Yb^{III} the complex undergoes a structural reorganization. Cyclic voltammetry starting from an oxidized sample of $\text{Yb}^{\text{II}}\mathbf{17}$ (**Figure A4.18**) displayed a separation of the anodic and cathodic waves similar to that from cyclic voltammetry starting from $\text{Yb}^{\text{II}}\mathbf{17}$. Additionally, scan-rate-dependent

experiments of Yb^{II}**41** (Figures A4.19–A4.22) revealed an increase in the cathodic peak area with increasing scan rate. The results of the cyclic voltammetry experiments starting from trivalent Yb and the scan-rate-dependent experiments can be employed to corroborate both the demetallation and structural reorganization theories.

Ether-rich cryptate Yb^{II}**41** displayed a more positive potential than Yb^{II}**17**, consistent with Eu^{II} and cryptands **17** and **41** (Figure 4.8).¹⁷⁹ Our $E_{1/2}$ value for Yb^{II}**17** is slightly (163 mV) more negative than a recently reported value,¹⁸⁹ which is explained by the difference in anions (Γ^- versus OTf^-) and solvents (*N,N*-dimethylformamide versus tetrahydrofuran) used in the experiments. The positive shift in $E_{1/2}$ imposed by **17** on the Yb^{II} ion is consistent across both reports. Ethereal complexes Yb^{II}**17** and Yb^{II}**41** experienced slightly smaller shifts in redox potential than their Eu^{II}-containing counterparts.

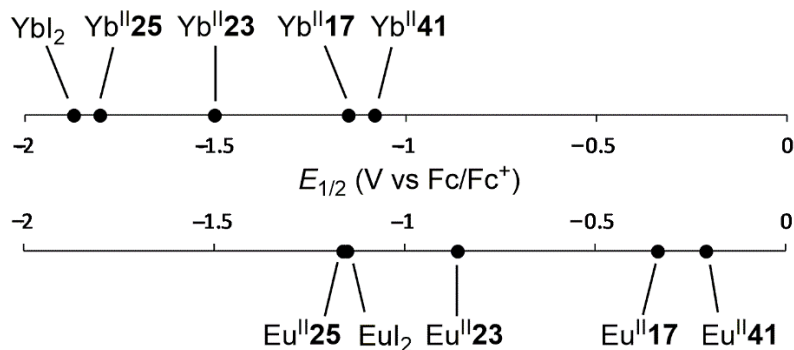


Figure 4.8 $E_{1/2}$ potentials of Yb^{II}-containing cryptates, Eu^{II}-containing cryptates,¹⁷⁹ YbI₂, and EuI₂. Values for Eu^{II}**17** and Eu^{II}**41** are for anodic peak potentials.

Complexes Yb^{II}**23** and Yb^{II}**25** displayed more negative $E_{1/2}$ values than Yb^{II}**17** and Yb^{II}**41**, which is consistent with the relationship of Eu^{II}**23** and Eu^{II}**25** with Eu^{II}**17** and Eu^{II}**41** and is due to the strong basicity of the amine-rich ligands.¹⁰¹ Cryptand **25** appeared to induce a small positive shift in redox potential for the Yb^{II} ion relative to YbI₂, but upon dissolving Yb^{II}**25** in *N,N*-dimethylformamide, we noticed that the solution appeared to be the same color as the YbI₂ solution. To probe whether Yb^{II}**25** remained complexed in *N,N*-dimethylformamide, UV–visible,

excitation, and emission spectra of Yb^{II}**25** and YbI₂ in *N,N*-dimethylformamide along with NMR spectra of Yb^{II}**25** and cryptand **25** in *N,N*-dimethylformamide and methanol were compared (Figures A4.1–A4.6 and A4.9–A4.12). The spectroscopic profiles of Yb^{II}**25** and YbI₂ in *N,N*-dimethylformamide are similar, but the NMR spectra of Yb^{II}**25** in methanol and *N,N*-dimethylformamide displayed peak broadening relative to the spectra of **25**. The NMR broadening observed for Yb^{II}**25** versus **25** paired with the change in electrochemical profile versus YbI₂ suggest that the Yb^{II} ion remains associated with cryptand **25** in solution. Overall, similar trends in the order of redox potentials of Yb^{II}**17**, Yb^{II}**41**, Yb^{II}**23**, and Yb^{II}**25** were observed relative to Eu^{II}**17**, Eu^{II}**41**, Eu^{II}**23**, and Eu^{II}**25**, with the Yb^{II}-containing cryptates having more negative potentials than the Eu^{II}-containing analogues. These results suggest that similar trends in electrochemical modulation are likely to be observed across the divalent-lanthanide series.

4.3 Summary

This study provides the basis for understanding how the properties of Ln^{II} ions in discrete molecules are affected by coordination environments by comparing complexes of Yb^{II} and Eu^{II}. The culmination of our comparative analyses has revealed coordination-induced differences in the solid-state, photophysical, and electrochemical properties between the small and mid-sized divalent lanthanides, which reaffirms the importance of ligand effects in lanthanide chemistry. This study is a critical step toward enabling the rational control of the properties of Ln^{II}-containing complexes that are potentially useful in applications including optoelectronics, photoredox catalysis, reductions, and imaging.

4.4 Materials and Methods

4.4.1 Experimental Procedures

Commercially available chemicals were used without purification unless otherwise noted. Water was purified using a PURELAB Ultra Mk2 water purification system (ELGA). 4,7,13,16,21,24-Hexaoxa-1,10-diazabicyclo[8.8.8]-hexacosane (**17**) and 5,6-benzo-4,7,13,16,21,24-hexaoxa-1,10-diazabicyclo[8.8.8]hexacos-5-ene (**41**) were purchased from Sigma-Aldrich. Ligand **41** arrived as a solution (50 wt % in toluene), and the solvent was removed under reduced pressure prior to use. 1,4,7,10,13,16,21,24-Octaazabicyclo[8.8.8]hexacosane (**23**) and 4,7,13,16,21,24-hexamethyl-1,4,7,10,13,16,21,24-octaazabicyclo- [8.8.8]hexacosane (**25**) were prepared following reported procedures.^{94,95,190} Eu^{II}**41**, Eu^{II}**23**, and Eu^{II}**25** were prepared following reported procedures.^{36,191} Commercially available anhydrous methanol, *N,N*-dimethylformamide, and tetrahydrofuran were used after degassing under reduced pressure.

UV–visible absorption spectra were collected using a Shimadzu UV mini-1240 spectrophotometer. Molar extinction coefficients were determined from the absorption spectra at different concentrations (1.0, 2.0, and 3.0 mM) of metal complexes between 250 and 600 nm. Excitation and emission spectra were recorded using a HORIBA Jobin Yvon Fluoromax-4 spectrofluorometer with 1 and 5 nm excitation and emission slit widths, respectively.

Cyclic voltammetry was performed using a Pine Wavenow USB potentiostat in an electrochemical cell under an atmosphere of Ar with a Ag/AgCl reference electrode, a glassy carbon working electrode, and a Pt wire auxiliary electrode. Acquisition parameters were eight segments, an initial potential of -1.5 V (rising), an upper potential of 0 or 1.5 V, a lower potential of -1.5 V, and a scan rate of 100 mV s⁻¹. Solutions of complexes (5 mM) and

tetraethylammonium perchlorate (0.1 M) in *N,N*-dimethylformamide were used for the analyses and were referenced to an external standard of ferrocene (1 mM). For the oxidized sample of Yb^{II}**17**, a sample of Yb^{II}**17** was exposed to compressed air to oxidize Yb^{II} to Yb^{III} until the solution changed color from a deep yellow to a pale yellow. Potentials versus ferrocene \pm the standard error of the mean of three independently prepared samples are reported.

Metal concentrations were determined using energy-dispersive X-ray fluorescence spectroscopy with a Shimadzu EDX-7000 spectrometer at the Lumigen Instrument Center in the Department of Chemistry at Wayne State University. Calibration curves were generated using fluorescence intensity at 7.22–7.62 keV for a concentration range of 25–500 ppm [diluted from the Sigma-Aldrich ICP standard, Yb₂O₃ in aqueous nitric acid (2%) 998 \pm 5 ppm]. Elemental analysis (C, H, and N) determinations were performed by Midwest Microlabs (Indianapolis, IN). All values are reported as percentages. ¹H-NMR spectra were obtained using a Mercury 400 (400 MHz) spectrometer.

4.4.2 Synthesis of Yb^{II}-Containing Complexes

Metalated complexes were synthesized and handled in an oxygen- and moisture-free glovebox under an atmosphere of N₂. Solutions of YbI₂ (0.075 mmol) in tetrahydrofuran (1.5 mL) were added to separate solutions of cryptands **17**, **41**, **23**, and **25** (0.075 mmol) in tetrahydrofuran (1.5 mL), and the resulting precipitates were washed with tetrahydrofuran (3 \times 1 mL). Residual solvent was removed under reduced pressure to yield the metal complexes. Precipitated solids (~20 mg) were used to grow crystals for X-ray analyses. Vapor diffusion of tetrahydrofuran into methanolic solutions was used to grow crystals of Yb^{II}**17** and Yb^{II}**41**. Slow evaporation from methanol/tetrahydrofuran (1:4) was used to grow crystals of Yb^{II}**23**. Vapor

diffusion of tetrahydrofuran into an acetonitrile/tetrahydrofuran (1:1) solution was used to grow crystals of Yb^{II}**25**.

Yb^{II}**17**. A white powder (50.0 mg, 83%). Anal. Calcd for C₁₈H₃₆N₂O₆YbI₂: C, 26.91; H, 4.52; N, 3.49. Found: C, 26.31; H, 4.51; N, 3.29.

Yb^{II}**41**. A white powder (45.0 mg, 70%). Anal. Calcd for C₂₂H₃₆N₂O₆YbI₂: C, 31.27; H, 4.56; N, 3.17. Found: C, 31.24; H, 4.38; N, 3.21.

Yb^{II}**23**. A red powder (51.0 mg, 85%). Anal. Calcd for C₁₈H₄₂N₈YbI₂: C, 27.51; H, 5.59; N, 13.51. Found: C, 27.88; H, 5.38; N, 13.50.

Yb^{II}**25**. A pale-yellow powder (55.5 mg, 85%). Anal. Calcd for C₂₄H₅₄N₈YbI₂: C, 32.70; H, 6.17; N, 12.71. Found: C, 32.91; H, 5.99; N, 12.42.

CHAPTER 5: SUMMARY AND FUTURE DIRECTIONS

5.1 Summary

The luminescence of complexes of divalent lanthanides in solution, and accordingly the applications thereof, is strongly dependent on the coordination environment surrounding the Ln^{II} ions. The electronics of coordinating ligands and the geometry of the resulting complexes determine both the energy and intensity of the Ln^{II} -containing complex with respect to the free ion. While the amount of research regarding trivalent-lanthanide luminescence eclipses that of divalent lanthanides, the luminescence of divalent lanthanides possesses several desirable qualities including tunability and large intensity with respect to those of trivalent lanthanides.

In Chapter 2, the application of the luminescent complex $\text{Eu}^{\text{II}}\mathbf{23}$ in photoredox catalysis is described. Under irradiation from blue light, $\text{Eu}^{\text{II}}\mathbf{23}$ enters an excited state that has a calculated electrochemical potential that is more than two volts more negative than the ground-state potential. Stoichiometric reactions run to completion in less than 30 minutes and as many as 120 turnovers were observed under catalytic conditions. A substrate scope bearing various reduction potentials suggested an electrochemical window of -0.9 to -3 V vs Ag/AgCl where temporal control of reactions can be achieved. The results of this study provide insight into an impactful application for luminescent Eu^{II} -containing complexes and laid the foundation for future studies regarding Eu^{II} -based photoredox catalysis.

In Chapter 3, a new Eu^{II} -containing complex, $\text{Eu}^{\text{II}}\mathbf{25}$, is described that displays blue luminescence with a high quantum efficiency in protic solvent. $\text{Eu}^{\text{II}}\mathbf{25}$ is a structurally modified variant of $\text{Eu}^{\text{II}}\mathbf{23}$ with methyl groups replacing the protons on the secondary amines of $\mathbf{23}$. This functionalization was expected to bathochromically shift the photophysical properties of $\text{Eu}^{\text{II}}\mathbf{25}$ with respect to $\text{Eu}^{\text{II}}\mathbf{23}$ based on the trends of the electrochemical series, but the observed

hypsochromic shift was determined to be a result of the change in geometry between the two complexes. Although the methyl groups did not induce the expected bathochromic shift, they did induce a substantial increase in luminescence quantum yield due to the retardation of nonradiative encounters between solvent molecules and the Eu^{II} ion and lack of N–H oscillators on the ligand. The results of this study provide information on the balance between geometry and electronics when designing a coordination field to tailor the photophysical properties of divalent lanthanides.

In Chapter 4, the analysis of a series of Yb^{II} -containing cryptates is described with respect to trends in the structural, spectroscopic, and electrochemical properties that are dependent on coordination environment. The trends found among the Yb^{II} -containing complexes were compared to trends among Eu^{II} -containing analogues to establish the degree of translatability of coordination motifs between divalent lanthanides. Differences between the trends found within the Yb^{II} and Eu^{II} series reaffirm that while some properties are affected similarly between Ln^{II} complexes, coordination environment does not affect all divalent lanthanides equally. The results of this study provide the basis for understanding how the properties of different Ln^{II} ions are influenced by the same coordination field and direct the rational design of future complexes of divalent lanthanides, especially those with sizes between those of europium and ytterbium.

5.2 Future Directions

In Chapter 2, $\text{Eu}^{\text{II}}\mathbf{23}$ was examined for use in photoredox catalysis. Because this was a preliminary investigation seeking to establish Eu^{II} as a viable candidate as a photoredox precatalyst, the reported reactivity consisted of a narrow scope meant to evaluate the electrochemical window within which $\text{Eu}^{\text{II}}\mathbf{23}$ could catalyze chemical reductions. An avenue by

which my research could be extrapolated is the further investigation of substrates, functional groups, solvents, and other assorted reaction conditions under which $\text{Eu}^{\text{II}}\mathbf{23}$ can promote reductive reactions. I expect that expanding the conditions and substrates that are compatible with $\text{Eu}^{\text{II}}\mathbf{23}$ will reap benefits spanning several divisions of chemistry: there will be a more fundamental understanding of the underrepresented field of molecular complexes of divalent lanthanides; and organic chemists will be given a relatively inexpensive and earth-abundant reductant that exceeds the potency of SmI_2 with hexamethylphosphoramide yet enables temporal control of reactions like $\text{Ru}(\text{bpy})_3$.

There are two major ways to augment the reactivity of a metal-based catalyst—modulating the coordination environment surrounding the metal ion and changing the identity of the metal. Chapter 4 explored the effects of both ligand modifications and metal selection on the properties relevant to photoredox catalysis. While there are nearly endless possibilities in the realm of ligand modification, it was shown in Chapter 4 that simply switching the Ln^{II} within a cryptate can have a profound influence on the electrochemical potential. For example, $\text{Eu}^{\text{II}}\mathbf{23}$ and $\text{Yb}^{\text{II}}\mathbf{23}$ have similar excitation and emission wavelengths, meaning that $\text{Yb}^{\text{II}}\mathbf{23}$ will also be excited by visible light and will have a similar enhancement of its excited-state potential versus its ground-state potential (**Equation 2.1**). However, the ground-state potential of $\text{Yb}^{\text{II}}\mathbf{23}$ is more than 0.5 V more negative than that of $\text{Eu}^{\text{II}}\mathbf{23}$, meaning that the excited-state potential of $\text{Yb}^{\text{II}}\mathbf{23}$ should be significantly more potent than the already impressive excited-state potential of $\text{Eu}^{\text{II}}\mathbf{23}$. For these reasons, I expect the investigation of the photoredox activity of $\text{Yb}^{\text{II}}\mathbf{23}$ to be a valuable extension of my graduate research.

In the preceding chapters, the fundamentals of coordination effects on the properties of divalent lanthanides was discussed with a strong emphasis on Eu^{II} and Yb^{II} , the divalent

lanthanides with the most positive electrochemical potentials. These studies could reasonably be extended to divalent lanthanides of more negative electrochemical potentials such as Sm^{II} and Tm^{II} . Not only will these studies reveal further trends in coordination effects across the divalent-lanthanide series, but because the electrochemical potentials of Sm^{II} and Tm^{II} are even more negative than those of Eu^{II} and Yb^{II} , they have the potential to be even more potent reductants than Eu^{II} **23**.

APPENDIX A: SUPPLEMENTARY FIGURES

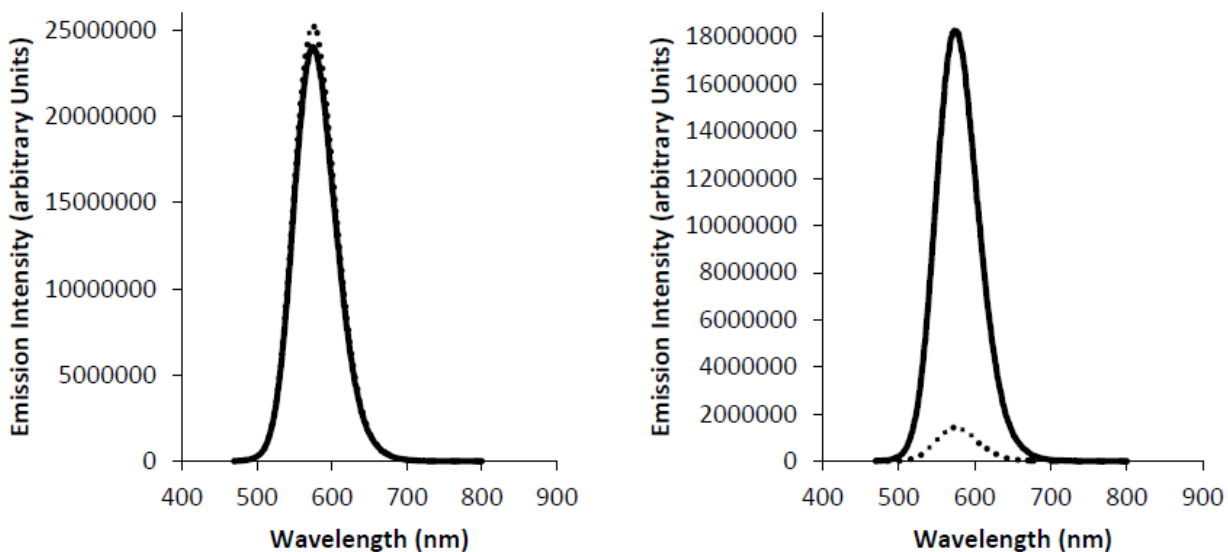


Figure A2.1 Emission of Eu^{II}23 before (—) and after (···) 12 h of either darkness (left) or exposure to blue LED light in a photoreactor (right). Data collected by Matthew D. Bailey.

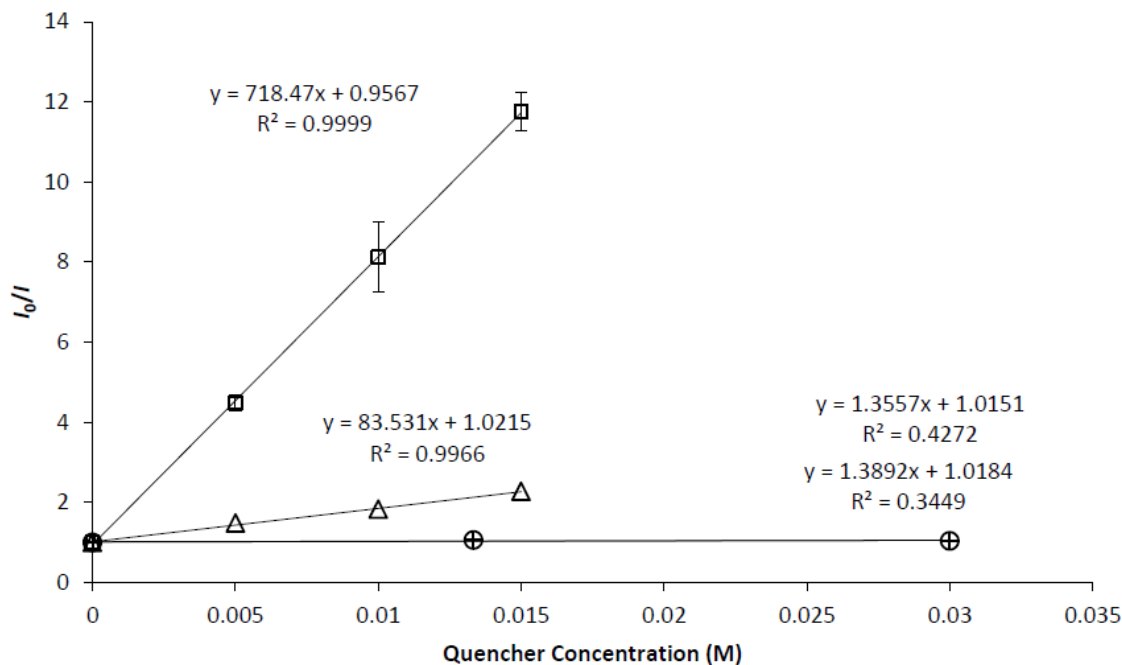


Figure A2.2 Ambient temperature Stern–Volmer analyses with benzyl chloride (squares), allyl chloride (triangles), chlorobenzene (circles), and 2-chloro-2-methylpropane (plus signs). Error bars represent the standard deviation of the mean of the measurements of independently prepared samples. Data collected by Matthew D. Bailey.

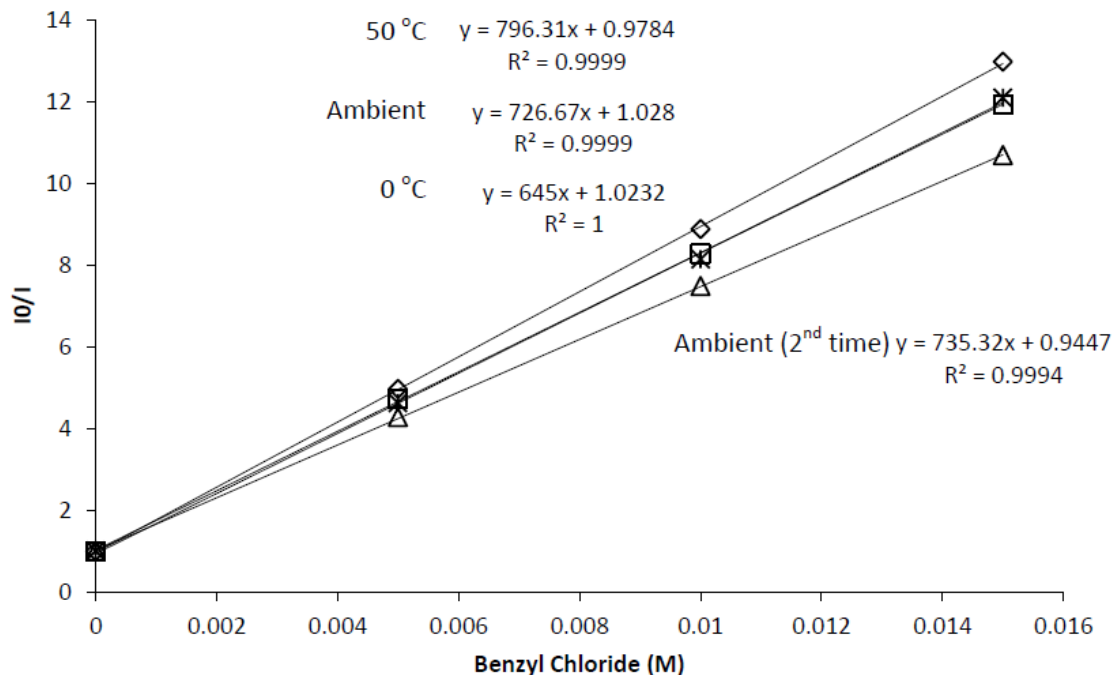


Figure A2.3 Variable temperature Stern–Volmer analysis: initial ambient-temperature measurements (squares), 50 °C measurements (diamonds), 0 °C measurements (triangles), and final ambient-temperature measurements (asterisks). Data collected by Matthew D. Bailey.

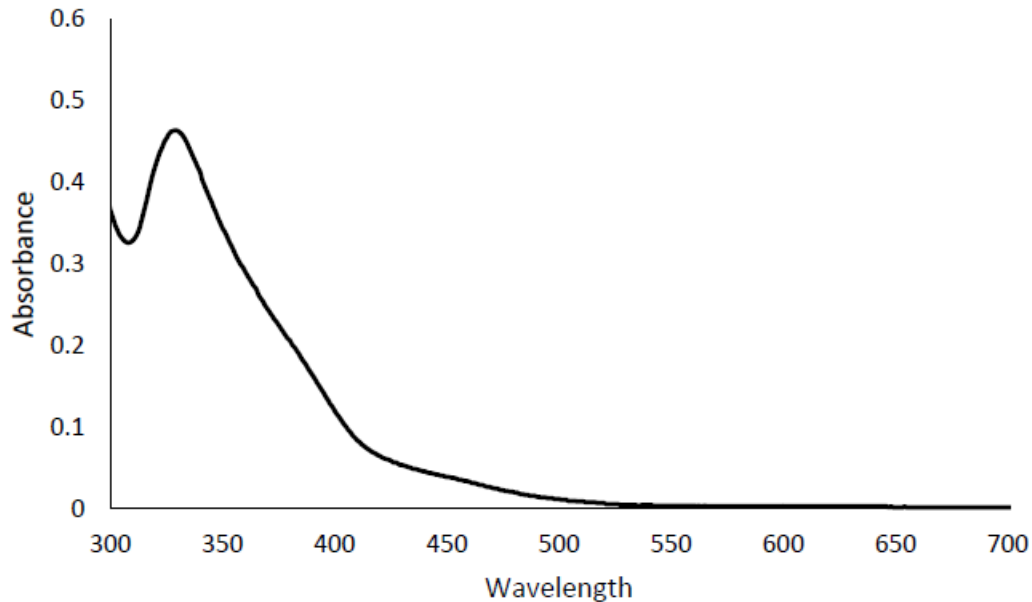


Figure A2.4 UV–visible spectrum of *in situ* generation of $\text{Eu}^{\text{II}}\mathbf{23}$. Data collected by Matthew D. Bailey.

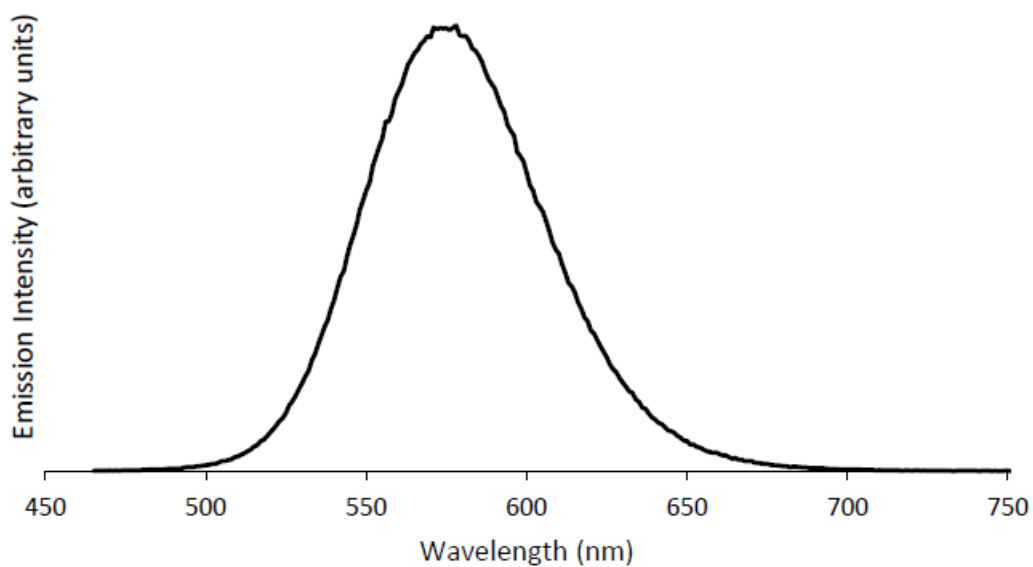


Figure A2.5 Fluorescence spectrum of *in situ* generation of $\text{Eu}^{\text{II}}\mathbf{23}$, $\lambda_{\text{ex}} = 460$ nm. Data collected by Matthew D. Bailey.

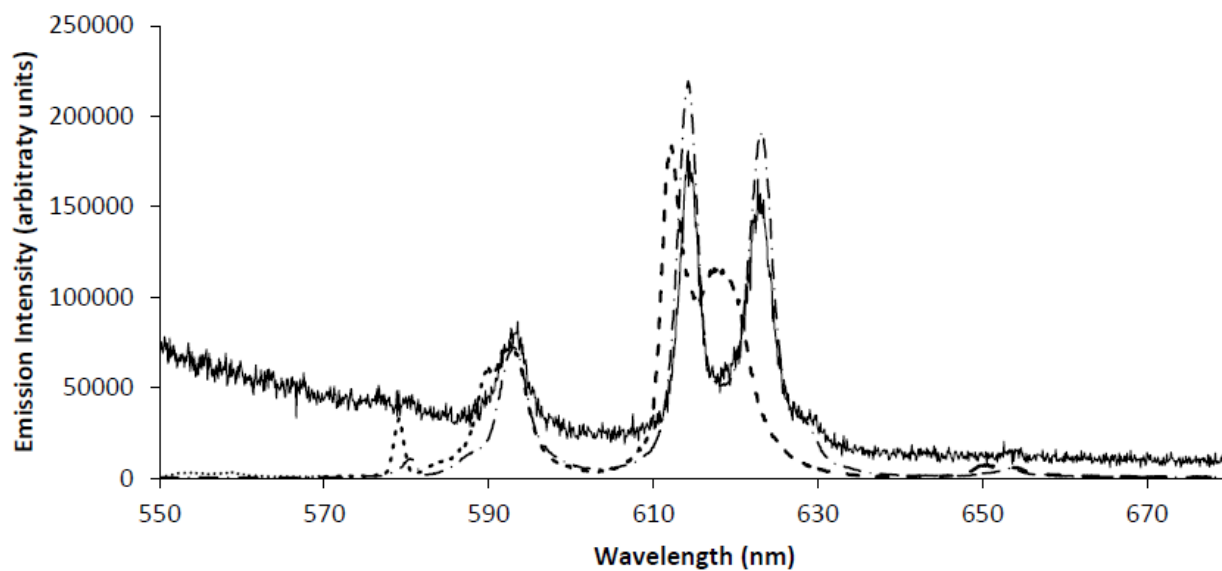


Figure A2.6 Eu^{III} binding study. EuCl_3 in methanol (10 mM, \cdots), EuCl_3 and $\mathbf{23}$ (10 mM each, $-\cdot-\cdot-$), and oxidized $\text{Eu}^{\text{II}}\mathbf{23}$ (2 mM, $—$). Data collected by Matthew D. Bailey.



Figure A2.7 Picture of a photoreactor next to a cooling fan.

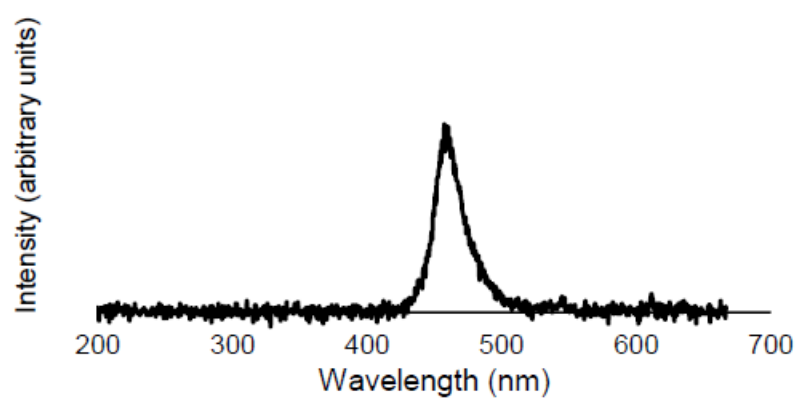


Figure A2.8 Emission profile of the blue light-emitting diodes used in the photoreactors showing a maximum emission band centered at 460 nm.

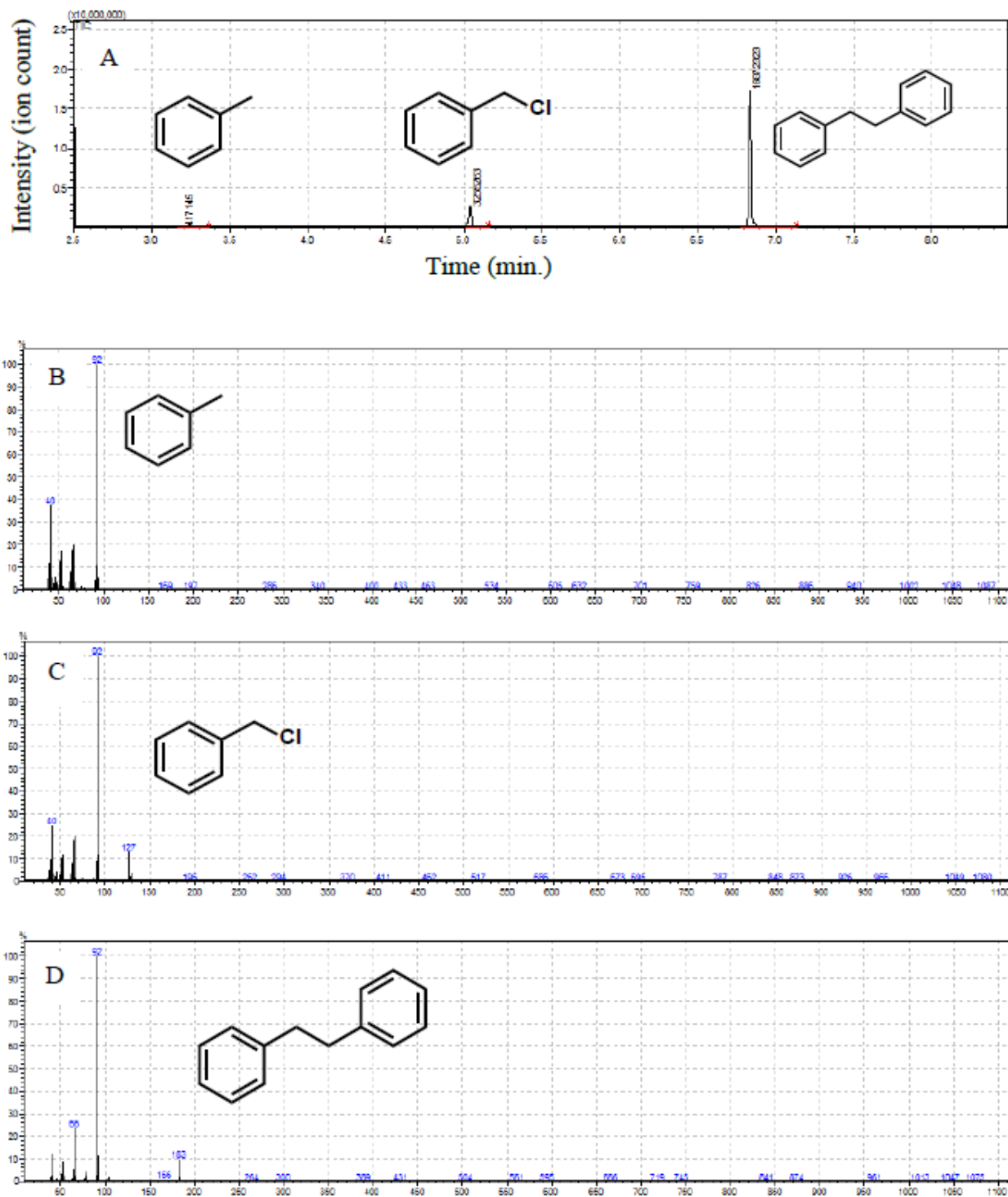


Figure A2.9 (A) Representative GC-MS chromatogram of a stoichiometric benzyl chloride coupling reaction. (B) Mass spectrum of the peak at 3.25 min corresponding to toluene. (C) Mass spectrum of the peak at 5.05 min corresponding to benzyl chloride. (D) Mass spectrum of the peak at 6.85 min corresponding to 1,2-diphenylethane.

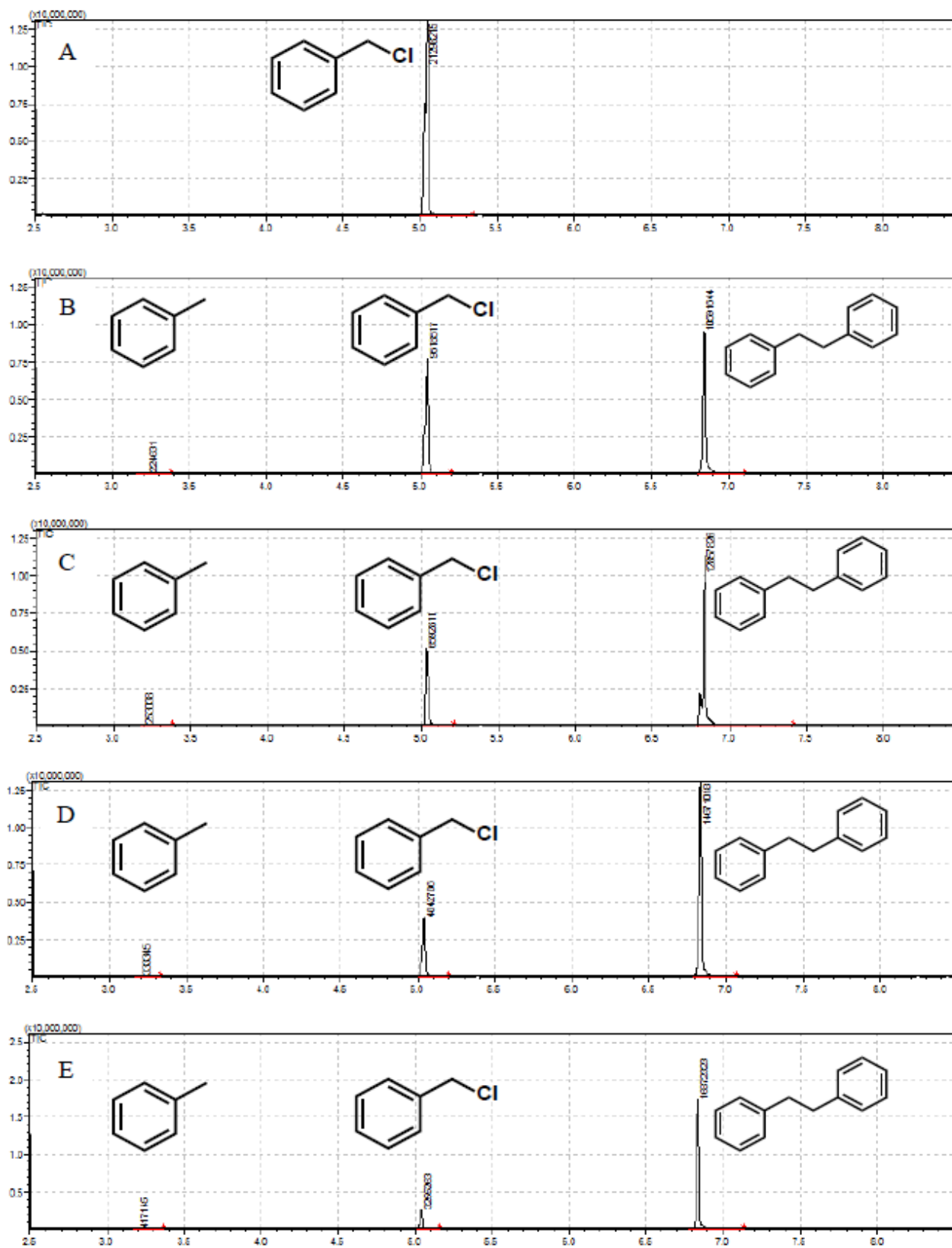


Figure A2.10 (Part 1) Full caption can be found on the following page.

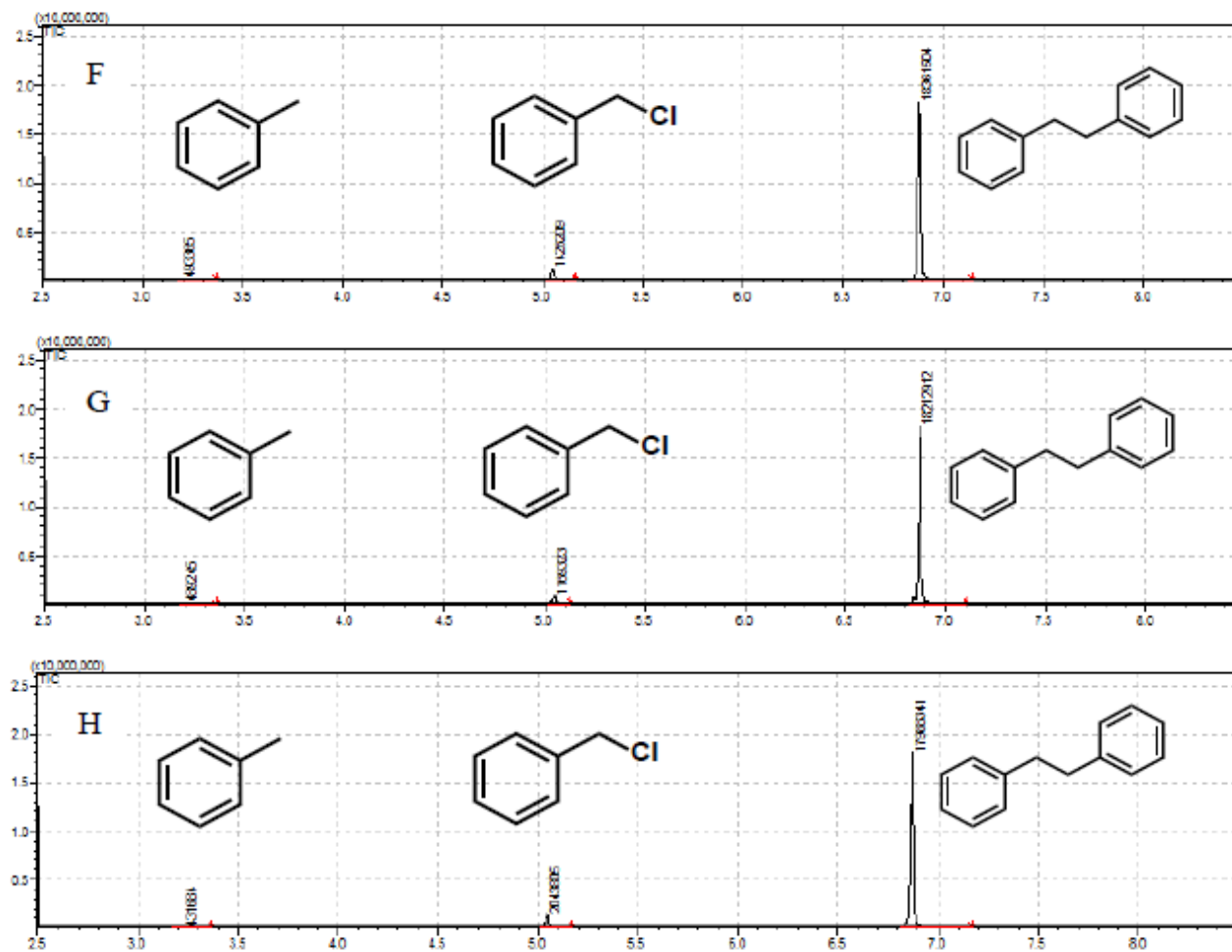


Figure A2.10 (Continued) Representative GC–MS chromatograms of a time progression of stoichiometric benzyl chloride coupling reaction. Each chromatogram is of a separate reaction stopped after (A) 0, (B) 5, (C) 10, (D) 15, (E) 20, (F) 25, (G) 30, and (H) 35 min.

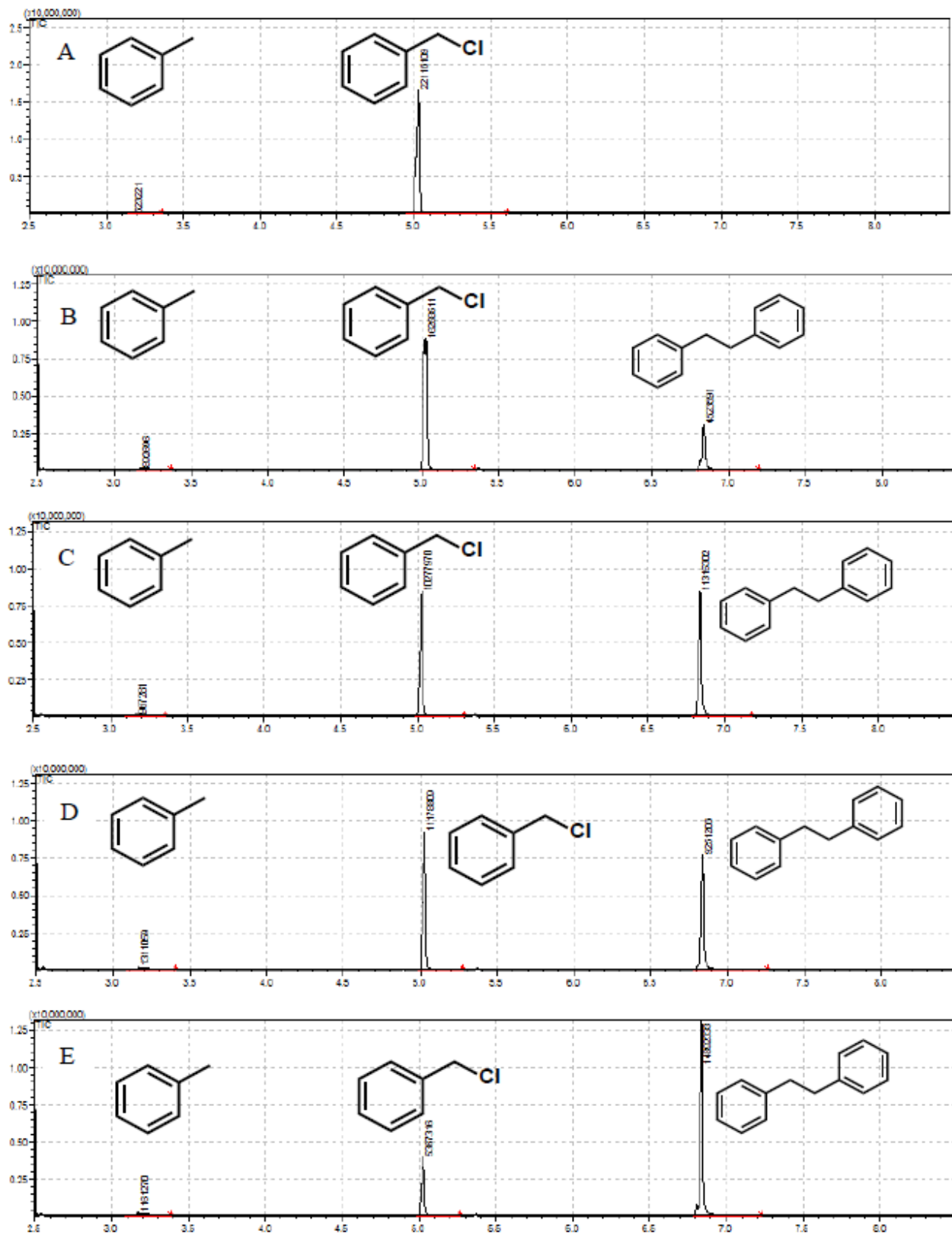


Figure A2.11 (Part 1) Full caption can be found on the following page.

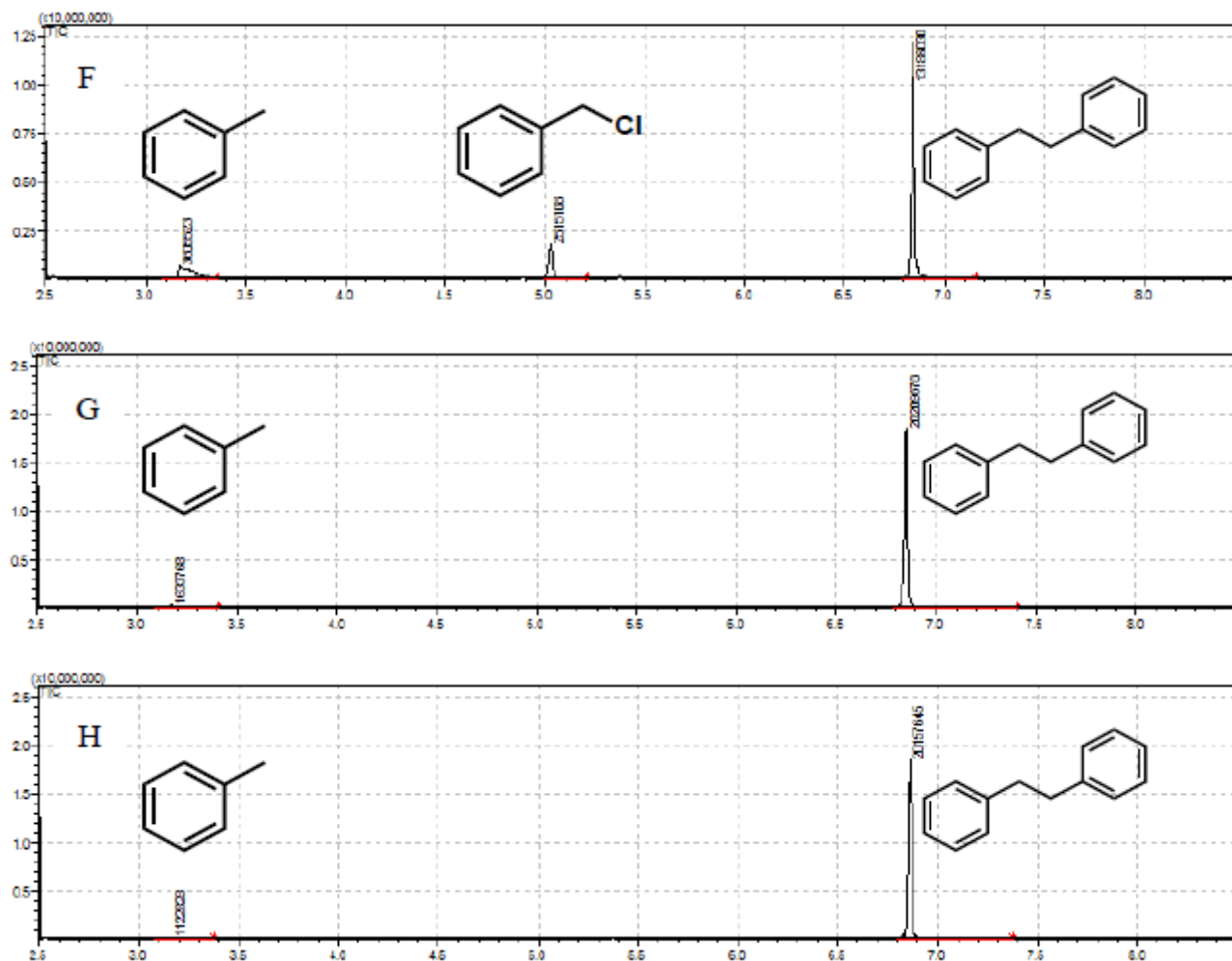


Figure A2.11 (Continued) Representative GC-MS chromatograms of a time progression of catalytic benzyl chloride coupling reactions. Each chromatogram is of a separate reaction stopped after (A) 0, (B) 1, (C) 2, (D) 3, (E) 4, (F) 5, (G) 6, and (H) 7 h.

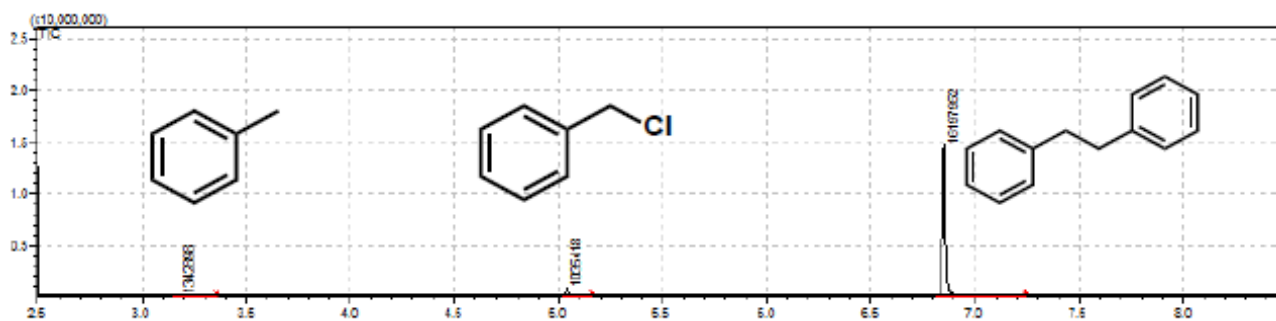


Figure A2.12 Representative GC-MS chromatogram of a catalytic benzyl chloride coupling reaction prepared in a wet glovebox starting from $\text{EuCl}_3 \cdot 6\text{H}_2\text{O}$.

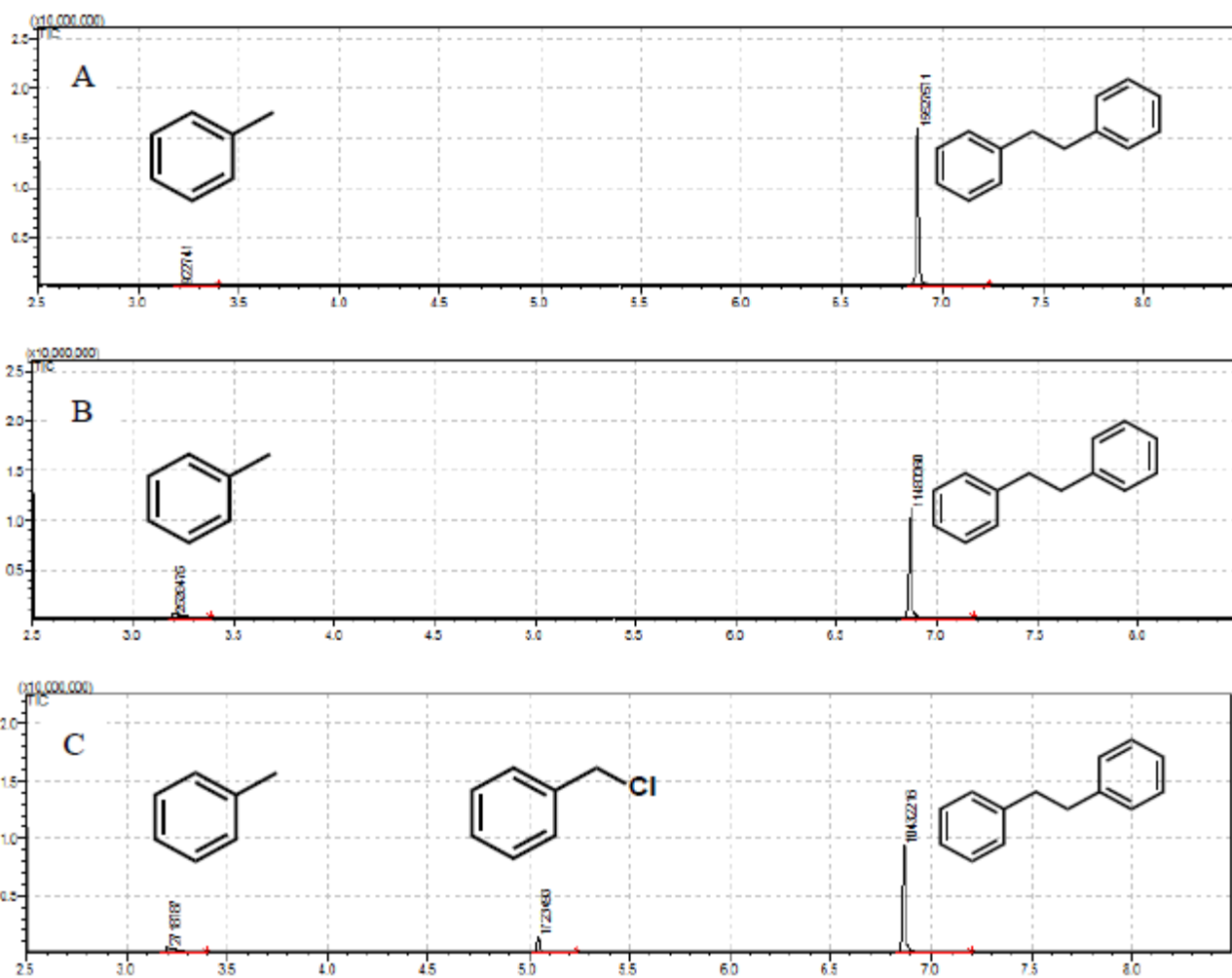


Figure A2.13 Representative GC-MS chromatograms of benzyl chloride coupling reactions run at catalyst loadings of (A) 5, (B) 1, and (C) 0.5%.

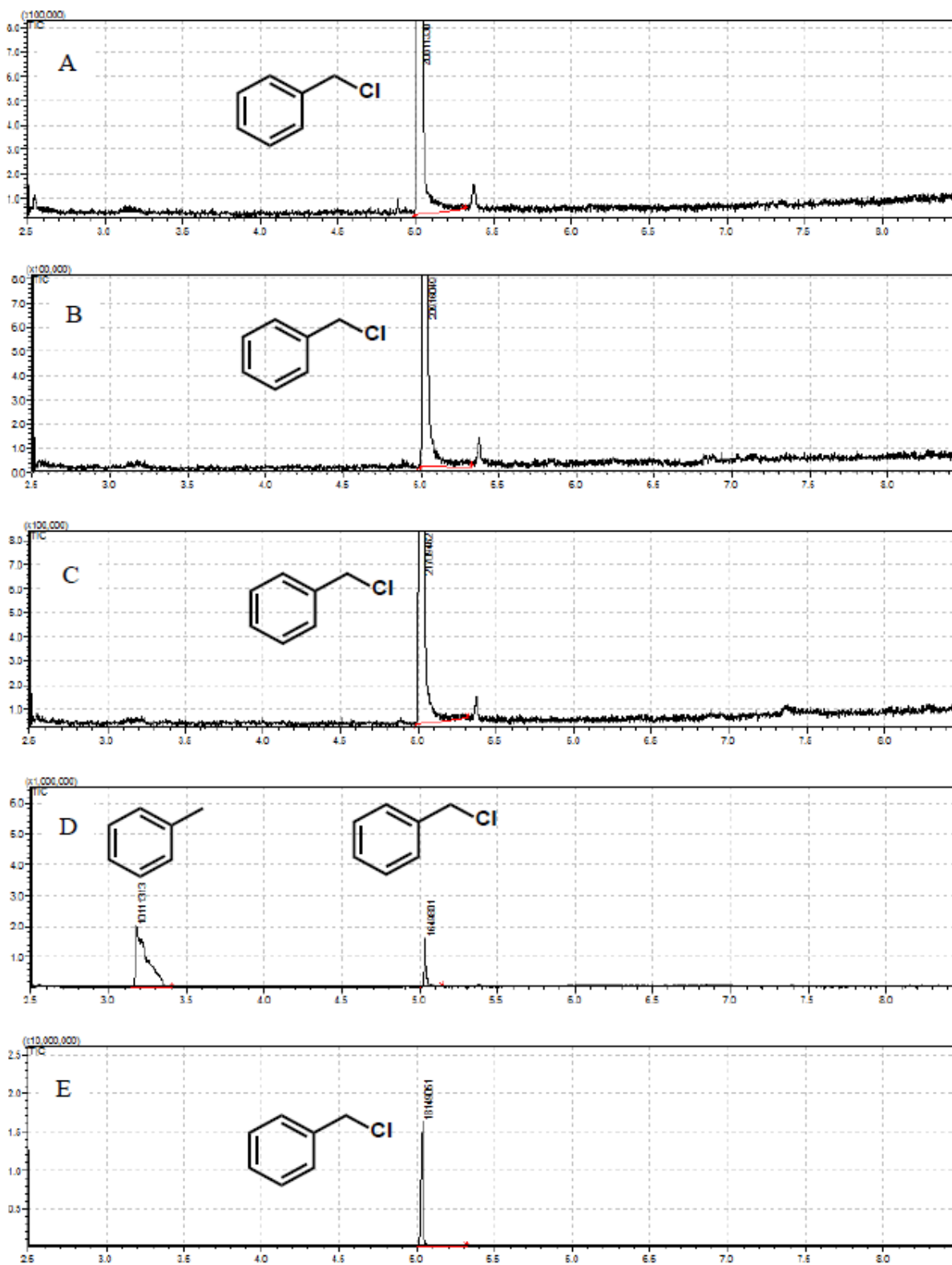


Figure A2.14 GC-MS chromatograms of control reactions (A) in the absence of light; (B) without europium; (C) without **23**; (D) with only zinc and benzyl chloride; and (E) with only benzyl chloride in solution.

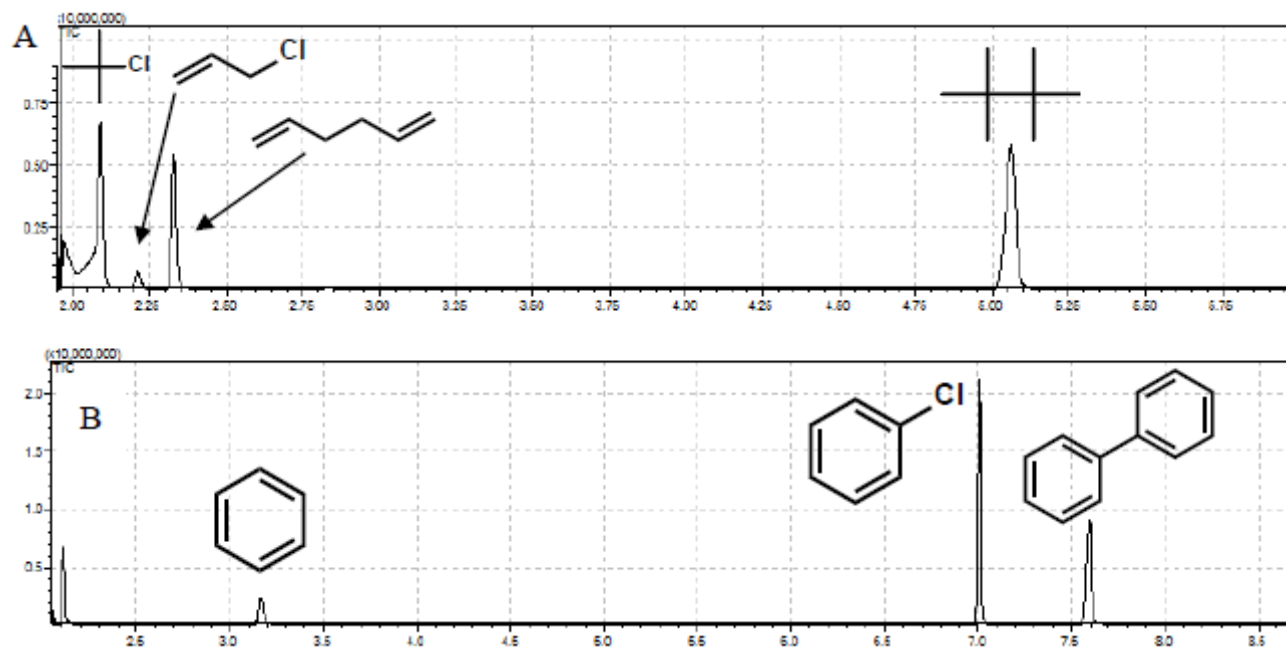


Figure A2.15 Representative GC-MS chromatograms of the calibration solutions for (A) allyl chloride and 2-chloro-2-methylpropane coupling reactions and (B) the chlorobenzene coupling reaction.

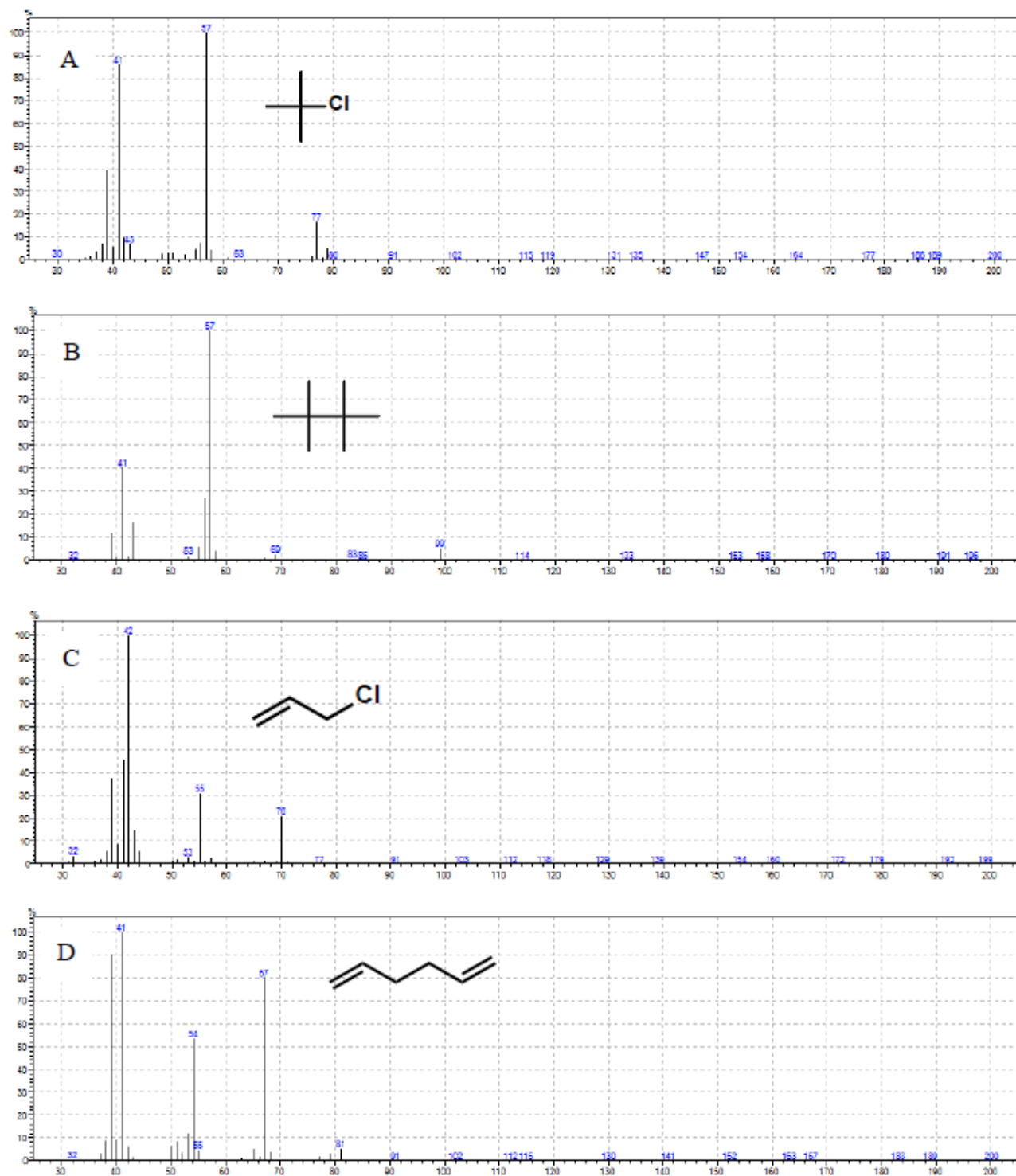


Figure A2.16 (Part 1) Full caption can be found on the following page.

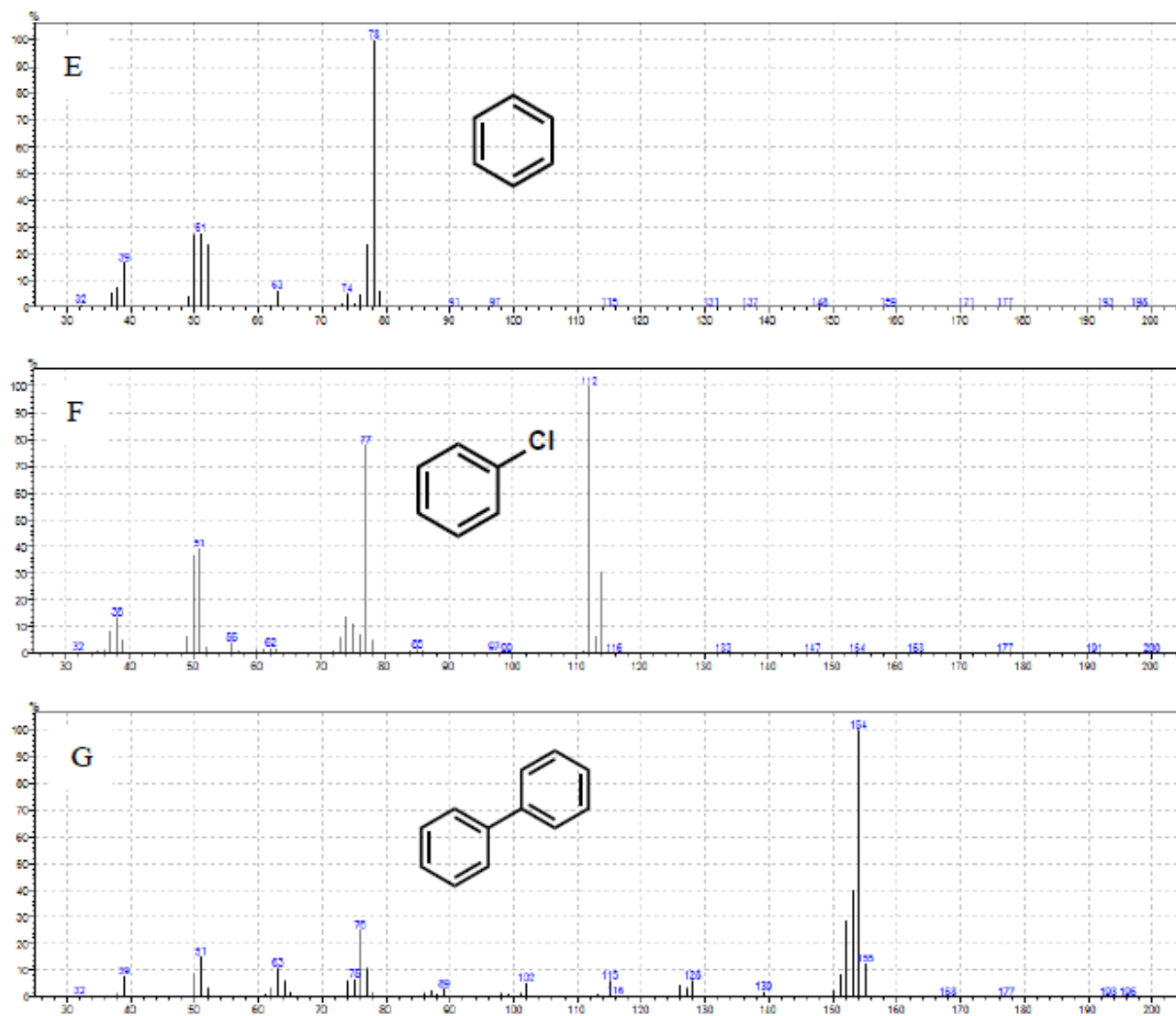


Figure A2.16 (Continued) Mass spectra of (A) 2-chloro-2-methylpropane, (B) 2,2,3,3-tetramethylbutane, (C) allyl chloride, (D) 1,5-hexadiene, (E) benzene, (F) chlorobenzene, and (G) biphenyl.

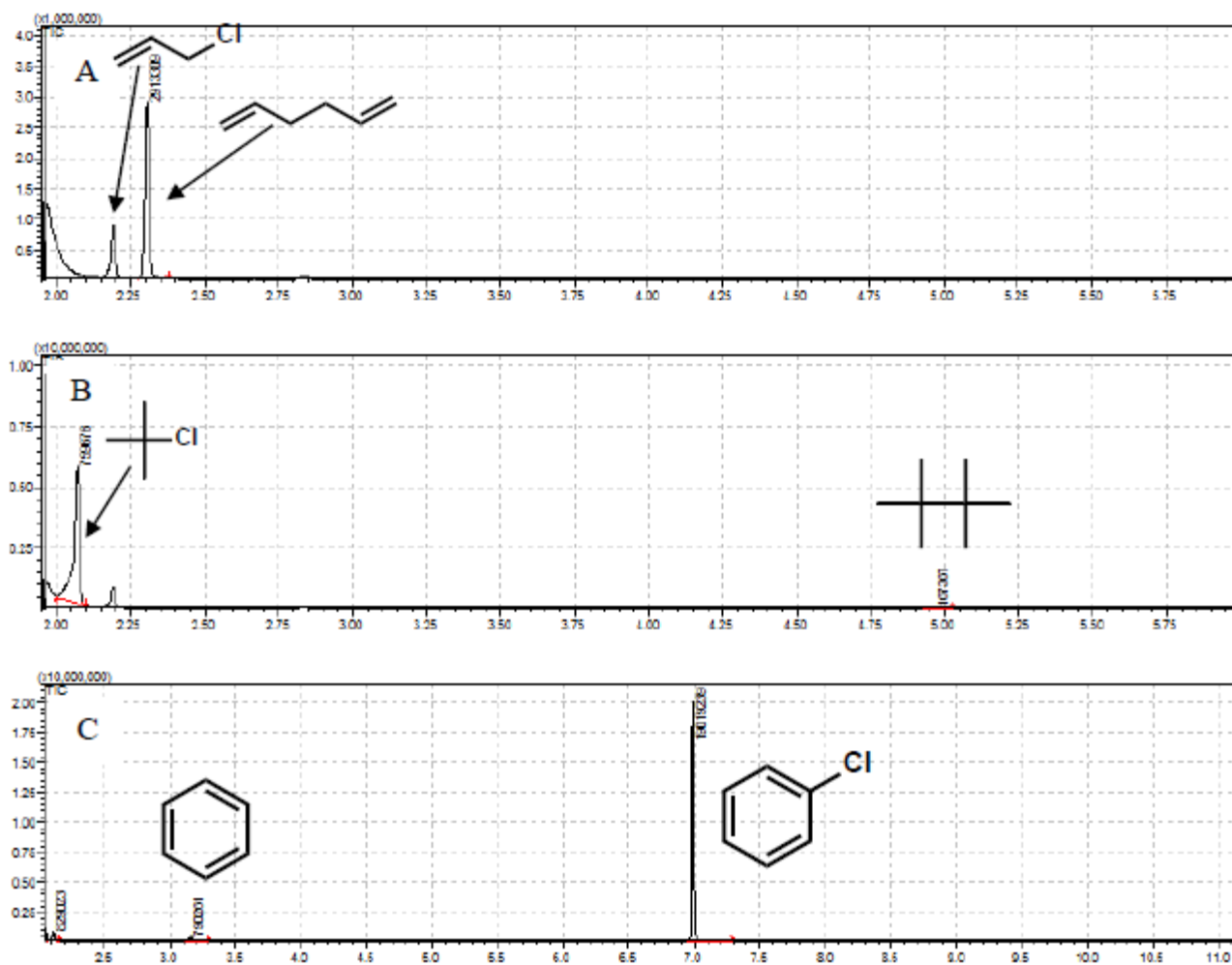


Figure A2.17 Representative GC-MS chromatograms of the products of the (A) allyl chloride coupling reaction, (B) 2-chloro-2-methylpropane coupling reaction, and (C) chlorobenzene coupling reaction.

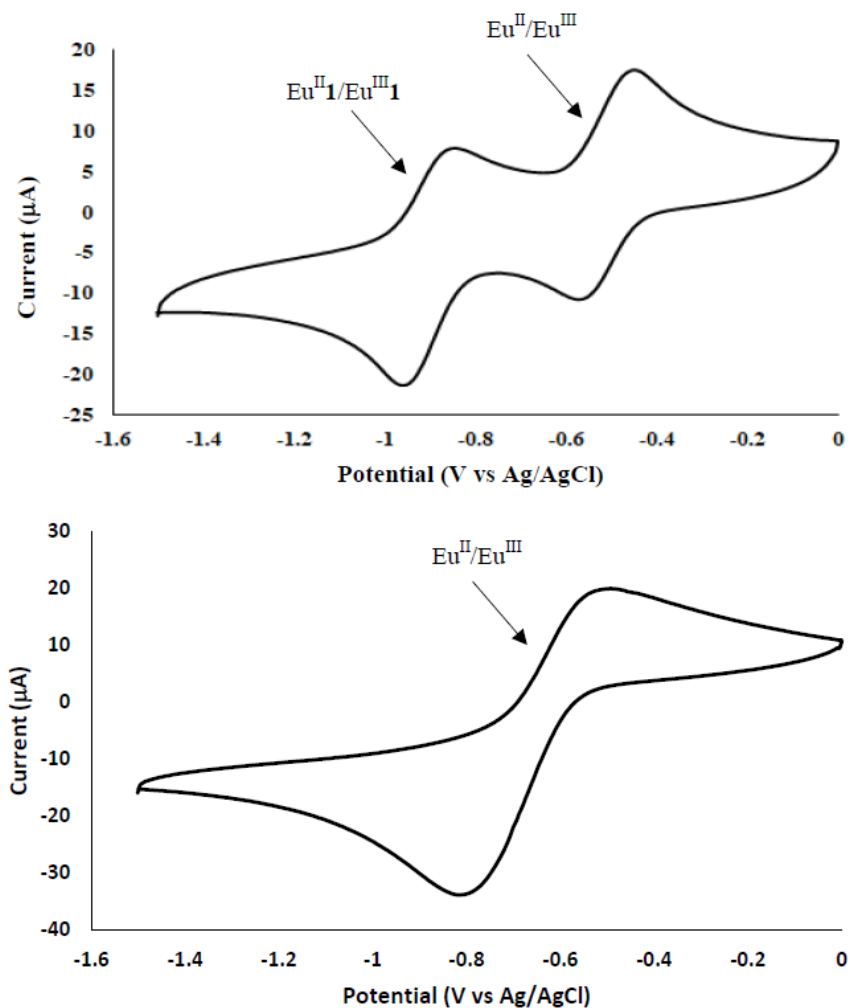


Figure A2.18 Top: Cyclic voltammogram of $\text{Eu}(\text{OTf})_3$ and **23** in DMF. Bottom: Cyclic voltammogram of $\text{Eu}(\text{OTf})_3$ in DMF. Upon addition of ligand **23** to a solution of $\text{Eu}(\text{OTf})_3$, a new peak arises with an $E_{1/2}$ of -0.9 V vs Ag/AgCl.

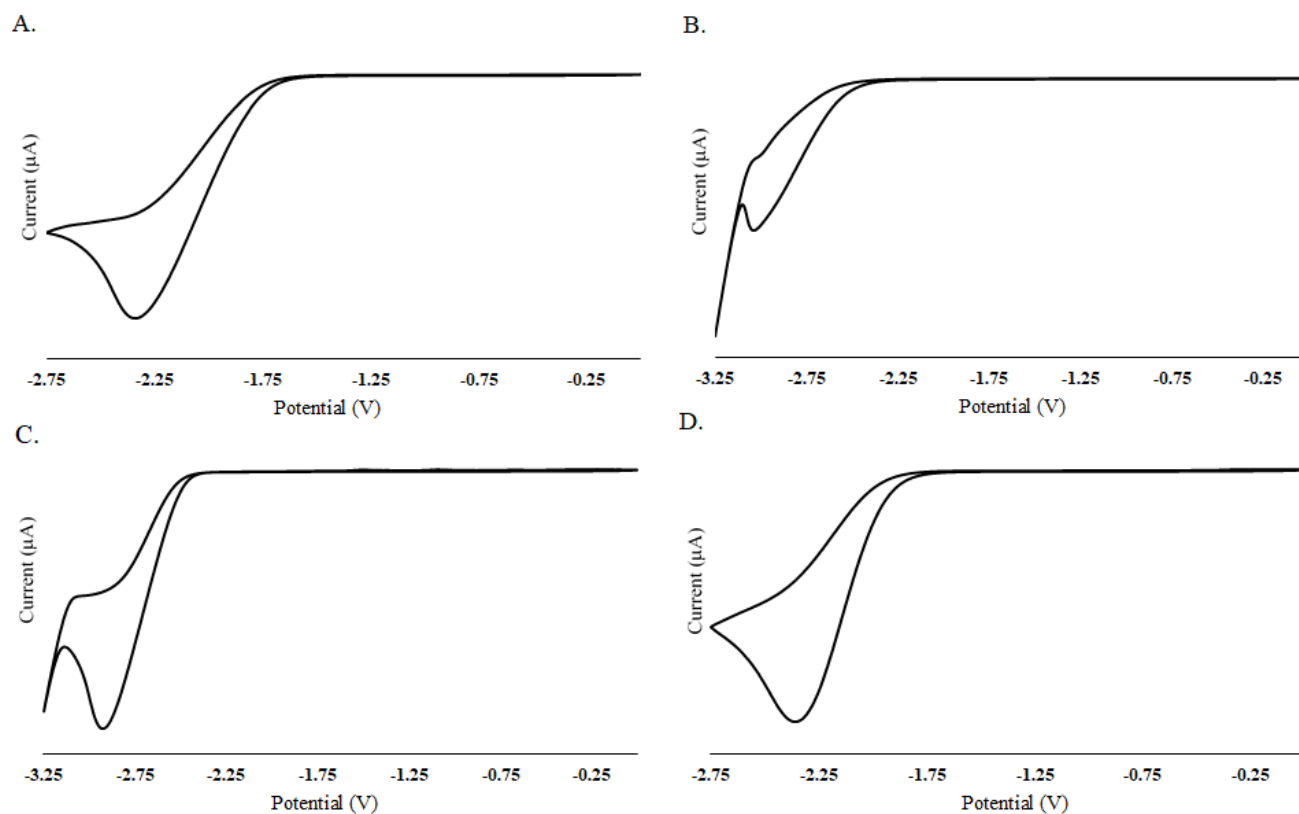


Figure A2.19 Cyclic voltammograms of (A) benzyl chloride, (B) 2-chloro-2-methylpropane, (C) chlorobenzene, and (D) allyl chloride. All potentials are relative to Ag/AgCl.

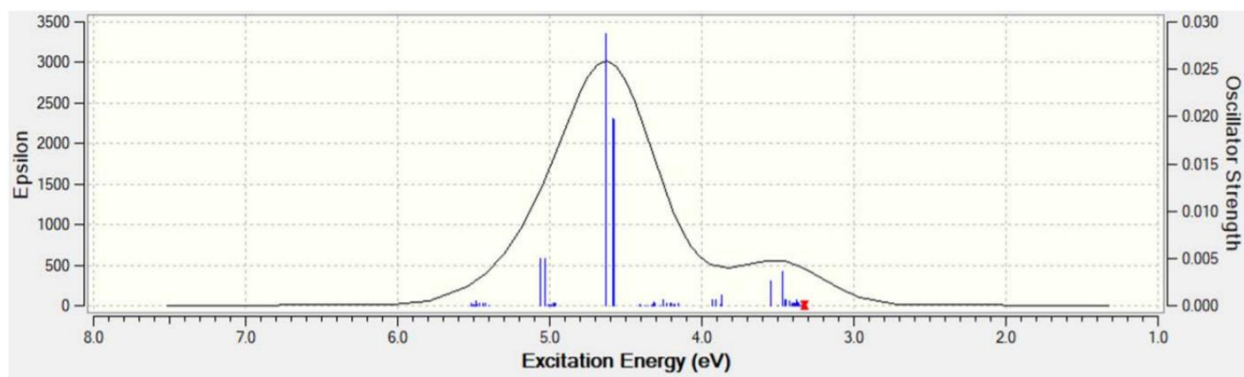


Figure A3.1 Spectrum depicting 80 calculated transitions of the absorption of $[\text{Eu}25]^{2+}$. Computations performed by Brooke A. Corbin.

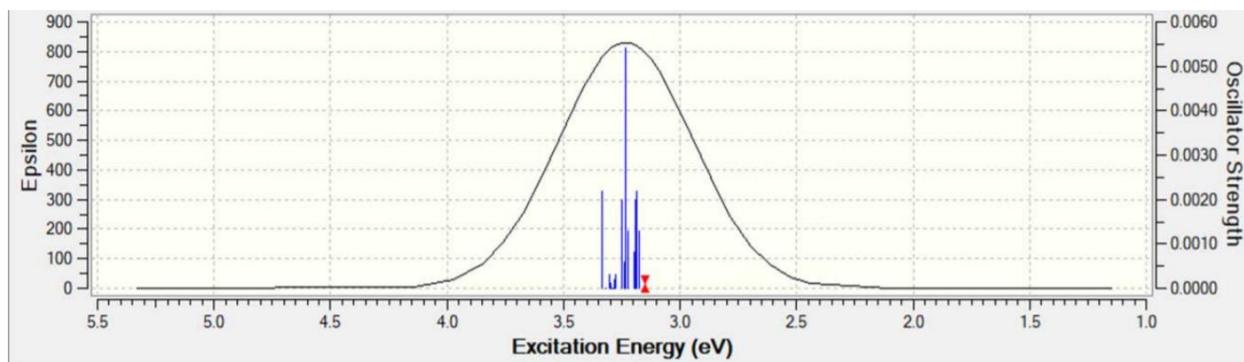


Figure A3.2 Spectrum depicting 80 calculated transitions of the emission of $[\text{Eu}25]^{2+}$. Computations performed by Brooke A. Corbin.

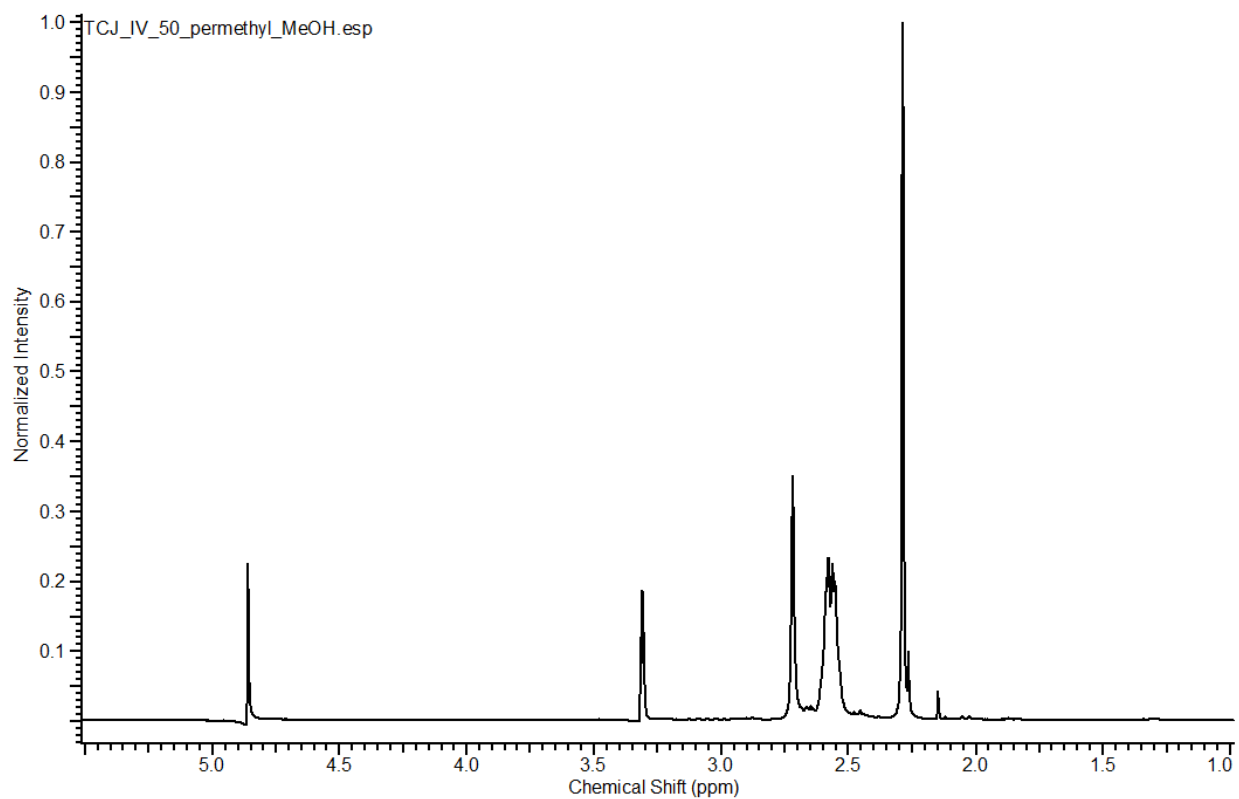


Figure A4.1 ^1H -NMR spectrum of cryptand **25** in d_4 -methanol.

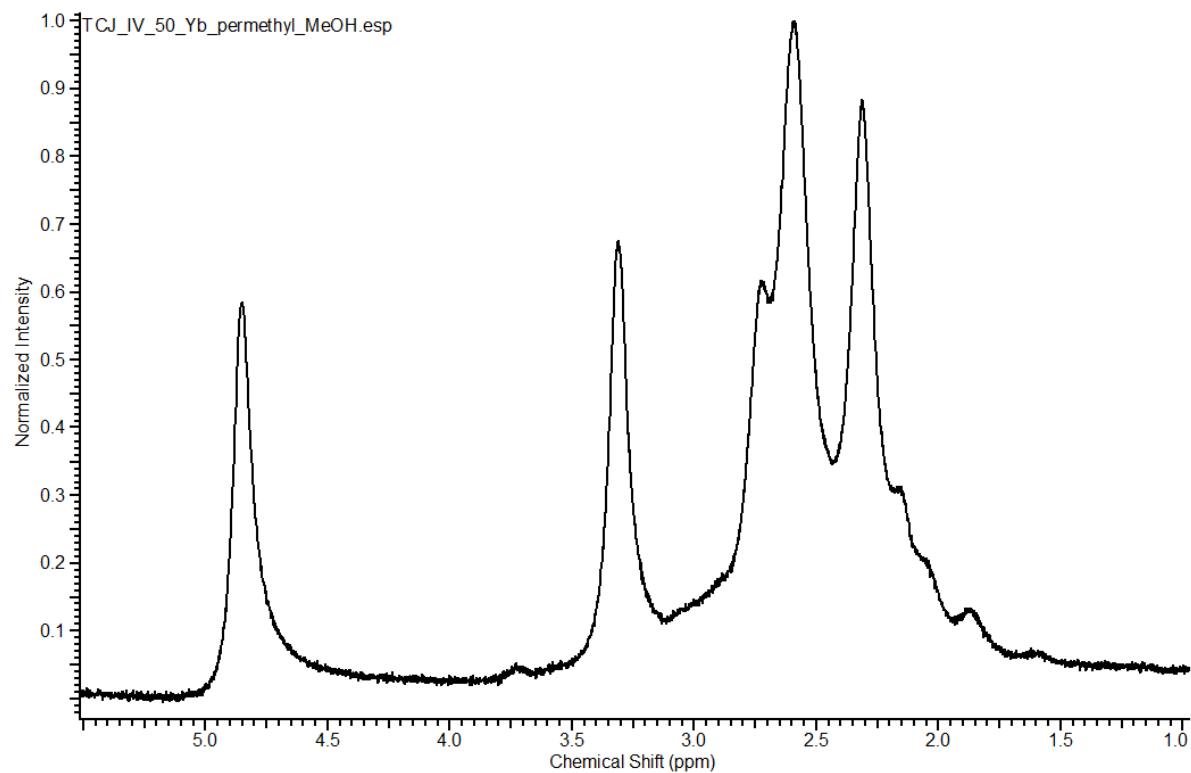


Figure A4.2 ¹H-NMR spectrum of Yb^{II}25 in *d*₄-methanol.

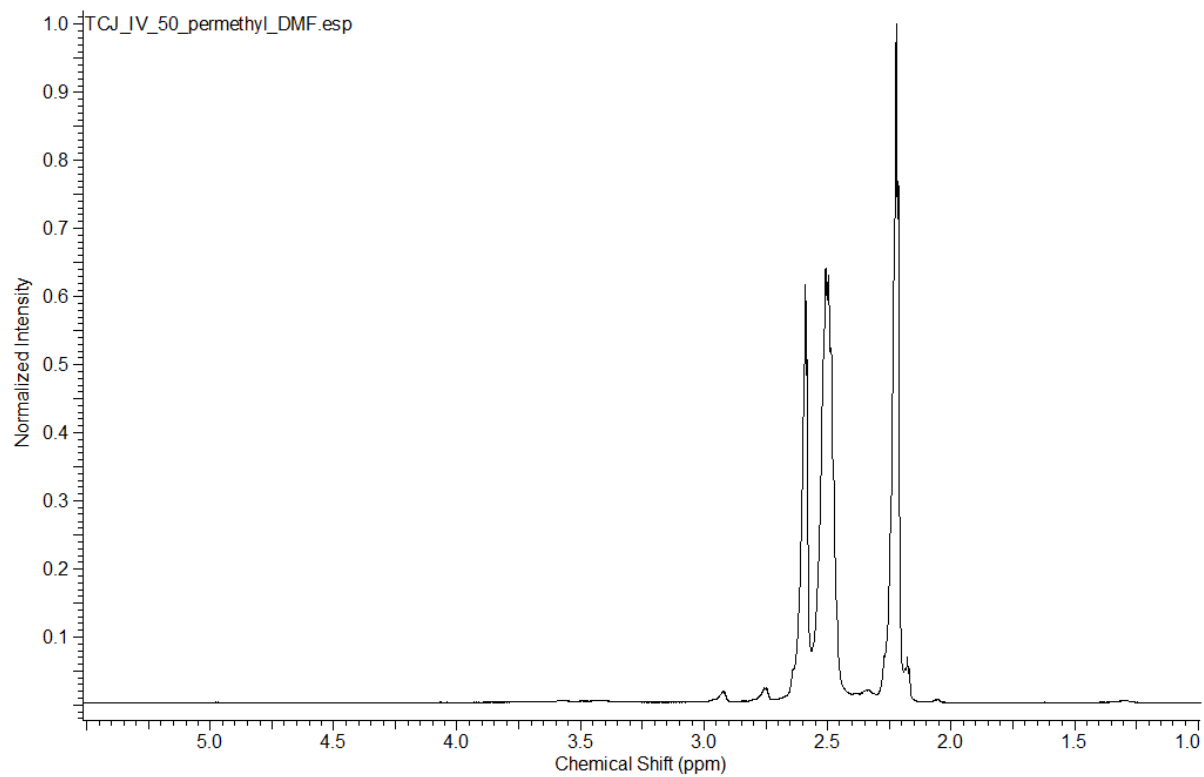


Figure A4.3 ¹H-NMR spectrum of cryptand 25 in *N,N*-dimethylformamide-*d*₇.

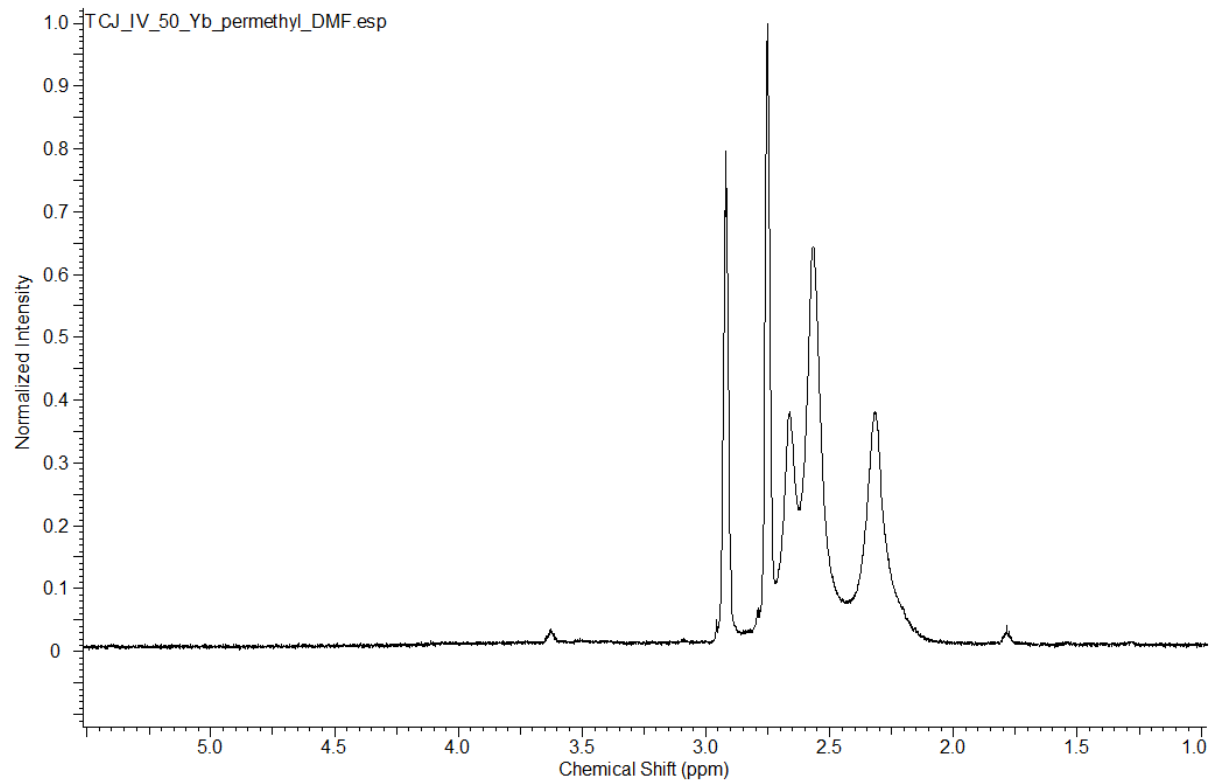


Figure A4.4 $^1\text{H-NMR}$ spectrum of $\text{Yb}^{\text{II}}\mathbf{25}$ in N,N -dimethylformamide- d_7 .

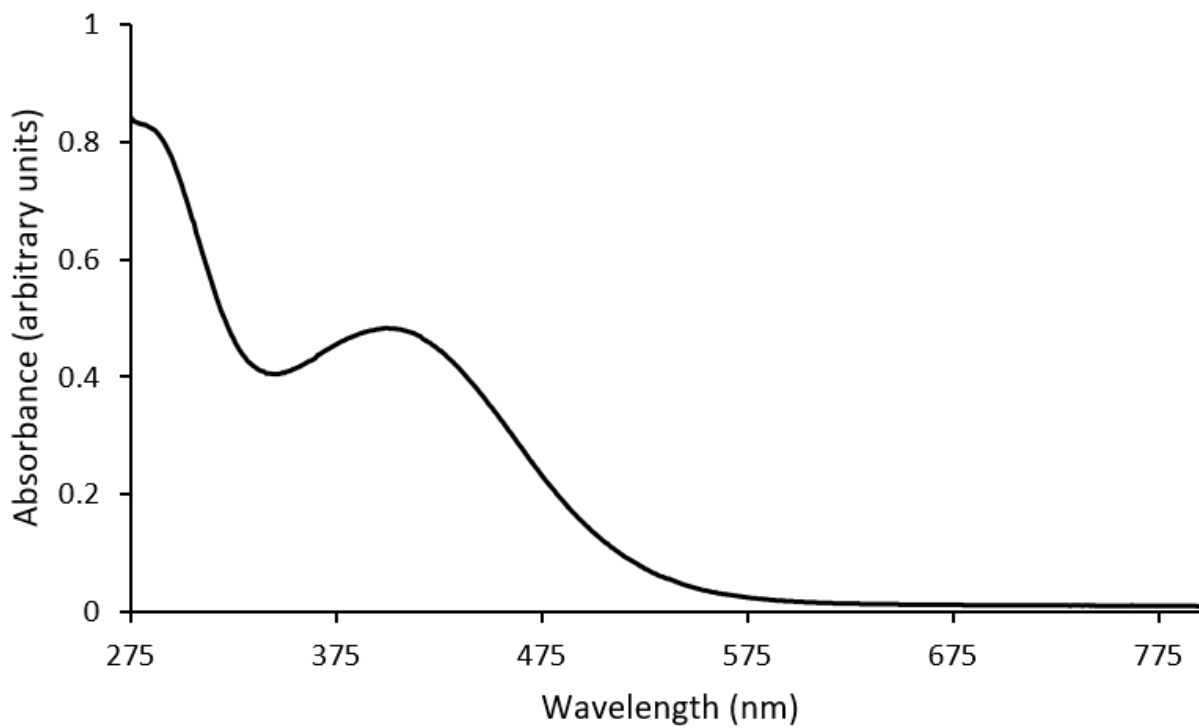


Figure A4.5 UV-visible spectrum of YbI_2 in N,N -dimethylformamide.

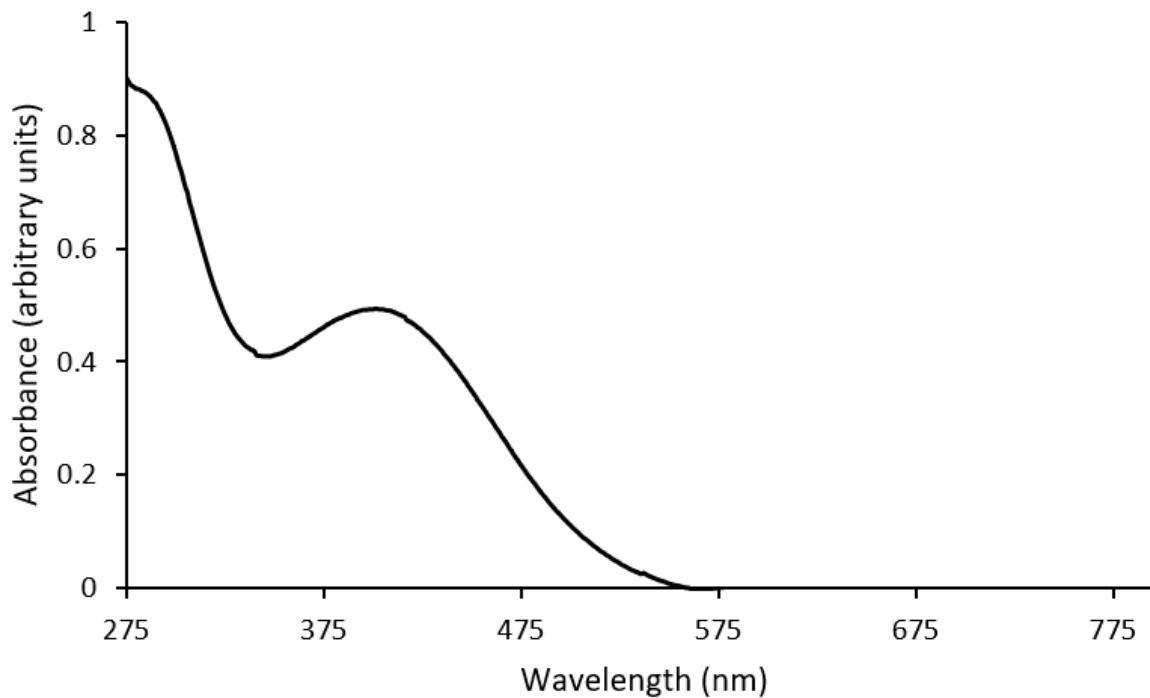


Figure A4.6 UV-visible spectrum of Yb^{II}25 in *N,N*-dimethylformamide.

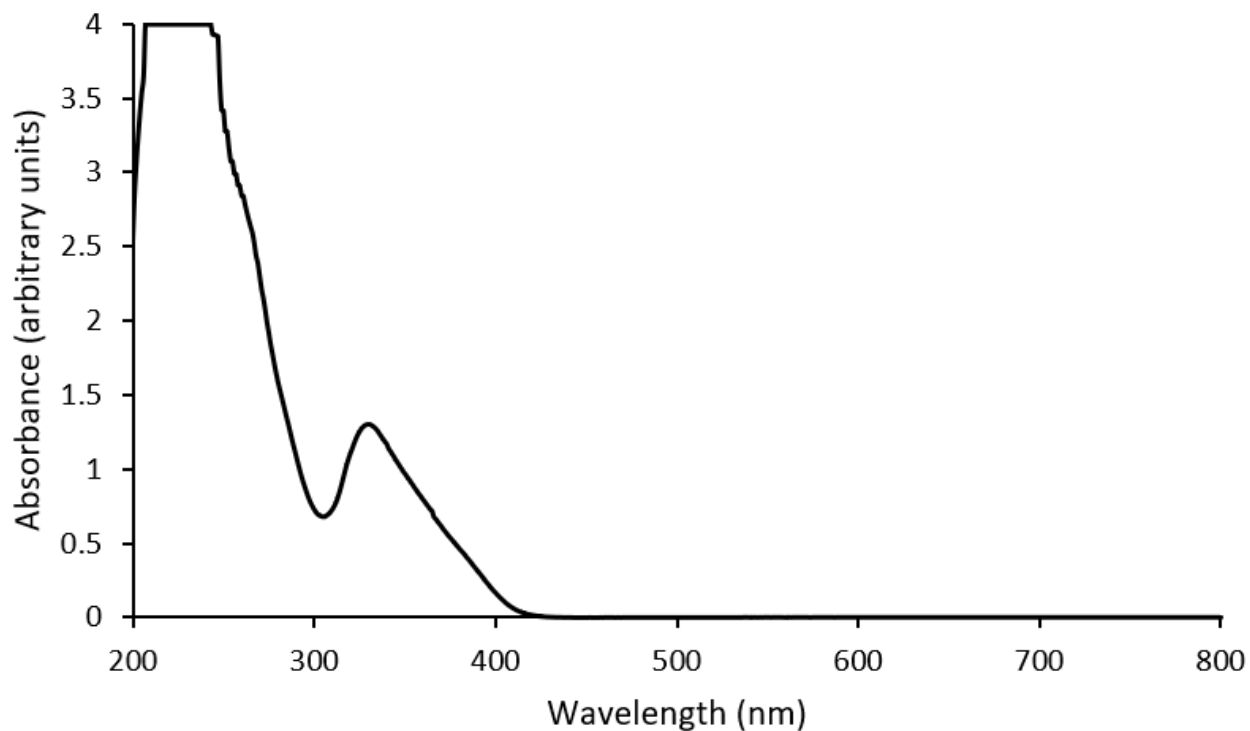


Figure A4.7 UV-visible spectrum of EuI₂ in methanol.

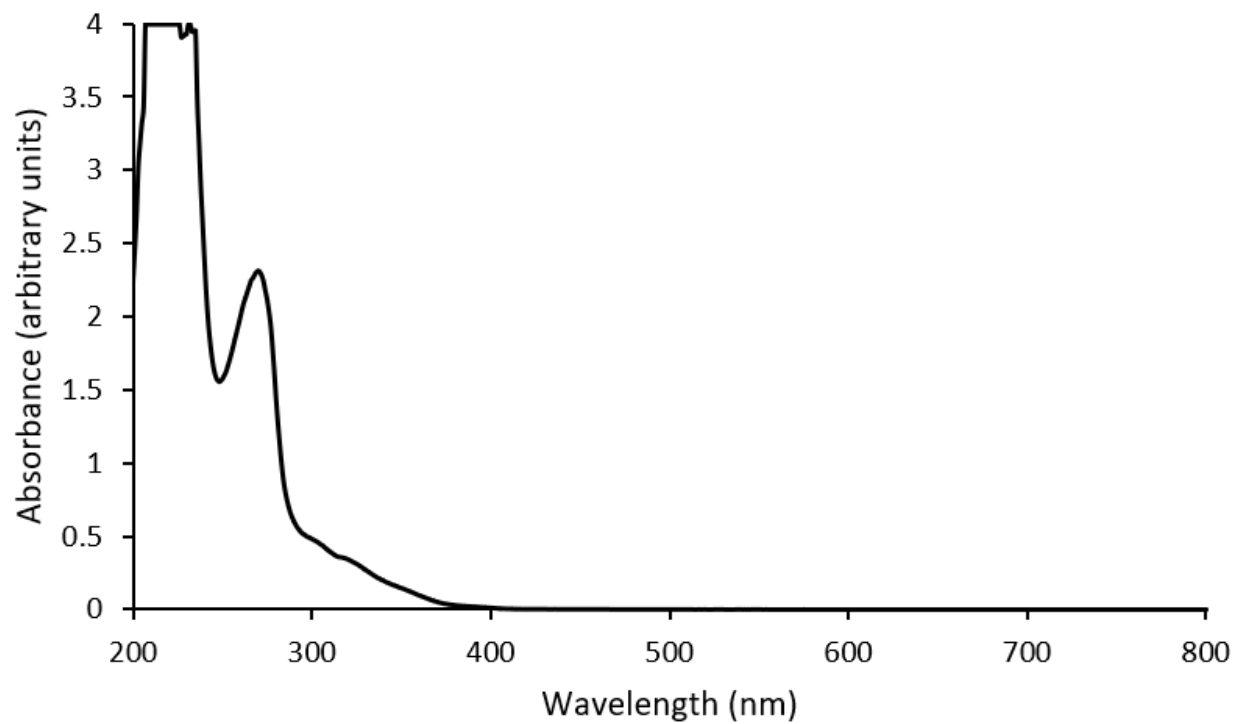


Figure A4.8 UV-visible spectrum of Eu^{II} 41 in methanol.

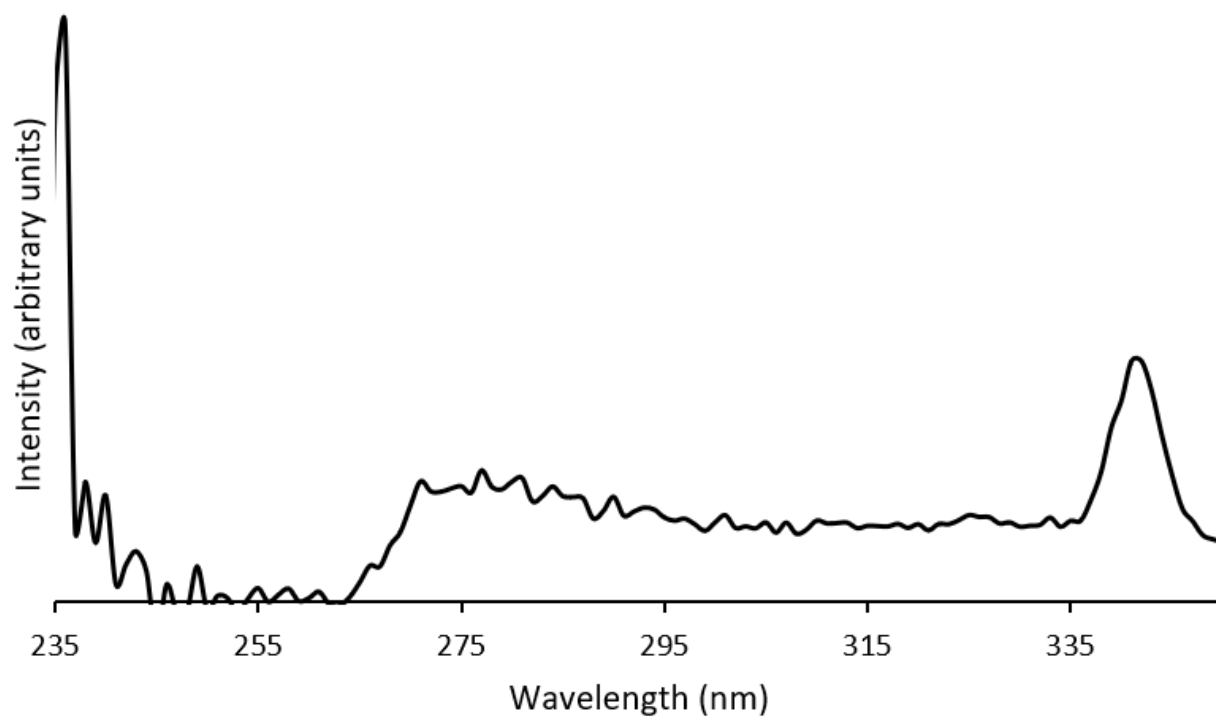


Figure A4.9 Excitation spectrum of YbI_2 in *N,N*-dimethylformamide.

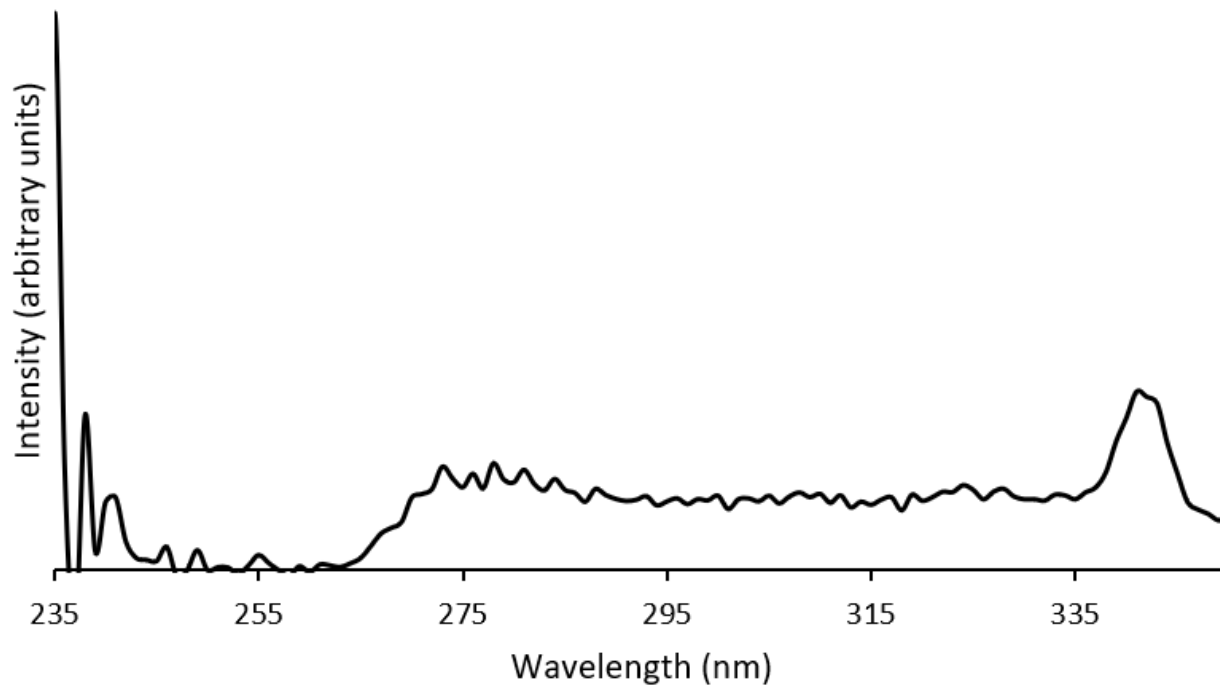


Figure A4.10 Excitation spectrum of $\text{Yb}^{\text{II}}\mathbf{25}$ in *N,N*-dimethylformamide.

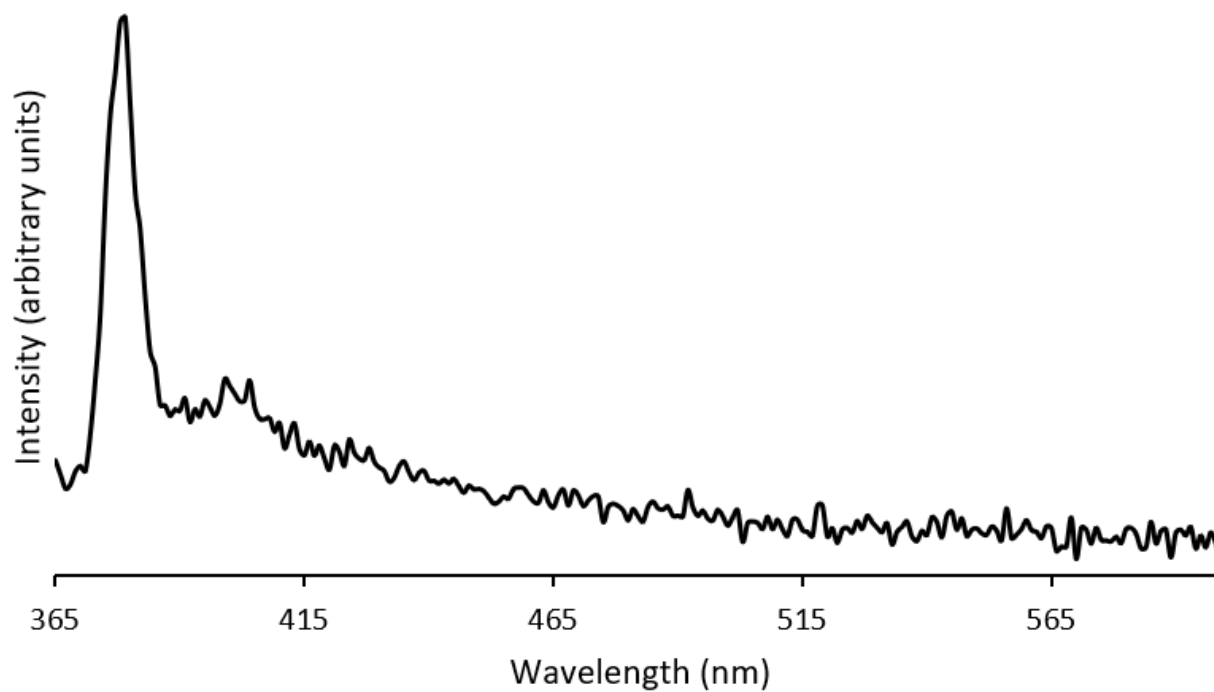


Figure A4.11 Emission spectrum of YbI_2 in *N,N*-dimethylformamide.

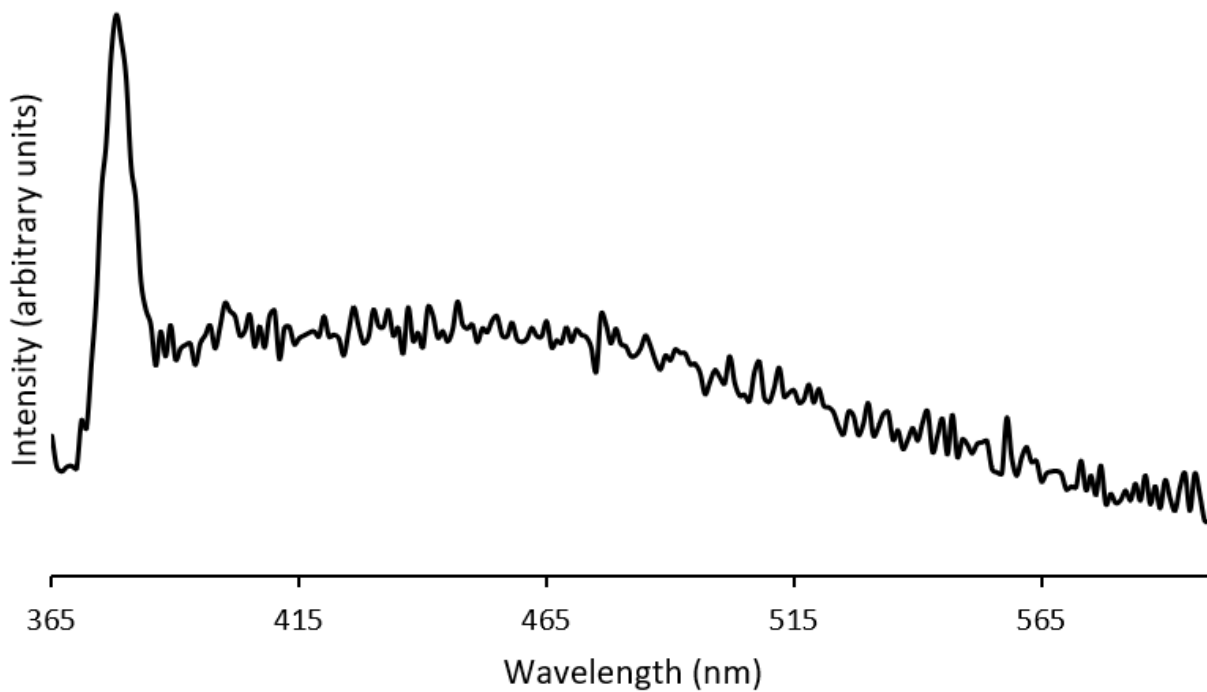


Figure A4.12 Emission spectrum of $\text{Yb}^{\text{II}}\mathbf{25}$ in *N,N*-dimethylformamide.

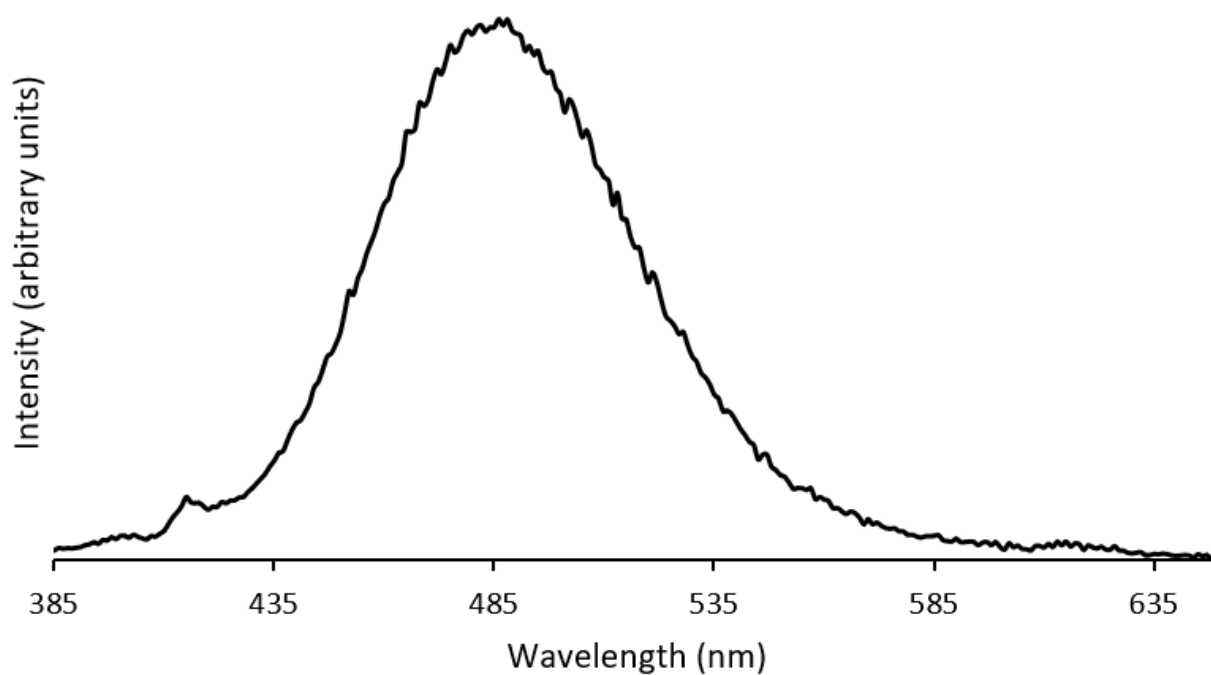


Figure A4.13 Emission spectrum of EuI_2 in methanol.

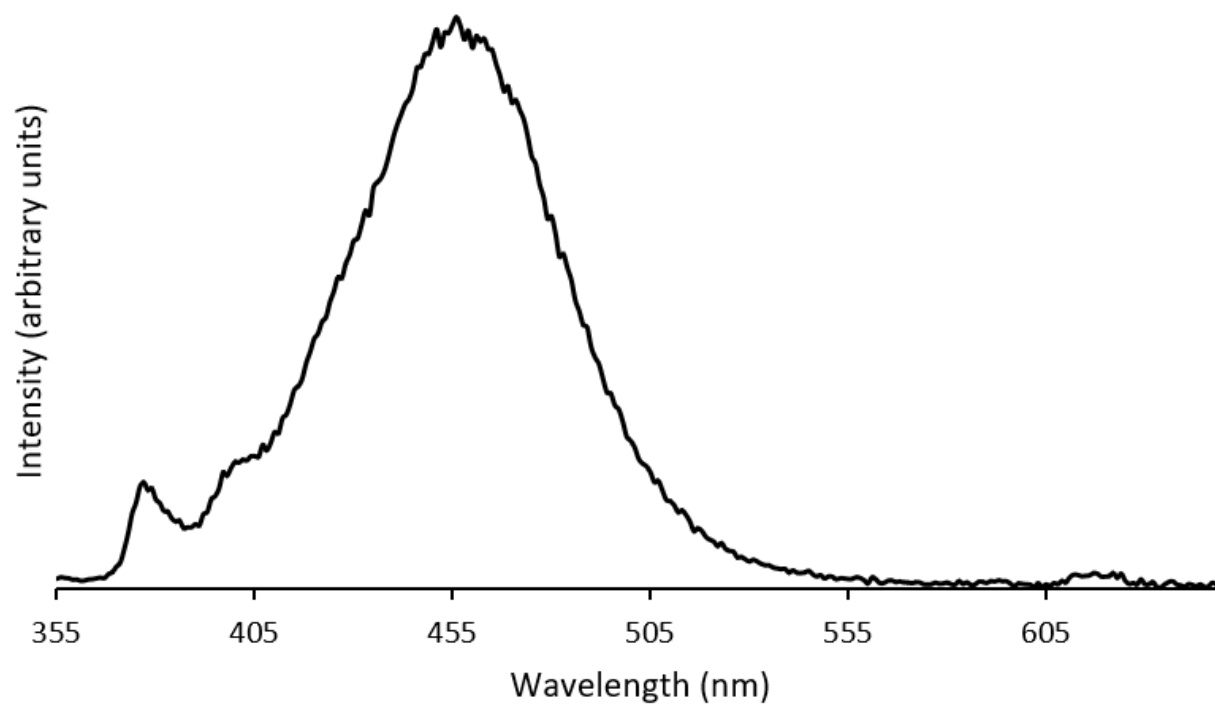


Figure A4.14 Emission spectrum of $\text{Eu}^{\text{II}}\mathbf{41}$ in methanol.

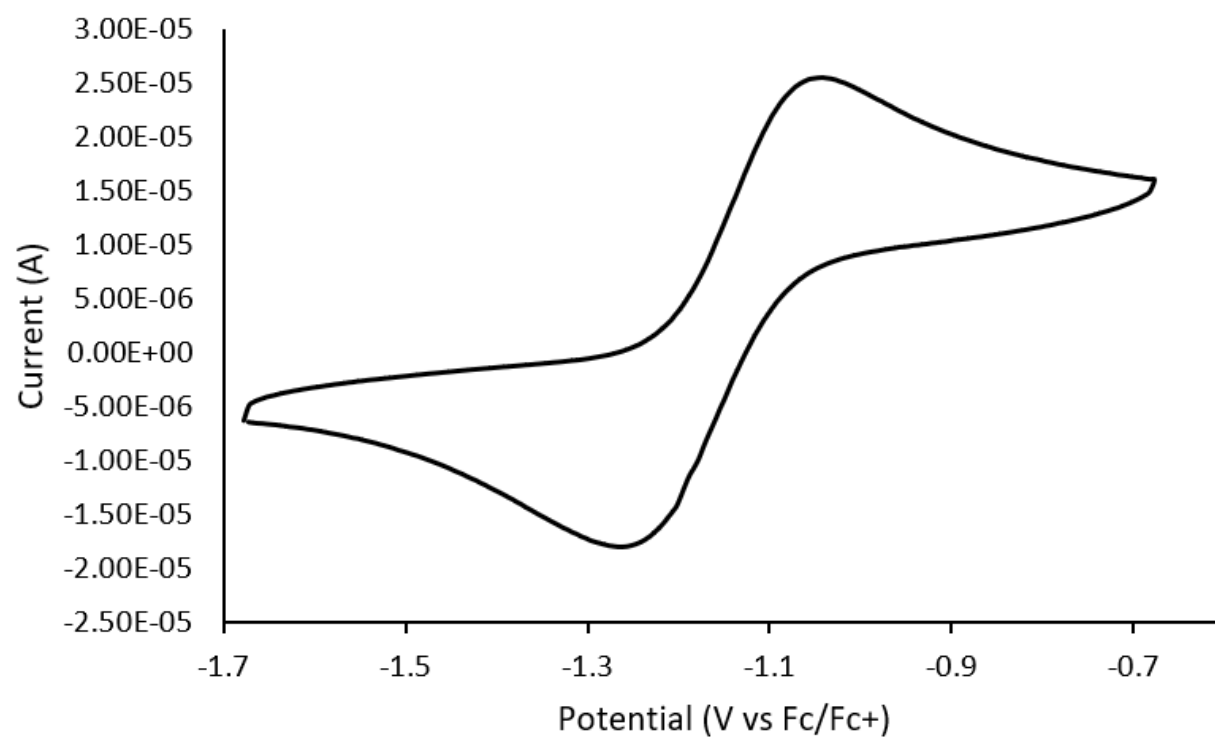


Figure A4.15 Cyclic voltammogram of EuI_2 in *N,N*-dimethylformamide.

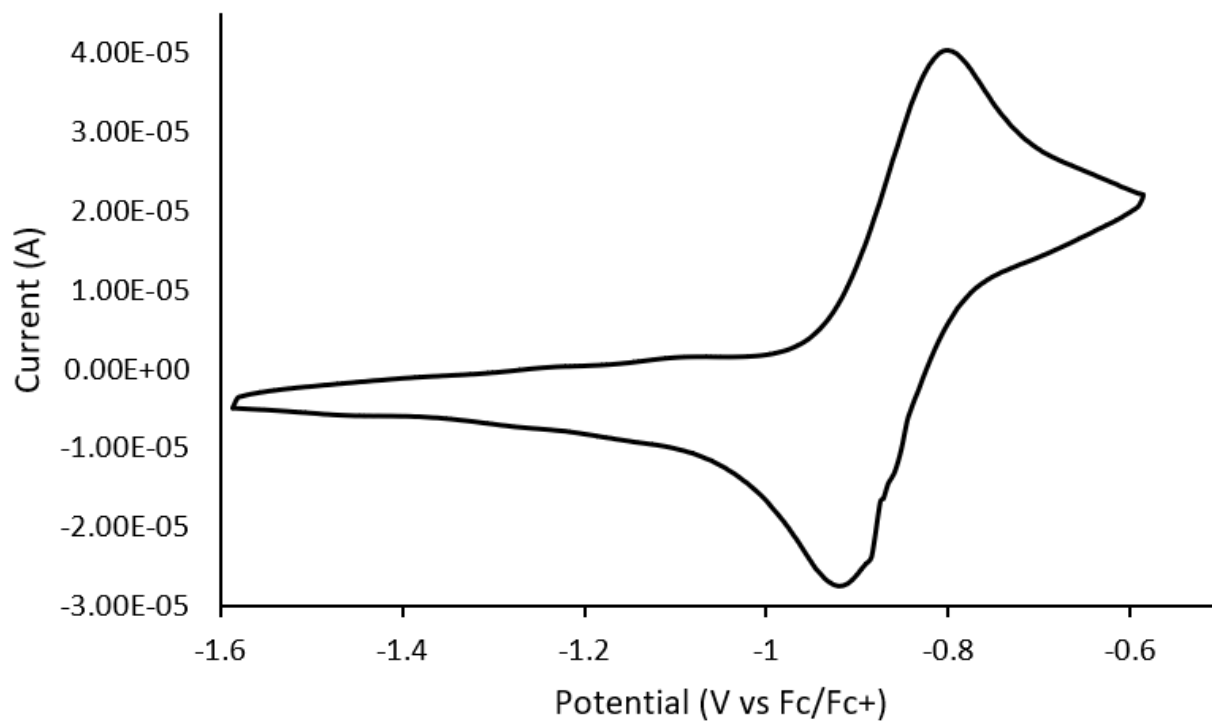


Figure A4.16 Cyclic voltammogram of Eu^{II}23 in *N,N*-dimethylformamide.

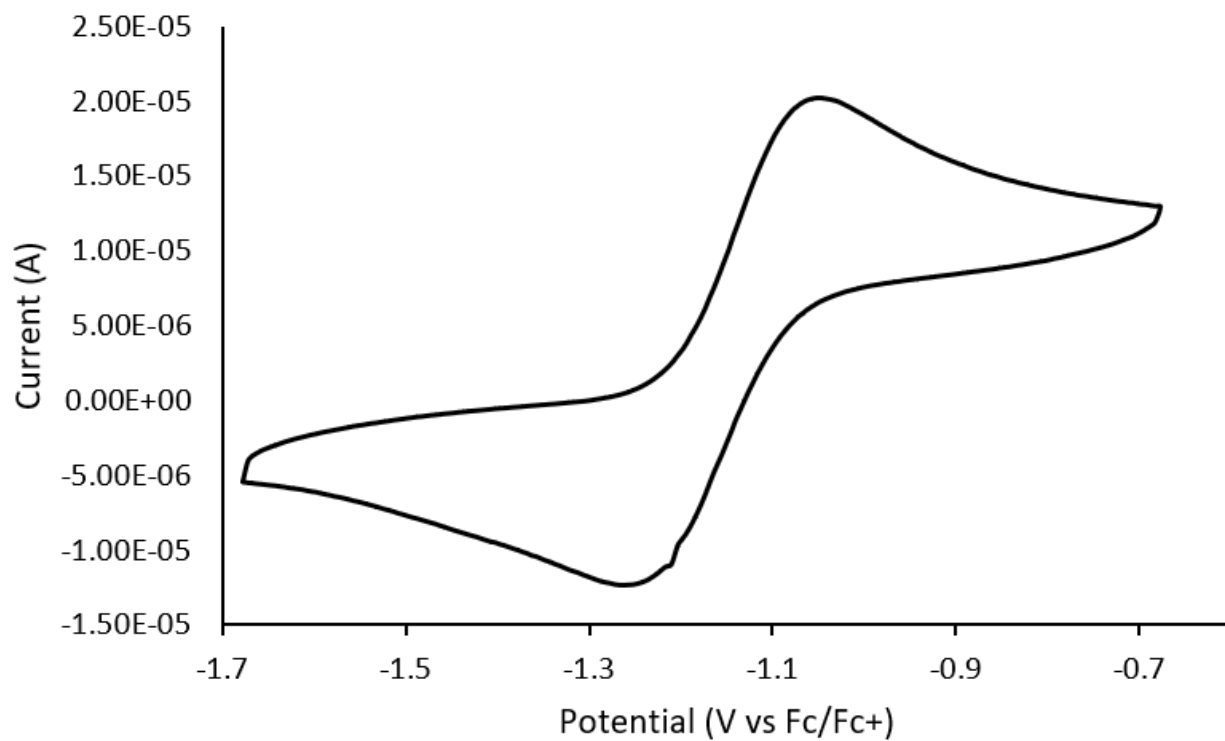


Figure A4.17 Cyclic voltammogram of Eu^{II}25 in *N,N*-dimethylformamide.

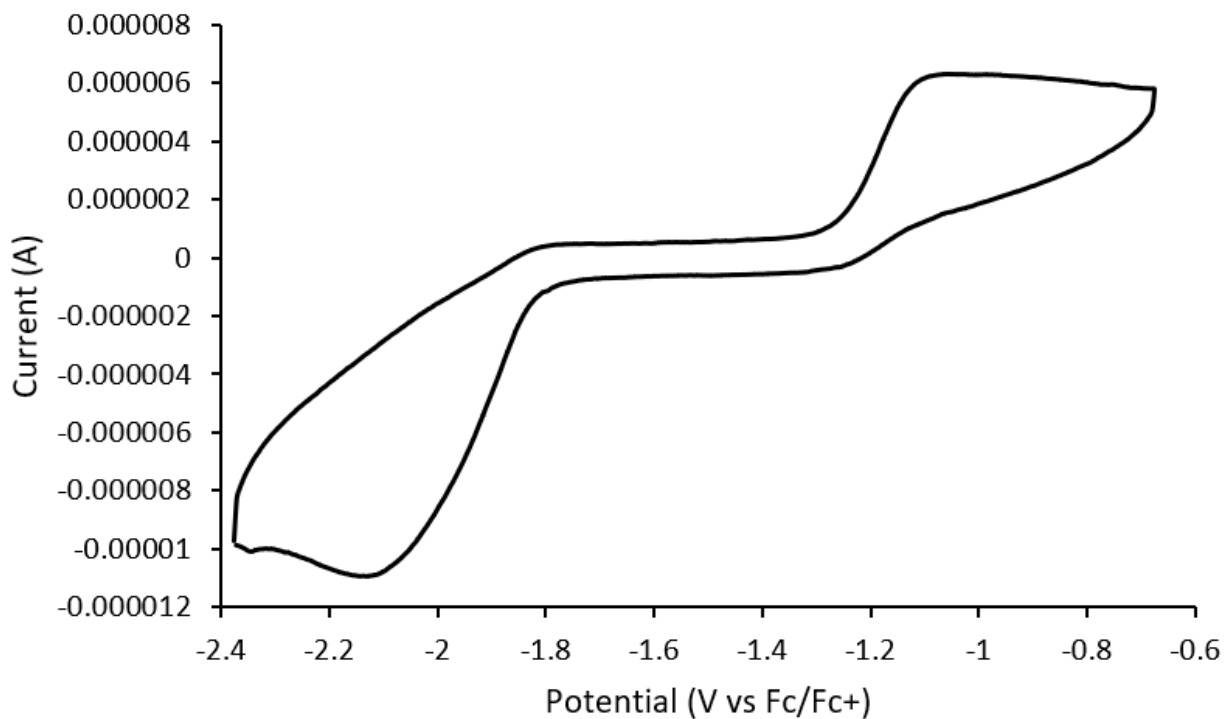


Figure A4.18 Cyclic voltammogram of oxidized Yb^{II}17 in *N,N*-dimethylformamide.

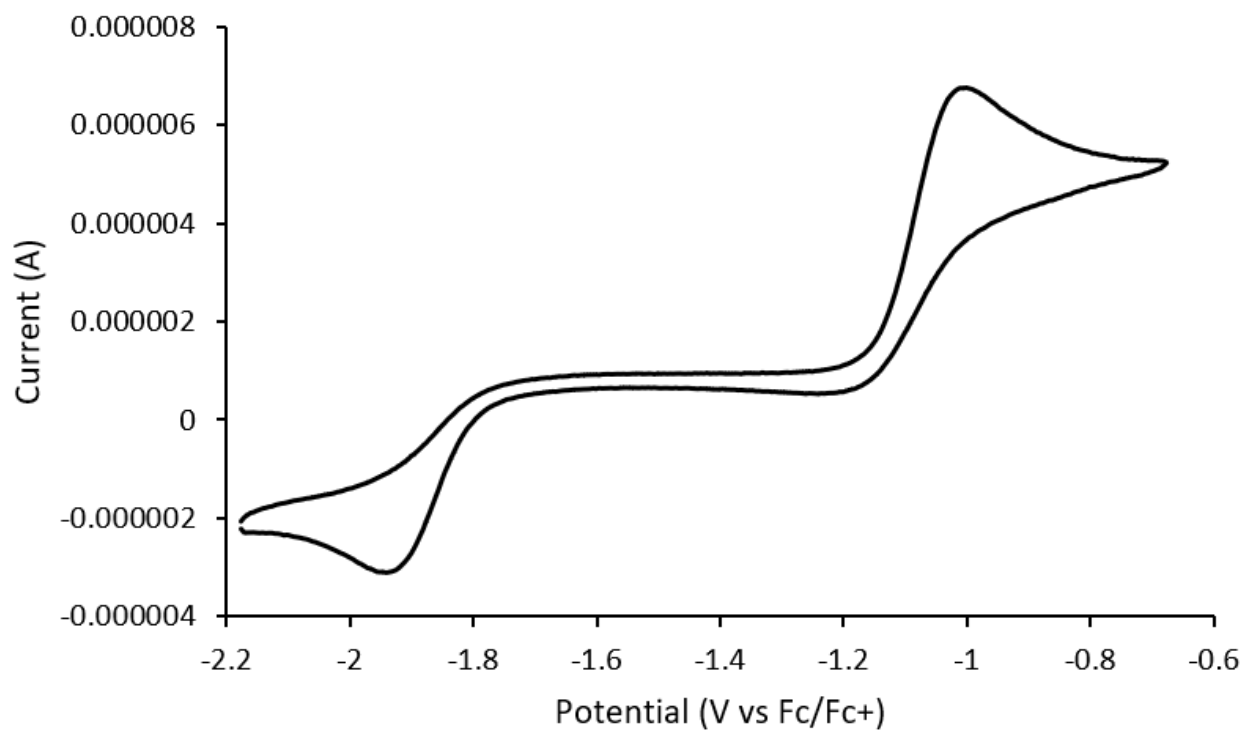


Figure A4.19 Cyclic voltammogram of Yb^{II}41 in *N,N*-dimethylformamide with a scan rate of 10 mV/s.

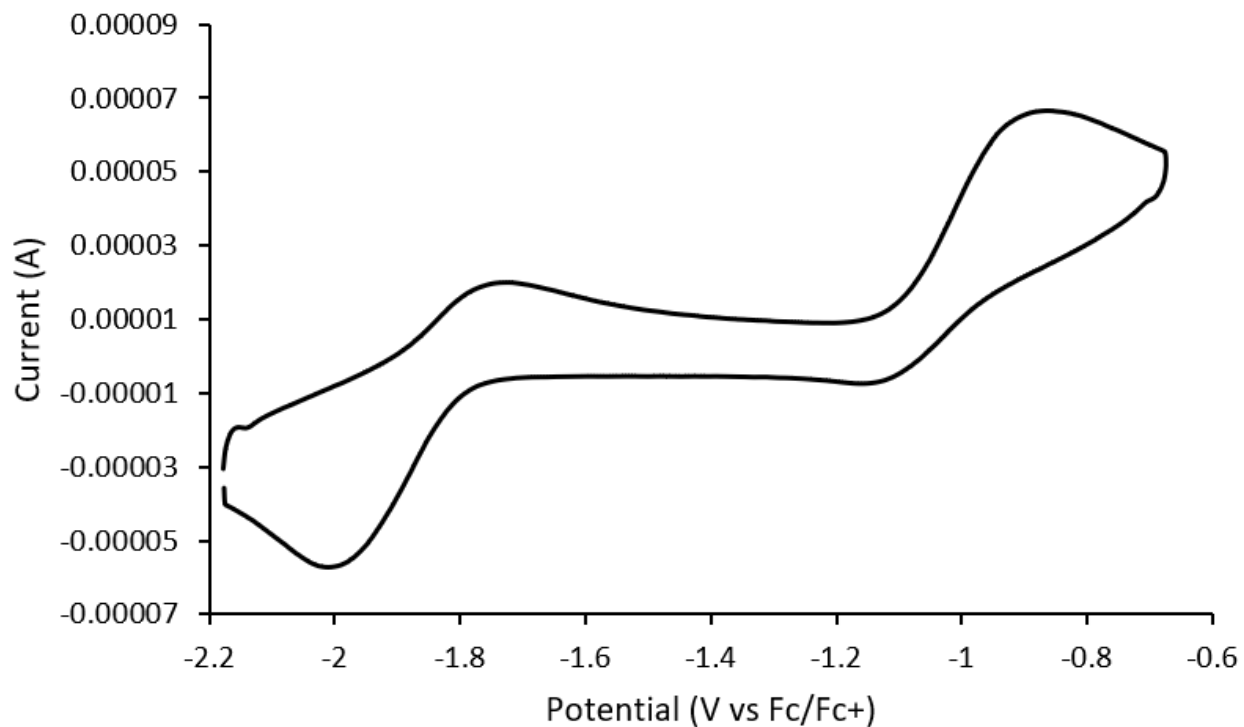


Figure A4.20 Cyclic voltammogram of $\text{Yb}^{\text{II}}\mathbf{41}$ in *N,N*-dimethylformamide with a scan rate of 1 V/s.

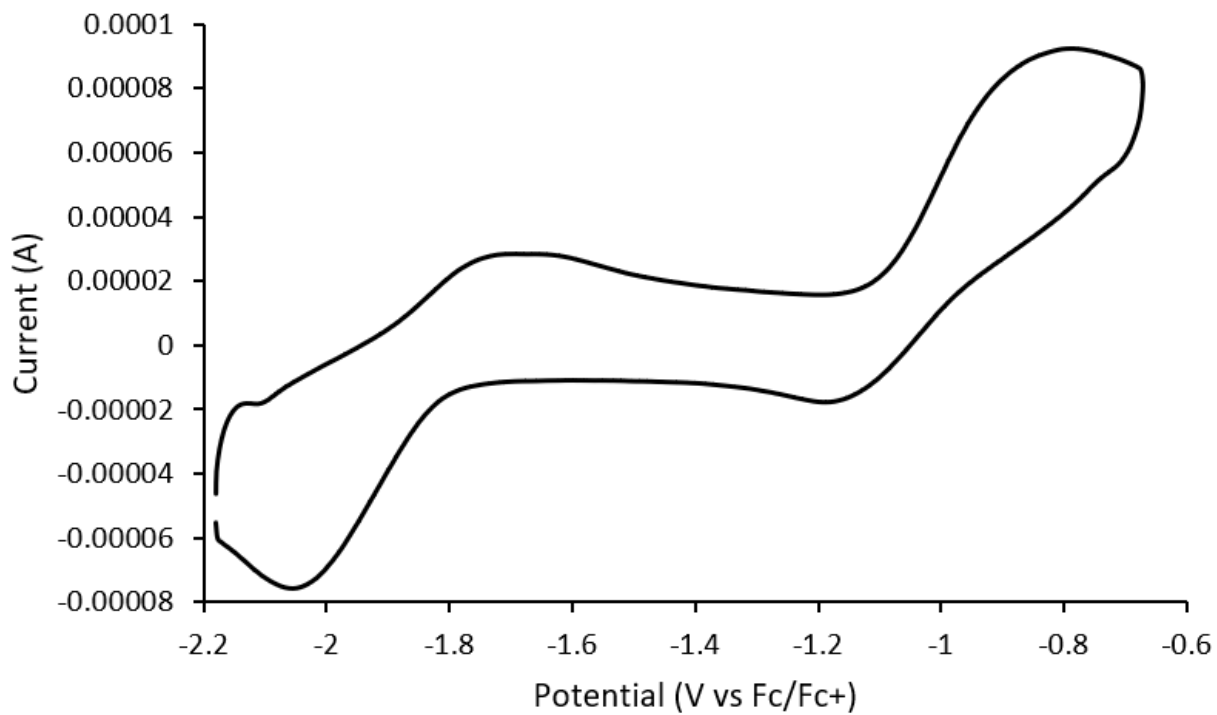


Figure A4.21 Cyclic voltammogram of $\text{Yb}^{\text{II}}\mathbf{41}$ in *N,N*-dimethylformamide with a scan rate of 2 V/s.

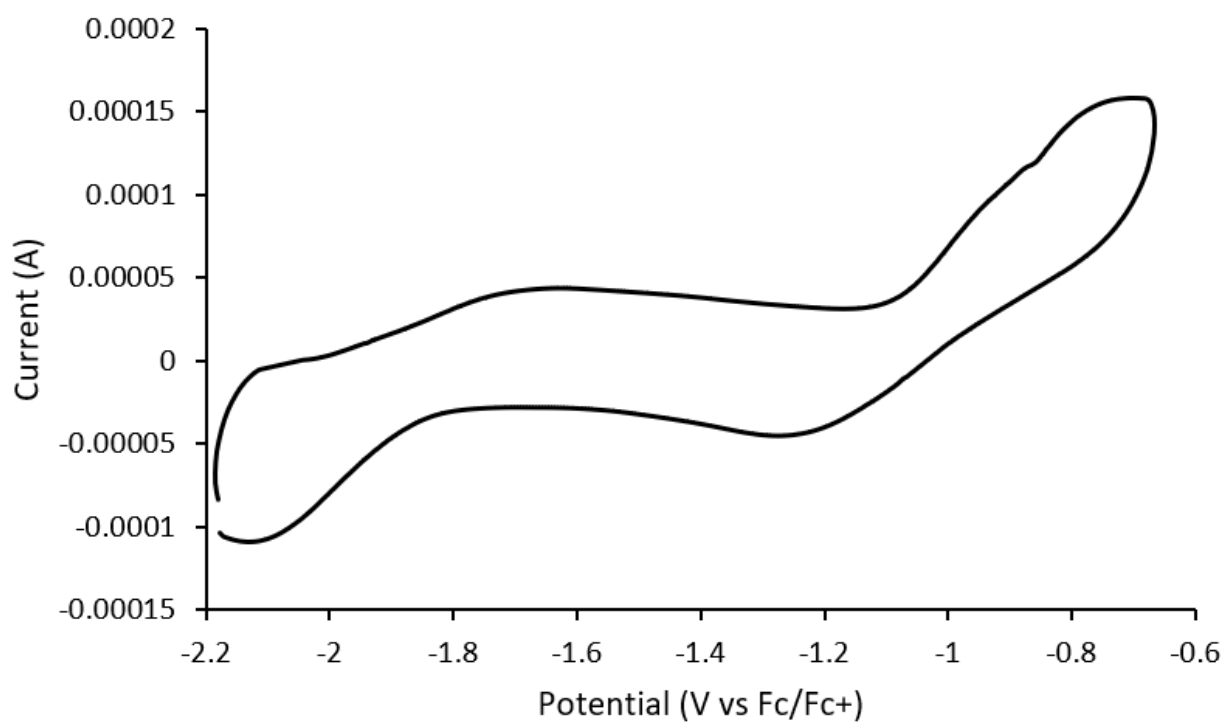


Figure A4.22 Cyclic voltammogram of $\text{Yb}^{\text{II}}\mathbf{41}$ in *N,N*-dimethylformamide with a scan rate of 5 V/s.

APPENDIX B: PERMISSIONS

Permission to reproduce “Jenks, T. C.; Bailey, M. D.; Hovey, J. L.; Fernando, S.; Basnayake, G.; Cross, M. E.; Li, W.; Allen, M. J. “First use of a divalent lanthanide for visible-light-promoted photoredox catalysis” *Chem. Sci.* **2018**, *9*, 1273–1278.” for use in Chapter 2:

First use of a divalent lanthanide for visible-light-promoted photoredox catalysis

T. C. Jenks, M. D. Bailey, Jessica L. Hovey, S. Fernando, G. Basnayake, M. E. Cross, W. Li and M. J. Allen, *Chem. Sci.*, 2018, **9**, 1273
DOI: 10.1039/C7SC02479G

This article is licensed under a [Creative Commons Attribution 3.0 Unported Licence](#). Material from this article can be used in other publications provided that the correct acknowledgement is given with the reproduced material.

Reproduced material should be attributed as follows:

- For reproduction of material from NJC:
[Original citation] - Published by The Royal Society of Chemistry (RSC) on behalf of the Centre National de la Recherche Scientifique (CNRS) and the RSC.
- For reproduction of material from PCCP:
[Original citation] - Published by the PCCP Owner Societies.
- For reproduction of material from PPS:
[Original citation] - Published by The Royal Society of Chemistry (RSC) on behalf of the European Society for Photobiology, the European Photochemistry Association, and RSC.
- For reproduction of material from all other RSC journals:
[Original citation] - Published by The Royal Society of Chemistry.

Information about reproducing material from RSC articles with different licences is available on our [Permission Requests page](#).

Permission to reproduce “Jenks, T. C.; Bailey, M. D.; Corbin, B. A.; Kuda-Wedagedara, A. N. W.; Martin, P. D.; Schlegel, H. B.; Rabuffetti, F. A.; Allen, M. J. “Photophysical characterization of a highly luminescent divalent-europium-containing azacryptate” *Chem. Commun.* **2018**, *54*, 4545–4548.” for use in Chapter 3:


If you are the author of this article you do not need to formally request permission to reproduce figures, diagrams etc. contained in this article in third party publications or in a thesis or dissertation provided that the correct acknowledgement is given with the reproduced material.

Reproduced material should be attributed as follows:

- For reproduction of material from NJC:
[Original citation] - Reproduced by permission of The Royal Society of Chemistry (RSC) on behalf of the Centre National de la Recherche Scientifique (CNRS) and the RSC
- For reproduction of material from PCCP:
[Original citation] - Reproduced by permission of the PCCP Owner Societies
- For reproduction of material from PPS:
[Original citation] - Reproduced by permission of The Royal Society of Chemistry (RSC) on behalf of the European Society for Photobiology, the European Photochemistry Association, and RSC
- For reproduction of material from all other RSC journals:
[Original citation] - Reproduced by permission of The Royal Society of Chemistry


If you are the author of this article you still need to obtain permission to reproduce the whole article in a third party publication with the exception of reproduction of the whole article in a thesis or dissertation.

Permission to reproduce “Jenks, T. C.; Kuda-Wedagedara, A. N. W.; Bailey, M. D.; Ward, C. L.; Allen, M. J. “Spectroscopic and Electrochemical Trends in Divalent Lanthanides through Modulation of Coordination Environment” *Inorg. Chem.* **2020**, *59*, 2613–2620.” for use in Chapter 4:



RightsLink®

[Home](#)
[Help](#)
[Email Support](#)
[Sign in](#)
[Create Account](#)



Spectroscopic and Electrochemical Trends in Divalent Lanthanides through Modulation of Coordination Environment

Author: Tyler C. Jenks, Akhila N. W. Kuda-Wedagedara, Matthew D. Bailey, et al

Publication: Inorganic Chemistry

Publisher: American Chemical Society

Date: Feb 1, 2020

Copyright © 2020, American Chemical Society

PERMISSION/LICENSE IS GRANTED FOR YOUR ORDER AT NO CHARGE

This type of permission/license, instead of the standard Terms & Conditions, is sent to you because no fee is being charged for your order. Please note the following:

- Permission is granted for your request in both print and electronic formats, and translations.
- If figures and/or tables were requested, they may be adapted or used in part.
- Please print this page for your records and send a copy of it to your publisher/graduate school.
- Appropriate credit for the requested material should be given as follows: "Reprinted (adapted) with permission from (COMPLETE REFERENCE CITATION), Copyright (YEAR) American Chemical Society." Insert appropriate information in place of the capitalized words.
- One-time permission is granted only for the use specified in your request. No additional uses are granted (such as derivative works or other editions). For any other uses, please submit a new request.

BACK
CLOSE WINDOW

© 2020 Copyright - All Rights Reserved | Copyright Clearance Center, Inc. | [Privacy statement](#) | [Terms and Conditions](#)
 Comments? We would like to hear from you. E-mail us at customer-care@copyright.com

REFERENCES

1. MacDonald, M. R.; Bates, J. E.; Ziller, J. W.; Furche, F.; Evans, W. J. "Completing the Series of +2 Ions for the Lanthanide Elements: Synthesis of Molecular Complexes of Pr^{2+} , Gd^{2+} , Tb^{2+} , and Lu^{2+} " *J. Am. Chem. Soc.* **2013**, *135*, 9857–9868.
2. Blasse, G. Chemistry and Physics of R-Activated Phosphors. In *Handbook on the Physics and Chemistry of Rare Earths*. Gschneidner, K. A., Jr., Eyring L., Eds.; North-Holland Publishing Company: Amsterdam, 1979; pp 237–274.
3. Suta, M.; Wickleder, C. "Synthesis, spectroscopic properties and applications of divalent lanthanides apart from Eu^{2+} " *J. Lumin.* **2019**, *210*, 210–238.
4. Sabbatini, N.; Ciano, M.; Dellonte, S.; Bonazzi, A.; Bolletta, F.; Balzani, V. "Photophysical Properties of Europium(II) Cryptates" *J. Phys. Chem.* **1984**, *88*, 1534–1537.
5. Bulgakov, R. G.; Eliseeva, S. M.; Galimov, D. I. "The first registration of a green liquid-phase chemiluminescence of the divalent Eu^{2+} ion in interaction of β -diketonate complexes $\text{Eu}(\text{acac})_3 \cdot \text{H}_2\text{O}$, $\text{Eu}(\text{dpm})_3$, $\text{Eu}(\text{fod})_3$ and $\text{Eu}(\text{CH}_3\text{COO})_3 \cdot 6\text{H}_2\text{O}$ with Bu^i_2AlH in THF with the participation of oxygen" *RSC Adv.* **2015**, *5*, 52132–52140.
6. Bünzli, J.-C. G.; Wessner, D. "Stoichiometry and Structure of the Complexes Between Lanthanide Ions and Macrocyclic Crown Ethers Containing from Four to Seven Coordinating Sites" *Isr. J. Chem.* **1984**, *24*, 313–322.
7. Corbin, B. A.; Hovey, J. L.; Thapa, B.; Schlegel, H. B.; Allen, M. J. "Luminescence differences between two complexes of divalent europium" *J. Organomet. Chem.* **2018**, *857*, 88–93.

8. Jørgensen, C. K. The Nephelauxetic Series. In *Progress in Inorganic Chemistry*. Cotton, F. A., Ed.; Interscience Publishers: New York, 1962; pp 73–124.
9. Jiang, J.; Higashiyama, N.; Machida, K.-i.; Adachi, G.-y. “The luminescent properties of divalent europium complexes of crown ethers and cryptands” *Coord. Chem. Rev.* **1998**, *170*, 1–29.
10. Haas, Y.; Stein, G.; Tomkiewicz, M. “Fluorescence and Photochemistry of the Charge-Transfer Band in Aqueous Europium(III) Solutions” *J. Phys. Chem.* **1970**, *74*, 2558–2562.
11. Ishida, A.; Toki, S.; Takamuku, S. “Photochemical reactions of α -methylstyrene induced by Eu(III)/Eu(III) photoredox system in methanol” *Chem. Lett.* **1985**, 893–896.
12. Maity, S.; Prasad, E. “Photoinduced electron transfer from Eu(II)-complexes to organic molecules: Rate and mechanistic investigation” *J. Photochem. Photobiol. A* **2014**, *274*, 64–72.
13. Jenks, T. C.; Bailey, M. D.; Hovey, J. L.; Fernando, S.; Basnayake, G.; Cross, M. E.; Li, W.; Allen, M. J. “First use of a divalent lanthanide for visible-light-promoted photoredox catalysis” *Chem. Sci.* **2018**, *9*, 1273–1278.
14. Prasad, E.; Knettle, B. W.; Flowers, R. A., II “Photoinduced Electron Transfer Reactions by SmI₂ in THF: Luminescence Quenching Studies and Mechanistic Investigations” *Chem. Eur. J.* **2005**, *11*, 3105–3112.
15. Kuda-Wedagedara, A. N. W.; Wang, C.; Martin, P. D.; Allen, M. J. “Aqueous Eu^{II}-Containing Complex with Bright Yellow Luminescence” *J. Am. Chem. Soc.* **2015**, *137*, 4960–4963.

16. Dorenbos, P. “Energy of the first $4f^7 \rightarrow 4f^6 5d$ transition of Eu^{2+} in inorganic compounds” *J. Lumin.* **2003**, *104*, 239–260.
17. Dorenbos, P. “ $f \rightarrow d$ transition energies of divalent lanthanides in inorganic compounds” *J. Phys.: Condens. Matter* **2003**, *15*, 575–594.
18. Qin, X.; Liu, X.; Huang, W.; Bettinelli, M.; Liu, X. “Lanthanide-Activated Phosphors Based on $4f$ - $5d$ Optical Transitions: Theoretical and Experimental Aspects” *Chem. Rev.* **2017**, *117*, 4488–4527.
19. Bulgakov, R. G.; Kuleshov, S. P.; Makhmutov, A. R.; Kinzyabaeva, Z. S. “Bright blue photoluminescence of Eu^{II} in the complex $\text{EuCl}_2 \cdot 0.5\text{H}_2\text{O} \cdot 0.05(\text{Bu}^i_2\text{Al})_2\text{O}$ ” *Russ. Chem. Bull., Int. Ed.* **2007**, *56*, 570–571.
20. Bulgakov, R. G.; Eliseeva, S. M.; Galimov, D. I. “Peculiarities of bright blue liquid-phase chemiluminescence of the Eu^{2+*} ion generated at interactions in the systems $\text{EuX}_3 \cdot 6\text{H}_2\text{O} - \text{THF} - \text{R}_{3-n}\text{AlH}_n - \text{O}_2$ ($\text{X} = \text{Cl}, \text{NO}_3$; $\text{R} = \text{Bu}^i, \text{Et}$ and Me ; $n = 0, 1$)” *J. Lumin.* **2016**, *172*, 71–82.
21. Adachi, G.-y.; Tomokiyo, K.; Sorita, K.; Shiokawa, J. “Luminescence of Divalent Europium Complexes with Crown Ethers and Polyethylene Glycols” *J. Chem. Soc., Chem Commun.* **1980**, 914–915.
22. Bulgakov, R. G.; Eliseeva, S. M.; Galimov, D. I. “Reduction of Ln^{III} to Ln^{II} in reactions of $\text{LnCl}_3 \cdot 6\text{H}_2\text{O}$ ($\text{Ln} = \text{Eu}, \text{Yb}$, and Sm) with Bu^i_2AlH in THF. The formation of soluble luminescent complexes $\text{LnCl}_2 \cdot x\text{THF}$ ” *Russ. Chem. Bull., Int. Ed.* **2013**, *62*, 2345–2348.
23. Okaue, Y.; Isobe, T. “Characterizations of Divalent Lanthanoid Iodides in Tetrahydrofuran by UV–Vis, Fluorescence and ESR Spectroscopy” *Inorg. Chim. Acta*, **1988**, *144*, 143–146.

24. Dimitriev, O. P.; Kislyuk, V. V. "Green luminescence of the europium chloride:dimethylformamide charge-transfer complex" *Chem. Phys. Lett.* **2003**, 377, 149–155.
25. Bulgakov, R. G.; Eliseeva, S. M.; Galimov, D. I. "The first observation of emission of electronically-excited states of the divalent Eu^{2+*} ion in the new chemiluminescent system $\text{EuCl}_3 \cdot 6\text{H}_2\text{O}-\text{Bu}^i_2\text{AlH}-\text{O}_2$ and the energy transfer from Eu^{2+*} ion to the trivalent ion, Tb^{3+} " *J. Lumin.* **2013**, 136, 95–99.
26. Adachi, G.-y.; Sorita, K.; Kawata, K.; Tomokiyo, K.; Shiokawa, J. "Luminescence of Divalent Europium Complexes with Crown Ethers, Cryptands and Polyethylene Glycols" *J. Less-Common Met.* **1983**, 93, 81–87.
27. Adachi, G.-y.; Fujikawa, H.; Tomokiyo, K.; Sorita, K.; Kawata, K.; Shiokawa, J. "Luminescence Properties of Divalent Europium Complexes with 15-Crown-5 Derivatives" *Inorg. Chim. Acta* **1986**, 113, 87–90.
28. Adachi, G.-y.; Fujikawa, H.; Shiokawa, J. "Luminescence of Divalent Europium Crown Complexes in Various Solvents and at Various Temperatures" *J. Less-Common Met.* **1986**, 126, 147–153.
29. Adachi, G.-y.; Sorita, K.; Kawata, K.; Tomokiyo, K.; Shiokawa, J. "Luminescence of Divalent Europium Complexes with 18-Crown-6 Derivatives" *Inorg. Chim. Acta* **1985**, 109, 117–121.
30. Higashiyama, N.; Takemura, K.; Kimura, K.; Adachi, G.-y. "Luminescence of divalent europium complexes with N-pivot lariat azacrown ethers" *Inorg. Chim. Acta* **1992**, 194, 201–206.

31. Adachi, G.-y.; Sakai, K.; Kawata, K.; Shiokawa, J. ““Photoinduced” Complex Formation” *Inorg. Chem.* **1984**, *23*, 3044–3045.
32. Lenora, C. U.; Staples, R. J.; Allen, M. J. “Measurement of the Dissociation of Eu^{II}-Containing Cryptates Using Murexide” *Inorg. Chem.* **2020**, *59*, 86–93.
33. Lenora, C. U.; Carniato, F.; Shen, Y.; Latif, Z.; Haacke, E. M.; Martin, P. D.; Botta, M.; Allen, M. J. “Structural Features of Eu(II)-Containing Cryptates That Influence Relaxivity” *Chem. Eur. J.* **2017**, *23*, 15404–15414.
34. Shinoda, S.; Nishioka, M.; Tsukube, H. “*In situ* generation of fluorescent macrocyclic europium(II) complexes via zinc reduction” *J. Alloys. Compd.* **2009**, *488*, 603–605.
35. Jin, G.-X.; Bailey, M. D.; Allen, M. J. “Unique Eu^{II} Coordination Environments with a Janus Cryptand” *Inorg. Chem.* **2016**, *55*, 9085–9090.
36. Jenks, T. C.; Bailey, M. D.; Corbin, B. A.; Kuda-Wedagedara, A. N. W.; Martin, P. D.; Schlegel, H. B.; Rabuffetti, F. A.; Allen, M. J. “Photophysical characterization of a highly luminescent divalent-europium-containing azacryptate” *Chem. Commun.* **2018**, *54*, 4545–4548.
37. Kelly, R. P.; Bell, T. D. M.; Cox, R. P.; Daniels, D. P.; Deacon, G. B.; Jaroschik, F.; Junk, P. C.; Le Goff, X. F.; Lemercier, G.; Martinez, A.; Wang, J.; Werner, D. “Divalent Tetra- and Penta-phenylcyclopentadienyl Europium and Samarium Sandwich and Half-Sandwich Complexes: Synthesis, Characterization, and Remarkable Luminescence Properties” *Organometallics* **2015**, *34*, 5624–5636.
38. Thomas, A. C.; Ellis, A. B. “Diethyl Ether Adducts of Bis(pentamethylcyclopentadienyl)europium(II) and -ytterbium(II): Excited-State Energy Transfer with Organolanthanoid Complexes” *Organometallics* **1985**, *4*, 2223–2225.

39. Tsuji, T.; Fukazawa, S.; Sugiyama, R.; Kawasaki, K.; Iwasa, T.; Tsunoyama, H.; Tokitoh, N.; Nakajima, A. "Physical properties of mononuclear organoeuropium sandwich complexes ligated by cyclooctatetraene and bis(trimethylsilyl)cyclooctatetraene" *Chem. Phys. Lett.* **2014**, 595–596, 144–150.
40. Kawasaki, K.; Sugiyama, R.; Tsuji, T.; Iwasa, T.; Tsunoyama, H.; Mizuhata, Y.; Tokitoh, N.; Nakajima, A. "A designer ligand field for blue-green luminescence of organoeuropium(II) sandwich complexes with cyclononatetraenyl ligands" *Chem. Commun.* **2017**, 53, 6557–6560.
41. Summerscales, O. T.; Jones, S. C.; Cloke, G. N.; Hitchcock, P. B. "Anti-Bimetallic Complexes of Divalent Lanthanides with Silylated Pentalene and Cyclooctatetraenyl Bridging Ligands as Molecular Models for Lanthanide-Based Polymers" *Organometallics* **2009**, 28, 5896–5908.
42. Kühling, M.; Wickleder, C.; Ferguson, M. J.; Hrib, C. G.; McDonald, R.; Suta, M.; Hilfert, L.; Takats, J.; Edelmann, F. T. "Investigation of the "bent sandwich-like" divalent lanthanide hydro-tris(pyrazolyl)borates $\text{Ln}(\text{Tp}^{\text{iPr}_2})_2$ (Ln = Sm, Eu, Tm, Yb)" *New J. Chem.* **2015**, 39, 7617–7625.
43. Kuzyaev, D. M.; Rumyanstev, R. V.; Fukin, G. K.; Bochkarev, M. N. "Hexafluoroisopropoxides of divalent and trivalent lanthanides. Structures and luminescent properties" *Russ. Chem. Bull., Int. Ed.* **2014**, 63, 848–853.
44. Kuzyaev, D. M.; Balashova, T. V.; Burin, M. E.; Fukin, G. K.; Romyantsev, R. V.; Pushkarev, A. P.; Ilichev, V. A.; Grishin, I. D.; Vorozhtsov, D. L.; Bochkarev, M. N. "Synthesis, structure and luminescent properties of lanthanide fluoroalkoxides" *Dalton Trans.* **2016**, 45, 3464–3472.

45. Goodwin, C. A. P.; Chilton, N. F.; Natrajan L. S.; Boulon, M.-E.; Ziller, J. W.; Evans, W. J.; Mills, D. P. "Investigation into the Effects of a Trigonal-Planar Ligand Field on the Electronic Properties of Lanthanide(II) Tris(silylamide) Complexes (Ln = Sm, Eu, Tm, Yb)" *Inorg. Chem.* **2017**, *56*, 5959–5970.
46. Li, W.; Fujikawa, H.; Adachi, G.-y.; Shiokawa, J. "Absorption and Emission Properties of Divalent Ytterbium Crown Ether Complexes" *Inorg. Chim. Acta* **1986**, *117*, 87–89.
47. Jenks, T. C.; Kuda-Wedagedara, A. N. W.; Bailey, M. D.; Ward, C. L.; Allen, M. J. "Spectroscopic and Electrochemical Trends in Divalent Lanthanides through Modulation of Coordination Environment" *Inorg. Chem.* **2020**, *59*, 2613–2620.
48. Thomas, A. C.; Ellis, A. B. "Chemiluminescent Reactions of Bis(η^5 -pentamethylcyclopentadienyl)ytterbium Derivatives" *J. Chem. Soc., Chem. Commun.* **1984**, 1270–1271.
49. Ellis, A. B.; Thomas, A. C.; Schlesener, C. J. "Excited-State Properties of Cyclopentadienylytterbium Complexes" *Inorg. Chim. Acta* **1984**, *94*, 20–21.
50. Skene, W. G.; Scaiano, J. C.; Cozens, F. L. "Fluorescence from Samarium(II) Iodide and Its Electron Transfer Quenching: Dynamics of the Reaction of Benzyl Radicals with Sm(II)" *J. Org. Chem.* **1996**, *61*, 7918–7921.
51. Bulgakov, R. G.; Eliseeva, S. M.; Galimov, D. I. "The first example of generation and emission of divalent Sm^{2+*} ion in a liquid-phase chemiluminescence in the system SmCl₃ · 6H₂O–THF–Buⁱ₂AlH–O₂" *J. Photochem. Photobiol. A* **2015**, *300*, 1–5.
52. Teprovich, J. A., Jr.; Prasad, E.; Flowers, R. A., II "Solvation-Controlled Luminescence of SmII Complexes" *Angew. Chem. Int. Ed.* **2007**, *46*, 1145–1148.

53. Amador A. G.; Yoon T. P. “A Chiral Metal Photocatalyst Architecture for Highly Enantioselective Photoreactions” *Angew. Chem., Int. Ed.* **2016**, *55*, 2304–2306.
54. Shaw, M. H.; Twilton, J.; MacMillan, D. W. C. “Photoredox in Organic Chemistry” *J. Org. Chem.* **2016**, *81*, 6898–6926.
55. Slutskyy, Y.; Overman, L. E. “Generation of the Methoxycarbonyl Radical by Visible-Light Photoredox Catalysis and Its Conjugate Addition with Electron-Deficient Olefins” *Org. Lett.* **2016**, *18*, 2564–2567.
56. Singh, A.; Fennell, C. J.; Weaver, J. D. “Photocatalyst Size Controls Electron and Energy Transfer: Selectable *E/Z* Isomer Synthesis via C–F Alkenylation” *Chem. Sci.* **2016**, *7*, 6796–6802.
57. Douglas, J. J.; Sevrin, M. J.; Stephenson, C. R. J. “Visible Light Photocatalysis: Applications and New Disconnections in the Synthesis of Pharmaceutical Agents” *Org. Process Res. Dev.* **2016**, *20*, 1134–1147.
58. Terrett, J. A.; Cuthbertson, J. D.; Shurtleff, V. W.; MacMillan, D. W. C. “Switching On Elusive Organometallic Mechanisms with Photoredox Catalysis” *Nature* **2015**, *524*, 330–334.
59. Nawrat, C. C.; Jamison, C. R.; Slutskyy, Y.; MacMillan, D. W. C.; Overman, L. E. “Oxalates as Activating Groups for Alcohols in Visible Light Photoredox Catalysis: Formation of Quaternary Centers by Redox-Neutral Fragment Coupling” *J. Am. Chem. Soc.* **2015**, *135*, 11270–11273.
60. Arora, A.; Teegardin, K. A.; Weaver, J. D. “Reductive Alkylation of 2-Bromoazoles via Photoinduced Electron Transfer: A Versatile Strategy to Csp^2 – Csp^3 Coupled Products” *Org. Lett.* **2015**, *17*, 3722–3725.

61. Tellis, J. C.; Primer, D. N.; Molander, G. A. "Single-Electron Transmetalation in Organoboron Cross-Coupling by Photoredox/Nickel Dual Catalysis" *Science* **2014**, *345*, 433–436.
62. Singh, K.; Staig, S. J.; Weaver, J. D. "Facile Synthesis of Z-Alkenes via Uphill Catalysis" *J. Am. Chem. Soc.* **2014**, *136*, 5275–5278.
63. Bergonzini, G.; Schindler, C. S.; Wallentin, C.-J.; Jacobsen, E. N.; Stephenson, C. R. J. "Photoredox Activation and Anion Binding Catalysis in the Dual Catalytic Enantioselective Synthesis of β -Amino Esters" *Chem. Sci.* **2014**, *5*, 112–116.
64. Xi, Y.; Yi, H.; Lei, A. "Synthetic Applications of Photoredox Catalysis with Visible Light" *Org. Biomol. Chem.* **2013**, *11*, 2387–2403.
65. Narayanam, J. M. R.; Stephenson, C. R. J. "Visible Light Photoredox Catalysis: Applications in Organic Synthesis" *Chem. Soc. Rev.* **2011**, *40*, 102–113.
66. Yoon, T. P.; Ischay, M. A.; Du, J. "Visible Light Photocatalysis as a Greener Approach to Photochemical Synthesis" *Nat. Chem.* **2010**, *2*, 527–532.
67. Welin, E. R.; Le, C.; Arias-Rotondo, D. M.; McCusker, J. K.; MacMillan, D. W. C. "Photosensitized, Energy-Transfer Mediated Organometallic Catalysis Through Electronically Excited Nickel(II)" *Science* **2017**, *355*, 380–385.
68. Sattler, W.; Henling, L. M.; Winkler, J. R.; Gray, H. B. "Bespoke Photoreductants: Tungsten Arylisocyanides" *J. Am. Chem. Soc.* **2015**, *137*, 1198–1205.
69. Harkins, S. B.; Peters, J. C. "A Highly Emissive Cu_2N_2 Diamond Core Complex Supported by a $[\text{PNP}]^-$ Ligand" *J. Am. Chem. Soc.* **2005**, *127*, 2030–2031.

70. Huo, H.; Harms, K.; Meggers, E. "Catalytic, Enantioselective Addition of Alkyl Radicals to Alkenes via Visible-Light-Activated Photoredox Catalysis with a Chiral Rhodium Complex" *J. Am. Chem. Soc.* **2016**, *138*, 6936–6939.
71. Büldt, L. A.; Guo, X.; Prescimone, A.; Wenger, O. S. "A Molybdenum(0) Isocyanide Analogue of Ru(2,2'-Bipyridine)₃²⁺: A Strong Reductant for Photoredox Catalysis" *Angew. Chem., Int. Ed.* **2016**, *55*, 11247–11250.
72. Li, D.; Che, C.-M.; Kwong, H.-L.; Yam, V. W.-W. "Photoinduced C–C Bond Formation From Alkyl Halides Catalysed by Luminescent Dinuclear Gold(I) and Copper(I) Complexes" *J. Chem. Soc., Dalton Trans.* **1992**, *23*, 3325–3329.
73. Creutz, S. E.; Lotito, K. J.; Fu, G. C.; Peters, J. C. "Photoinduced Ullman C–N Coupling: Demonstrating the Viability of a Radical Pathway" *Science* **2012**, *338*, 647–651.
74. Sattler, W.; Ener, M. E.; Blakemore, J. D.; Rachford, A. A.; LaBeaume, P. J.; Thackeray, J. W.; Cameron, J. F.; Winkler, J. R.; Gray, H. B. "Generation of Powerful Tungsten Reductants by Visible Light Excitation" *J. Am. Chem. Soc.* **2013**, *135*, 10614–10617.
75. Kern, J.-M.; Sauvage, J.-P. "Photoassisted C–C Coupling via Electron Transfer to Benzylic Aldehydes by a Bis(di-imine) Copper(I) Complex" *J. Chem. Soc., Chem. Commun.* **1987**, *8*, 546–548.
76. Yin, H.; Carroll, P. J.; Anna, J. M.; Schelter, E. J. "Luminescent Ce(III) Complexes as Stoichiometric and Catalytic Photoreductants for Halogen Atom Abstraction Reactions" *J. Am. Chem. Soc.* **2015**, *137*, 9234–9237.
77. Yin, H.; Carroll, P. J.; Manor, B. C.; Anna, J. M.; Schelter, E. J. "Cerium Photosensitizers: Structure–Function Relationships and Applications in Photocatalytic Aryl Coupling Reactions" *J. Am. Chem. Soc.* **2016**, *138*, 5984–5993.

78. Yin, H.; Jin, Y.; Hertzog, J. E.; Mullane, K. C.; Carroll, P. J.; Manor, B. C.; Anna, J. M.; Schelter, E. J. "The Hexachlorocerate(III) Anion: A Potent, Benchtop Stable, and Readily Available Ultraviolet A Photosensitizer for Aryl Chlorides" *J. Am. Chem. Soc.* **2016**, *138*, 16266–16273.
79. Suzuki, K.; Tang, F.; Kikukawa, Y.; Yamaguchi, K.; Mizuno, N. "Visible-Light-Induced Photoredox Catalysis with a Tetracerium-Containing Silicotungstate" *Angew. Chem., Int. Ed.* **2014**, *53*, 5356–5360.
80. Guo, J.-J.; Hu, A.; Chen, Y.; Sun, J.; Tang, H.; Zuo, Z. "Photocatalytic C–C Bond Cleavage and Amination of Cycloalkanols by Cerium(III) Chloride Complex" *Angew. Chem., Int. Ed.* **2016**, *55*, 15319–15322.
81. Nicolaou, K. C.; Ellery, S. P.; Chen, J. S. "Samarium Diiodide Mediated Reactions in Total Synthesis" *Angew. Chem., Int. Ed.* **2009**, *48*, 7140–7165.
82. Ogawa, A.; Sumino, Y.; Nanke, T.; Ohya, S.; Sonoda, N.; Hirao, T. "Photoinduced Reduction and Carbonylation of Organic Chlorides with Samarium Diiodide" *J. Am. Chem. Soc.* **1997**, *119*, 2745–2746.
83. Molander, G. A.; Wolfe, C. N. "Intramolecular Ketone–Nitrile Reductive Coupling Reactions Promoted by Samarium(II) Iodide" *J. Org. Chem.* **1998**, *63*, 9031–9036.
84. Molander, G. A.; Alonso-Alija, C. "Sequenced Reactions with Samarium(II) Iodide. Sequential Intermolecular Carbonyl Addition/Intramolecular Nucleophilic Acyl Substitution for the Preparation of Seven-, Eight-, and Nine-Membered Carbocycles" *J. Org. Chem.* **1998**, *63*, 4366–4373.
85. Rao, C. N.; Hoz, S. "Photostimulated Reduction of Nitriles by SmI₂" *J. Org. Chem.* **2012**, *77*, 4029–4034.

86. Rao, C. N.; Hoz, S. "Synergism and Inhibition in the Combination of Visible Light and HMPA in SmI₂ Reductions" *J. Org. Chem.* **2012**, *77*, 9199–9204.
87. Sumino, Y.; Harato, N.; Tomisaka, Y.; Ogawa, A. "A Novel Photoinduced Reduction System of Low-Valent Samarium Species: Reduction of Organic Halides and Chalcogenides, and Its Application to Carbonylation with Carbon Monoxide" *Tetrahedron* **2003**, *59*, 10499–10508.
88. Maity, S.; Choquette, K. A.; Flowers, R. A., II; Prasad, E. "Effect of Crown Ethers on the Ground and Excited State Reactivity of Samarium Diiodide in Acetonitrile" *J. Phys. Chem. A* **2012**, *116*, 2154–2160.
89. Nomoto, A.; Kojo, Y.; Shiino, G.; Tomisaka, Y.; Mitani, I.; Tatsumi, M.; Ogawa, A. "Reductive carboxylation of alkyl halides with CO₂ by use of photoinduced SmI₂/Sm reduction system" *Tetrahedron Lett.* **2010**, *51*, 6580–6583.
90. Tomisaka, Y.; Nomoto, A.; Ogawa, A. "On the Potentially Excellent Reducing Ability of a Series of Low-Valent Rare Earths Induced by Photoirradiation" *Tetrahedron Lett.* **2009**, *50*, 584–586.
91. Watson, P. L.; Tulip, T. H.; Williams, I. "Defluorination of Perfluoroolefins by Divalent Lanthanoid Reagents: Activating Carbon–Fluorine Bonds" *Organometallics* **1990**, *9*, 1999–2009.
92. Neumann, M.; Zeitler, K. "Application of Microflow Conditions to Visible Light Photoredox Catalysis" *Org. Lett.* **2012**, *14*, 2658–2661.
93. Wang, Z. J.; Ghasimi, S.; Landfester, K.; Zhang, K. A. I. "A Conjugated Porous Poly-Benzobisthiadiazole Network for a Visible Light-Driven Photoredox Reaction" *J. Mater. Chem. A* **2014**, *2*, 18720–18724.

94. Smith, P. H.; Barr, M. E.; Brainard, J. R.; Ford, D. K.; Freiser, H.; Muralidharan, S.; Reilly, S. D.; Ryan, R. R.; Silks, L. A., III; Yu, W.-h. "Synthesis and Characterization of Two Nitrogen-Donor Cryptands" *J. Org. Chem.* **1993**, *58*, 7939–7941.
95. Redko, M. Y.; Huang, R.; Dye, J. L.; Jackson, J. E. "One-Pot Synthesis of 1,4,7,10,13,16,21,24-Octaazabicyclo[8.8.8]hexacosane – The Peraza Analogue of [2.2.2]Cryptand" *Synthesis* **2006**, 759–761.
96. Prier, C. K.; Rankic, D. A.; MacMillan, D. W. C. "Visible Light Photoredox Catalysis with Transition Metal Complexes: Applications in Organic Synthesis" *Chem. Rev.* **2013**, *113*, 5322–5363.
97. Hazin, P. N.; Bruno, J. W.; Brittain, H. G. "Luminescence Spectra of a Series of Cerium(III) Halides and Organometallics. Probes of Bonding Properties Using 4f–5d Excited States" *Organometallics* **1987**, *6*, 913–918.
98. Raehm, L.; Mehdi, A.; Wickleder, C.; Reyé, C.; Corriu, R. J. P. "Unexpected Coordination Chemistry of Bisphenanthroline Complexes Within Hybrid Materials: A Mild Way to Eu²⁺ Containing Materials with Bright Yellow Luminescence" *J. Am. Chem. Soc.* **2007**, *129*, 12636–12637.
99. Tucker, J. W.; Stephenson, C. R. J. "Shining Light on Photoredox Catalysis: Theory and Synthetic Applications" *J. Org. Chem.* **2012**, *77*, 1617–1622.
100. Rehm, D.; Weller, A. "Kinetics of Fluorescence Quenching by Electron and H-Atom Transfer" *Isr. J. Chem.* **1970**, *8*, 259–271.
101. Seibig, S.; Tóth, É.; Merbach, A. E. "Unexpected Differences in the Dynamics and in the Nuclear and Electronic Relaxation Properties of the Isoelectronic

- [Eu^{II}(DTPA)(H₂O)]³⁻ and [Gd^{III}(DTPA)(H₂O)]²⁻ Complexes (DTPA = Diethylenetriamine Pentaacetate)” *J. Am. Chem. Soc.* **2000**, *122*, 5822–5830.
102. Burai, L.; Tóth, É.; Seibig, S.; Scopelliti, R.; Merbach, A. E. “Solution and Solid-State Characterization of Eu^{II} Chelates: A Possible Route Towards Redox Responsive MRI Contrast Agents” *Chem.–Eur. J.* **2000**, *6*, 3761–3770.
103. Regueiro-Figueroa, M.; Barriada, J. L.; Pallier, A.; Esteban-Gómez, D.; de Blas, A.; Rodríguez-Blas, T.; Tóth, É.; Platas-Iglesias, C. “Stabilizing Divalent Europium in Aqueous Solution Using Size-Discrimination and Electrostatic Effects” *Inorg. Chem.* **2015**, *54*, 4940–4952.
104. Ekanger, L. A.; Mills, D. R.; Ali, M. M.; Polin, L. A.; Shen, Y.; Haacke, E. M.; Allen, M. J. “Spectroscopic Characterization of the 3+ and 2+ Oxidation States of Europium in a Macrocyclic Tetraglycinate Complex” *Inorg. Chem.* **2016**, *55*, 9981–9988.
105. Flowers, R. A., II “Mechanistic Studies on the Roles of Cosolvents and Additives in Samarium(II)-Based Reductions” *Synlett* **2008**, *10*, 1427–1439.
106. Yields are reported as the mean ± standard error of the mean of three independently prepared reactions.
107. Lakowicz, J. R. *Principles of Fluorescence Spectroscopy*, 3rd Edition; Springer Science: New York, 2006; pp 278–327.
108. Averill, D. J.; Allen, M. J. “Synthesis, Spectroscopic Characterization, and Reactivity of Water-Tolerant Eu³⁺-Based Precatalysts” *Inorg. Chem.* **2014**, *53*, 6257–6263.
109. de Bettencourt-Dias, A. Introduction to Lanthanide Ion Luminescence. In *Luminescence of Lanthanide Ions in Coordination Compounds and Nanomaterials*, de Bettencourt-Dias, A., Ed.; John Wiley and Sons: West Sussex, 2014; pp 1–48.

110. Zhang, Z.; Xu, B.; Su, J.; Shen, L.; Xie, Y.; Tian, H. “Color-Tunable Solid-State Emission of 2,2'-Biindenyl-Based Fluorophores” *Angew. Chem., Int. Ed.* **2011**, *50*, 11654–11657.
111. Sagara, Y.; Kato, T. “Brightly Tricolored Mechanochromic Luminescence from a Single-Luminophore Liquid Crystal: Reversible Writing and Erasing of Images” *Angew. Chem.* **2011**, *123*, 9156–9156.
112. Kang, J. H.; Kim, J. Y.; Jeon, D. Y. “Synthesis and Characterization of Orange-Emitting SnO₂:Eu³⁺ Phosphor by an Optimized Combustion Method” *J. Electrochem. Soc.* **2005**, *152*, H33–H38.
113. Sun, T.; Chen, X.; Jin, L.; Li, H.-W.; Chen, B.; Fan, B.; Moine, B.; Qiao, X.; Fan, X.; Tsang, S.-W.; Yu, S. F.; Wang, F. “Broadband Ce(III)-Sensitized Quantum Cutting in Core–Shell Nanoparticles: Mechanistic Investigation and Photovoltaic Application” *J. Phys. Chem. Lett.* **2017**, *8*, 5099–5104.
114. de Bettencourt-Dias, A.; Rossini, J. S. K. “Ligand Design for Luminescent Lanthanide-Containing Metallopolymers” *Inorg. Chem.* **2016**, *55*, 9954–9963.
115. Wei, Y.; Li, Q.; Sa, R.; Wu, K. “A White-Light-Emitting LnMOF with Color Properties Improved via Eu³⁺ Doping: An Alternative Approach to a Rational Design for Solid-State Lighting” *Chem. Commun.* **2014**, *50*, 1820–1823.
116. Singh, K.; Boddula, R.; Vaidyanathan, S. “Versatile Luminescent Europium(III)- β -Diketonate-Imidazo-Bipyridyl Complexes Intended for White LEDs: A Detailed Photophysical and Theoretical Study” *Inorg. Chem.* **2017**, *56*, 9376–9390.

117. Wu, W.; Xia, Z. “Synthesis and Color-Tunable Luminescence Properties of Eu^{2+} and Mn^{2+} -Activated $\text{Ca}_3\text{Mg}_3(\text{PO}_4)_4$ Phosphor for Solid State Lighting” *RSC Adv.* **2013**, *3*, 6051–6057.
118. Yu, R.; Noh, H. M.; Moon, B. K.; Choi, B. C.; Jeong, J. H.; Jang, K.; Yi, S. S.; Jang, J. K. “Synthesis and Luminescence Properties of a Novel Red-Emitting Phosphor $\text{Ba}_3\text{La}(\text{PO}_4)_3:\text{Eu}^{3+}$ for Solid-State Lighting” *J. Alloys Compd.* **2013**, *576*, 236–241.
119. Setlur, A. A.; Heward, W. J.; Gao, Y.; Srivastava, A. M.; Chandran, R. G.; Shankar, M. V. “Crystal Chemistry and Luminescence of Ce^{3+} -Doped $\text{Lu}_2\text{CaMg}_2(\text{Si,Ge})_3\text{O}_{12}$ and Its Use in LED Based Lighting” *Chem. Mater.* **2006**, *18*, 3314–3322.
120. Liu, J.; Bu, J.; Bu, W.; Zhang, S.; Pan, L.; Fan, W.; Chen, F.; Zhou, L.; Peng, W.; Zhao, K.; Du, J.; Shi, J. “Real-Time In Vivo Quantitative Monitoring of Drug Release by Dual-Mode Magnetic Resonance and Upconverted Luminescence Imaging” *Angew. Chem., Int. Ed.* **2014**, *53*, 4551–4555.
121. Hanaoka, K.; Kikuchi, K.; Kobayashi, S.; Nagano, T. “Time-Resolved Long-Lived Luminescence Imaging Method Employing Luminescent Lanthanide Probes with a New Microscopy System” *J. Am. Chem. Soc.* **2007**, *129*, 13502–13509.
122. Debroye, E.; Parac-Vogt, T. N. “Towards Polymetallic Lanthanide Complexes as Dual Contrast Agents for Magnetic Resonance and Optical Imaging” *Chem. Soc. Rev.* **2014**, *43*, 8178–8192.
123. Jin, M.; Sumitani, T.; Sato, H.; Seki, T.; Ito, H. “Mechanical-Stimulation-Triggered and Solvent-Vapor-Induced Reverse Single-Crystal-to-Single-Crystal Phase Transitions with Alterations of the Luminescence Color” *J. Am. Chem. Soc.* **2018**, *140*, 2875–2879.

124. Zhang, K. Y.; Yu, Q.; Wei, H.; Liu, S.; Zhao, Q.; Huang, W. “Long-Lived Emissive Probes for Time-Resolved Photoluminescence Bioimaging and Biosensing” *Chem. Rev.* **2018**, *118*, 1770–1839.
125. Bradberry, S. J.; Savyasachi, A. J.; Martinez-Calvo, M.; Gunnlaugsson, T. “Development of Responsive Visibly and NIR Luminescent and Supramolecular Coordination Self-Assemblies Using Lanthanide Ion Directed Synthesis” *Coord. Chem. Rev.* **2014**, *273–274*, 226–241.
126. Eliseeva, S. V.; Bünzli, J.-C. G. “Lanthanide Luminescence for Functional Materials and Bio-Sciences” *Chem. Soc. Rev.* **2010**, *39*, 189–227.
127. Rosa, I. L. V.; Tavares, F. A.; deMoura, A. P.; Pinatti, I. M.; da Silva, L. F.; Li, M. S.; Longo, E. “Luminescent and Gas Sensor Properties of the $\text{ZrO}_2\text{:Hhpa:Eu}^{3+}$ Hybrid Compound” *J. Lumin.* **2018**, *197*, 38–46.
128. Moore, J. D.; Lord, R. L.; Cisneros, G. A.; Allen, M. J. “Concentration-Independent pH Detection with a Luminescent Dimetallic Eu(III)-Based Probe” *J. Am. Chem. Soc.* **2012**, *134*, 17372–17375.
129. Liu, T.; Nonat, A.; Beyler, M.; Regueiro-Figueroa, M.; Nono, K. N.; Jeannin, O.; Camerel, F.; Debaene, F.; Cianférani-Sanglier, S.; Tripier, R.; Platas-Iglesias, C.; Charbonnière, L. J. “Supramolecular Luminescent Lanthanide Dimers for Fluoride Sequestering and Sensing” *Angew. Chem., Int. Ed.* **2014**, *53*, 7259–7263.
130. Devery, J. J., III; Nguyen, J. D.; Dai, C.; Stephenson, C. R. J. “Light-Mediated Reductive Debromination of Unactivated Alkyl and Aryl Bromides” *ACS Catal.* **2016**, *6*, 5962–5967.

131. Nicewicz, D. A.; MacMillan, D. W. C. “Merging Photoredox Catalysis with Organocatalysis: The Direct Asymmetric Alkylation of Aldehydes” *Science* **2008**, *322*, 77–80.
132. Devery, J. J., III; Douglas, J. J.; Nguyen, J. D.; Cole, K. P.; Flowers, R. A., II; Stephenson, C. R. J. “Ligand Functionalization as a Deactivation Pathway in a *fac*-Ir(ppy)₃-Mediated Radical Addition” *Chem. Sci.* **2015**, *6*, 537–541.
133. Dissanayake, P.; Allen, M. J. “Dynamic Measurements of Aqueous Lanthanide Triflate-Catalyzed Reactions Using Luminescence Decay” *J. Am. Chem. Soc.* **2009**, *131*, 6342–6343.
134. Dissanayake, P.; Mei, Y.; Allen, M. J. “Luminescence-Decay as an Easy-to-Use Tool for the Study of Lanthanide-Containing Catalysts in Aqueous Solutions” *ACS Catal.* **2011**, *1*, 1203–1212.
135. Farrell, D.; Harding, C. J.; McKee, V.; Nelson, J. “Effect of Methylation on the Coordination of Copper by Small Azacryptands; The Role of Geometrically Constrained Hydrogen Bonding in Stabilizing Terminally Coordinated Oxygen Species” *Dalton Trans.* **2006**, 3204–3211.
136. Basal, L. A.; Bailey, M. D.; Romero, J.; Ali, M. M.; Kurenbekova, L.; Yustein, J.; Pautler, R. G.; Allen, M. J. “Fluorinated Eu^{II}-based multimodal contrast agent for temperature- and redox-responsive magnetic resonance imaging” *Chem. Sci.* **2017**, *8*, 8345–8350.
137. Müller-Buschbaum, K.; Mokaddem, Y.; Schappacher, F. M.; Pöttgen, R. “ ∞^3 [Eu(Tzpy)₂]: A Homoleptic Framework Containing {Eu^{II}N₁₂} Icosahedra” *Angew. Chem., Int. Ed.* **2007**, *46*, 4385–4387.

138. Ekanger, L. A.; Polin, L. A.; Shen, Y.; Haacke, E. M.; Martin, P. D.; Allen, M. J. “A Eu^{II}-Containing Cryptate as a Redox Sensor in Magnetic Resonance Imaging of Living Tissue” *Angew. Chem. Int. Ed.* **2015**, *54*, 14398–14401.
139. Huh, D. N.; Kotyk, C. M.; Gembicky, M.; Rheingold, A. L.; Ziller, J. W.; Evans, W. J. “Synthesis of rare-earth-metal-in-cryptand dications, [Ln(2.2.2-cryptand)]²⁺, from Sm²⁺, Eu²⁺, and Yb²⁺ silyl metallocenes (C₅H₄SiMe₃)₂Ln(THF)₂” *Chem. Commun.* **2017**, *53*, 8664–8666.
140. Wang, D.; Zhao, C.; Phillips, D. L. “A Theoretical Study of Divalent Lanthanide (Sm and Yb) Complexes with a Triazacyclononane-Functionalized Tetramethylcyclopentadienyl Ligand” *Organometallics* **2004**, *23*, 1953–1960.
141. Scalmani, G.; Frisch, M. J.; Mennucci, B.; Tomasi, J.; Cammi, R.; Barone, V. “Geometries and Properties of Excited States in the Gas Phase and in Solution: Theory and Application of a Time-Dependent Density Functional Theory Polarizable Continuum Model” *J. Chem. Phys.* **2006**, *124*, 1–15.
142. Furche, F.; Ahlrichs, R. “Adiabatic Time-Dependent Density Functional Methods for Excited State Properties” *J. Chem. Phys.* **2002**, *117*, 7433–7447.
143. Stratmann, R. E.; Scuseria, G. E.; Frisch, M. J. “An Efficient Implementation of Time-Dependent Density-Functional Theory for the Calculation of Excitation Energies of Large Molecules” *J. Chem. Phys.* **1998**, *109*, 8218–8224.
144. Becke, A. D. “Becke’s Three Parameter Hybrid Method Using the LYP Correlation Functional” *J. Chem. Phys.* **1993**, *98*, 5648.
145. Perdew, J. P. “Density-Functional Approximation for the Correlation Energy of the Inhomogeneous Electron Gas” *Phys. Rev. B* **1986**, *33*, 8822–8824.

146. Zhao, Y.; Rabouw, F. T.; van Puffelen, T.; van Walree, C. A.; Gamelin, D. R.; de Mello Donegá, C.; Meijerink, A. “Lanthanide-Doped CaS and SrS Luminescent Nanocrystals: A Single-Source Precursor Approach for Doping” *J. Am. Chem. Soc.* **2014**, *136*, 16533–16543.
147. Rybak, J.-C.; Hailmann, M.; Matthes, P. R.; Zurawski, A.; Nitsch, J.; Steffen, A.; Heck, J. G.; Feldmann, C.; Götzendörfer, S.; Meinhardt, J.; Sextl, G.; Kohlmann, H.; Sedlmaier, S. J.; Schnick, W.; Müller-Buschbaum, K. “Metal–Organic Framework Luminescence in the Yellow Gap by Codoping of the Homoleptic Imidizolate $^3[\text{Ba}(\text{Im})_2]$ with Divalent Europium” *J. Am. Chem. Soc.* **2013**, *135*, 6896–6902.
148. Marks, S.; Heck, J. G.; Habicht, M. H.; Oña-Burgos, P.; Feldmann, C.; Roesky, P. W. “[Ln(BH₄)₂(THF)₂] (Ln = Eu, Yb)—A Highly Luminescent Material. Synthesis, Properties, Reactivity, and NMR Studies” *J. Am. Chem. Soc.* **2012**, *134*, 16983–16986.
149. Kunkel, N.; Kohlmann, H.; Sayede, A.; Springborg, M. “Alkaline-Earth Metal Hydrides as Novel Host Lattices for Eu^{II} Luminescence” *Inorg. Chem.* **2011**, *50*, 5873–5875.
150. Edgar, A.; Varoy, C. R.; Koughia, C.; Tonchev, D.; Belev, G.; Okada, G.; Kasap, S. O.; von Seggern, H.; Ryan, M. “Optical properties of divalent samarium-doped fluorochlorozirconate glasses and glass ceramics” *Opt. Mater.* **2009**, *31*, 1459–1466.
151. Chciuk, T. V.; Flowers, R. A., II “Proton-Coupled Electron Transfer in the Reduction of Arenes by SmI₂–Water Complexes” *J. Am. Chem. Soc.* **2015**, *137*, 11526–11531.
152. Chopade, P. R.; Davis, T. A.; Prasad, E.; Flowers, R. A., II “Solvent-Dependent Diastereoselectivities in Reductions of β -Hydroxyketones by SmI₂” *Org. Lett.* **2004**, *6*, 2685–2688.

153. Shabangi, M.; Flowers, R. A., II “Electrochemical Investigation of the Reducing Power of SmI₂ in THF and the Effect of HMPA Cosolvent” *Tetrahedron Lett.* **1997**, *38*, 1137–1140.
154. Selikhov, A. N.; Plankin, G. S.; Cherkasov, A. V.; Shavyrin, A. S.; Louyriac, E.; Maron, L.; Trifonov, A. A. “Thermally Stable Ln(II) and Ca(II) Bis(benzhydryl) Complexes: Excellent Precatalysts for Intermolecular Hydrophosphination of C–C Multiple Bonds” *Inorg. Chem.* **2019**, *58*, 5325–5334.
155. Sun, L.; Sahloul, K.; Mellah, M. “Use of Electrochemistry to Provide Efficient SmI₂ Catalytic System for Coupling Reactions.” *ACS Catal.* **2013**, *3*, 2568–2573.
156. Kondo, T.; Akazome, M.; Watanabe, Y. “Lanthanide(II) Iodide Catalysed Photochemical Allylation of Aldehydes with Allylic Halides” *J. Chem. Soc., Chem. Commun.* **1991**, 757–758.
157. Meyer, A. U.; Slanina, T.; Heckel, A.; König, B. “Lanthanide Ions Coupled with Photoinduced Electron Transfer Generate Strong Reduction Potentials from Visible Light” *Chem. Eur. J.* **2017**, *23*, 7900–7904.
158. Zhu, Z.; Wang, C.; Xiang, X.; Pi, C.; Zhou, X. “DyI₂ initiated mild and highly selective silyl radical-catalyzed cyclotrimerization of terminal alkynes and polymerization of MMA” *Chem. Commun.* **2006**, 2066–2068.
159. Maldiney, T.; Lecointre, A.; Viana, B.; Bessière, A.; Bessodes, M.; Gourier, D.; Richard, C.; Scherman, D. “Controlling Electron Trap Depth to Enhance Optical Properties of Persistent Luminescence Nanoparticles for In Vivo Imaging” *J. Am. Chem. Soc.* **2011**, *133*, 11810–11815.

160. Garcia, J.; Kuda-Wedagedara, A. N. W.; Allen, M. J. “Physical Properties of Eu²⁺-Containing Cryptates as Contrast Agents for Ultrahigh-Field Magnetic Resonance Imaging” *Eur. J. Inorg. Chem.* **2012**, 2135–2140.
161. Corbin, B. A.; Basal, L. A.; White, S. A.; Shen, Y.; Haacke, E. M.; Fishbein, K. W.; Allen, M. J. “Screening of ligands for redox-active europium using magnetic resonance imaging” *Bioorg. Med. Chem.* **2018**, *26*, 5274–5279.
162. Basal, L. A.; Yan, Y.; Shen, Y.; Haacke, E. M.; Mehrmohammadi, M.; Allen, M. J. “Oxidation-Responsive, Eu^{II/III}-Based, Multimodal Contrast Agent for Magnetic Resonance and Photoacoustic Imaging” *ACS Omega* **2017**, *2*, 800–805.
163. Reda, T.; Barker, C. D.; Hirst, J. “Reduction of the Iron–Sulfur Clusters in Mitochondrial NADH:Ubiquinone Oxidoreductase (Complex I) by Eu^{II}-DTPA, a Very Low Potential Reductant” *Biochemistry*, **2008**, *47*, 8885–8893.
164. Yao, S.; Chan, H.-S.; Lam, C.-K.; Lee, H. K. “Synthesis, Structure, and Reaction Chemistry of Samarium(II), Europium(II), and Ytterbium(II) Complexes of the Unsymmetrical Benzamidinate Ligand [PhC(NSiMe₃)(NC₆H₃Prⁱ_{2-2,6})]” *Inorg. Chem.* **2009**, *48*, 9936–9946.
165. Moore, J. A.; Cowley, A. H.; Gordon, J. C. “Mediating Oxidation States in Decamethyleuropocene Complexes. The Role of the Diazabutadiene Fragment” *Organometallics* **2006**, *25*, 5207–5209.
166. Lin, L.; Ning, L.; Zhou, R.; Jiang, C.; Peng, M.; Huang, Y.; Chen, J.; Huang, Y.; Tao, Y.; Liang, H. “Site Occupation of Eu²⁺ in Ba_{2-x}Sr_xSiO₄ (x = 0–1.9) and Origin of Improved Luminescence Thermal Stability in the Intermediate Composition” *Inorg. Chem.* **2018**, *57*, 7090–7096.

167. Strobel, P.; Niklaus, R.; Schmidt, P. J.; Schnick, W. "Oxoberyllates SrBeO_2 and $\text{Sr}_{12}\text{Be}_{17}\text{O}_{29}$ as Novel Host Materials for Eu^{2+} Luminescence" *Chem. Eur. J.* **2018**, *24*, 12678–12685.
168. Ishida, A.; Toki, S.; Takamuku, S. "Hydroxymethylation of 1,3-Dimethyluracil and Its Derivatives induced by a Photoredox System of $\text{Eu}^{\text{III}}/\text{Eu}^{\text{II}}$ in MeOH" *J. Chem. Soc., Chem. Commun.* **1985**, 1481–1483.
169. Douglas, D. L.; Yost, D. M. "Photo-Chemical Reduction of Water by Europium (II) Ion, and the Magnetic Susceptibilities of Europium (II) and (III) Ions" *J. Chem. Phys.* **1949**, *17*, 1345–1346.
170. Davis, D. D.; Stevenson, K. L.; King, G. K. "Photolysis of Europium(II) Perchlorate in Aqueous Acidic Solution" *Inorg. Chem.* **1977**, *16*, 670–673.
171. Ekanger, L. A.; Ali, M. M.; Allen, M. J. "Oxidation-responsive $\text{Eu}^{2+/3+}$ -liposomal contrast agent for dual-mode magnetic resonance imaging" *Chem. Commun.* **2014**, *50*, 14835–14838.
172. Burai, L.; Scopelliti, R.; Tóth, É. " Eu^{II} -cryptate with optimal water exchange and electronic relaxation: a synthon for potential pO_2 responsive macromolecular MRI contrast agents" *Chem. Commun.* **2002**, 2366–2367.
173. Garcia, J.; Neelavalli, J.; Haacke, E. M.; Allen, M. J. " Eu^{II} -containing cryptates as contrast agents for ultra-high field strength magnetic resonance imaging" *Chem. Commun.* **2011**, *47*, 12858–12860.

174. Garcia, J.; Allen, M. J. "Interaction of biphenyl-functionalized Eu^{2+} -containing cryptate with albumin: Implications to contrast agents in magnetic resonance imaging" *Inorg. Chim. Acta* **2012**, *393*, 324–327.
175. Ekanger, L. A.; Allen, M. J. "Overcoming the Concentration-Dependence of Responsive Probes for Magnetic Resonance Imaging" *Metallomics*, **2015**, *7*, 405–421.
176. Ekanger, L. A.; Polin, L. A.; Shen, Y.; Haacke, E. M.; Allen, M. J. "Evaluation of Eu^{II} -Based Positive Contrast Enhancement after Intravenous, Intraperitoneal, and Subcutaneous Injections" *Contrast Media Mol. Imaging* **2016**, *11*, 299–303.
177. Shannon, R. D. "Revised Effective Ionic Radii and Systematic Studies of Interatomic Distances in Halides and Chalcogenides" *Acta Cryst.* **1976**, *A 32*, 751–767.
178. Huh, D. N.; Ziller, J. W.; Evans, W. J. "Facile Encapsulation of Ln(II) Ions into Cryptate Complexes from $\text{LnI}_2(\text{THF})_2$ Precursors (Ln = Sm, Eu, Yb)" *Inorg. Chem.* **2019**, *58*, 9613–9617.
179. Gamage, N.-D. H.; Mei, Y.; Garcia, J.; Allen, M. J. "Oxidatively Stable, Aqueous Europium(II) Complexes through Steric and Electronic Manipulation of Cryptand Coordination Chemistry" *Angew. Chem. Int. Ed.* **2010**, *49*, 8923–8925.
180. Burdett, J. K.; Hoffmann, R.; Fay, R. C. "Eight-Coordination" *Inorg. Chem.* **1978**, *17*, 2553–2568.
181. Cox, B. G.; Truong, N. V.; Garcia-Rosas, J.; Schneider, H. "Kinetics and Equilibria of Alkaline-Earth-Metal Complex Formation with Cryptands in Methanol" *J. Phys. Chem.* **1984**, *88*, 996–1001.

182. McClure, D. S.; Kiss, Z. "Survey of the Spectra of the Divalent Rare-Earth Ions in Cubic Crystals" *J. Chem. Phys.* **1963**, *39*, 3251–3257.
183. Fieser, M. E.; MacDonald, M. R.; Krull, B. T.; Bates, J. E.; Ziller, J. W.; Furche, F.; Evans, W. J. "Structural, Spectroscopic, and Theoretical Comparison of Traditional vs Recently Discovered Ln²⁺ Ions in the [K(2.2.2-cryptand)][(C₅H₄SiMe₃)₃Ln] Complexes: The Variable Nature of Dy²⁺ and Nd²⁺" *J. Am. Chem. Soc.* **2015**, *137*, 369–382.
184. Yee, E. L.; Gansow, O. A.; Weaver, M. J. "Electrochemical Studies of Europium and Ytterbium Cryptate Formation in Aqueous Solution. Effects of Varying the Metal Oxidation State upon Cryptate Thermodynamics and Kinetics" *J. Am. Chem. Soc.* **1980**, *102*, 2278–2285.
185. Gál, M.; Kielar, F.; Sokolová, R.; Ramešová, S.; Kolivoška, V. "Electrochemical Study of the Eu^{III}/Eu^{II} Redox Properties of Complexes with Potential MRI Ligands" *Eur. J. Inorg. Chem.* **2013**, 3217–3223.
186. Pohl, R.; Montes, V. A.; Shinar, J.; Anzenbacher, P., Jr. "Red–Green–Blue Emission from Tris(5aryl-8quinolinolate)Al(III) Complexes" *J. Org. Chem.* **2004**, *69*, 1723–1725.
187. Bratsch, S. G. "Standard Electrode Potentials and Temperature Coefficients in Water at 298.15 K" *J. Phys. Chem. Ref. Data* **1989**, *18*, 1–21.
188. Connelly, N. G.; Geiger, W. E. "Chemical Redox Agents for Organometallic Chemistry" *Chem. Rev.* **1996**, *96*, 877–910.

189. Marsh, M. L.; White, F. D.; Meeker, D. S.; McKinley, C. D.; Dan, D.; Van Alstine, C.; Poe, T. N.; Gray, D. L.; Hobart, D. E.; Albrecht-Schmitt, T. E. "Electrochemical Studies of Selected Lanthanide and Californium Cryptates" *Inorg. Chem.* **2019**, *58*, 9602–9612.
190. Dietrich, B.; Dilworth, B.; Lehn, J.-M.; Souchez, J.-P. "Anion Cryptates: Synthesis, Crystal Structures, and Complexation Constants of Fluoride and Chloride Inclusion Complexes of Polyammonium Macrobicyclic Ligands" *Helv. Chim. Acta* **1996**, *79*, 569–587.
191. Garcia, J.; Allen, M. J. "Developments in the Coordination Chemistry of Europium(II)" *Eur. J. Inorg. Chem.* **2012**, 4550–4563.

ABSTRACT**THE EFFECTS OF COORDINATION ENVIRONMENT ON THE SPECTROSCOPIC AND ELECTROCHEMICAL PROPERTIES OF DIVALENT LANTHANIDES**

by

TYLER CHRISTIAN JENKS**August 2020****Advisor:** Dr. Matthew J. Allen**Major:** Chemistry (Inorganic)**Degree:** Doctor of Philosophy

The research projects in this dissertation pertain to the properties of molecular divalent lanthanide complexes with a focus on luminescence properties in solution. Most available research in lanthanide chemistry focuses on either the trivalent oxidation state or the divalent oxidation state in solid inorganic host matrices. The results described herein contribute to the body of knowledge regarding the effects of coordination environment on the spectroscopic and electrochemical properties of divalent lanthanides in solvated molecular complexes.

The divalent-europium-containing complex $\text{Eu}^{\text{II}}\mathbf{23}$ was evaluated as a visible-light-excited photoredox precatalyst. Stoichiometric and catalytic carbon–carbon bond forming reactions of $\text{Eu}^{\text{II}}\mathbf{23}$ with benzyl chloride in the presence of blue light were performed. A substrate scope with organic substrates of varying reduction potentials was also explored to frame the electrochemical window within which the precatalyst can perform chemical reductions. Spectroscopic, electrochemical, and structural characterizations of the complex add insight to the mechanistic aspects of the reductive coupling reaction. The results of this study serve as

foundational knowledge for future research endeavors focusing on Eu^{II} -based photoredox chemistry.

The divalent-europium-containing complex $\text{Eu}^{\text{II}}\mathbf{25}$, a structurally modified variant of $\text{Eu}^{\text{II}}\mathbf{23}$, was synthesized to examine the electronic and steric effects of alkylated tertiary amines versus secondary amines on the luminescence of the coordinated Eu^{II} ion. The steric bulk of the added methyl groups forced $\text{Eu}^{\text{II}}\mathbf{25}$ into a lower coordination number than $\text{Eu}^{\text{II}}\mathbf{23}$, invoking hypsochromic spectroscopic shifts that were not expected based strictly on the electronic character of the tertiary amine donors of $\mathbf{25}$. The steric hindrance of the methyl groups in $\mathbf{25}$ provided increased protection of the Eu^{II} ion from nonradiative interactions with solvent molecules with respect to $\mathbf{23}$, providing a substantial increase in the luminescence quantum yield of the complex. The results of this study provide information for tuning the luminescence wavelength and intensity of Eu^{II} -containing complexes in solution.

A series of Yb^{II} -containing cryptates with varying electronic and steric character was synthesized and characterized. Structural, spectroscopic, and electrochemical trends among the complexes were observed. These trends were compared to the trends observed in the analogous series of Eu^{II} -containing complexes, with differences and similarities between the trends being discussed. The results of this study serve as an imperative guide as to the translatability of ligand trends across the divalent lanthanide series

The results of these studies are expected to enhance the ability to selectively and rationally modulate the luminescence of divalent-lanthanide-containing complexes based on metal selection and coordination environment, ultimately improving the intrigue and impact of the field of divalent lanthanide luminescence in solution.

AUTOBIOGRAPHICAL STATEMENT

Publications

1. **Jenks, T. C.**; Bailey, M. D.; Hovey, J. L.; Fernando, S.; Basnayake, G.; Cross, M. E.; Li, W.; Allen, M. J. "First Use of a Divalent Lanthanide in Visible-Light-Promoted Photoredox Catalysis" *Chem. Sci.* **2018**, *9*, 1273–1278.
2. **Jenks, T. C.**; Bailey, M. D.; Corbin, B. A.; Kuda-Wedagedara, A. N. W.; Martin, P. D.; Schlegel, H. B.; Rabuffetti, F. A.; Allen, M. J. "Photophysical Characterization of a Highly Luminescent Divalent-Europium-Containing Azacryptate" *Chem Commun.* **2018**, *54*, 4545–4548.
3. **Jenks, T. C.**; Kuda-Wedagedara, A. N. W.; Bailey, M. D.; Ward, C. L.; Allen, M. J. "Spectroscopic and Electrochemical Trends in Divalent Lanthanides through Modulation of Coordination Environment" *Inorg. Chem.* **2020**, *59*, 2613–2620.
4. **Jenks, T. C.**; Allen, M. J. Low-Valent Lanthanide Luminescence in Solution. In *Lanthanide Luminescence: Photophysical, Analytical and Biological Aspects*. In Springer Series on Fluorescence; de Bettencourt-Dias, A., Ed.; Springer Verlag: Berlin, Heidelberg, 2020; Vol. x, pp xx–xx. *submitted (invited)*.

Fellowships and Awards

American Chemical Society-Division of Inorganic Chemistry Travel Award	2018
Joseph Jasper Scholarship for Graduate Students in Chemistry	2018
Thomas C. Rumble Graduate Research Fellowship	2018–2019
A. Paul and Carol C. Schaap Endowed Distinguished Graduate Award	2018–2019
Heller Fellowship	2019–2020

Presentations/Conferences

National

1. 256th ACS National Meeting and Exposition. Boston, MA. August 19–23, 2018; Poster.

Regional

1. *Ohio Inorganic Weekend 2016*. University of Akron, Akron, OH. November 4–5, 2016; Poster.
2. 48th Central Regional Meeting of the American Chemical Society. Dearborn, MI. June 6–9, 2017; Poster Abstract CERM-141.
3. *Ohio Inorganic Weekend 2017*. Ohio State University, Columbus, OH. November 3–4, 2017; Poster.
4. *Ohio Inorganic Weekend 2018*. Ohio University, Athens, OH. November 9–10, 2018; Oral presentation.
5. *Ohio Inorganic Weekend 2019*. University of Toledo, Toledo, OH. November 1–2, 2019; Poster.

Local

1. 18th Annual Chemistry Graduate Research Symposium 2016. Wayne State University, Detroit, MI. October 22, 2016; Poster.
2. 19th Annual Chemistry Graduate Research Symposium 2017. Wayne State University, Detroit, MI. October 14, 2017; Poster.
- 20th Annual Chemistry Graduate Research Symposium 2018. Wayne State University, Detroit, MI. October 6, 2018; Poster.